Mitfa-Independent Melanocyte Progenitors are Highly Susceptible to GNAQ-induced Uveal Melanoma in Adult Zebrafish

Julius I. Yevdash,[1] Delaney Robinson,[1] Rachel Moore,[1] Zhijie Li,[1] Katelyn R. Campbell-Hanson,[1] Danielle Gutelius,[2] Stephen P. G. Moore,[2] Dylan Friend,[1] Isaac O'Toole,[1] Collin Montgomery,[1] Jesse D. Riordan,[3,4] Adam J. Dupuy,[3,4] Robert A. Cornell,[5] Elaine M. Binkley,[4,6,7] Deborah Lang,[2] Ronald J. Weigel,[1,3,4] Colin Kenny[1,3,4,5,8]

1. Department of Surgery, College of Medicine, University of Iowa, Iowa City, IA 52242, USA.
2. Department of Dermatology, Boston University School of Medicine, Boston, MA, 02118, USA.
3. Department of Anatomy & Cell Biology, University of Iowa, Iowa City, IA, 52242, USA.
4. Holden Comprehensive Cancer Center, University of Iowa, Iowa City, IA 52242, USA.
5. Department of Oral Health Sciences, University of Washington, School of Dentistry, Seattle, WA, 98195
6. Department of Ophthalmology and Visual Sciences, University of Iowa, Iowa City, IA 52242, Iowa
7. University of Iowa, Institute for Vision Research, Iowa City, IA 52242, Iowa
8. Lead Contact.

* Corresponding author: colin-kenny@uiowa.edu

Summary

Melanocytes reside in diverse microenvironments that influence their susceptibility to oncogenic transformation, however, studying rare melanoma subsets has been hindered by the lack of suitable animal models. We developed a primary, immune-competent zebrafish model to study uveal melanoma (UM), utilizing choroidal-targeted injection and electroporation of plasmids containing human *GNAQ*^{Q209L} and CRISPR/Cas9 cassettes for tumor suppressor gene deletion. Single-cell transcriptional profiling of genetically identical eye- and skin-derived tumors revealed distinct oncogenic pathways, highlighting the importance of studying melanoma subtypes in their correct anatomical context. Additionally, we identified a population of *tfec*- and *pax3a*-expressing melanocyte progenitor cells in *mitfa*-deficient embryos and adult zebrafish eyes, which were highly susceptible to GNAQ-driven transformation. While previous studies have linked *mitfa* deficiency to accelerated UM onset, our findings suggest that an expanded progenitor population in *mitfa*-deficient animals drives this susceptibility. Our study establishes a critical role for Mitfa-independent melanocyte progenitors in UM pathogenesis

Highlights

- Choroid-targeted electroporation of oncogenic GNAQ induces anatomically correct UM in adult zebrafish.
- Mitfa-independent melanocyte progenitor cells are highly susceptible to GNAQ-driven transformation.
- Germline loss of *mitfa* accelerates UM onset via progenitor enrichment, a phenotype not recapitulated by conditional *mitfa*-KO in adult zebrafish.
- Oncogenic BRAF and GNAQ transform molecularly and developmentally distinct subpopulations of cells within the melanocyte lineage.

52 **Introduction**

53

54 Uveal melanoma (UM) is a rare cancer of the melanocytes in the eye that is both vision
55 threatening and deadly.[1-4] The majority of UM's (~90%) occur in the choroid, the vascular
56 structure supplying the outer retina, with the remainder arising from the ciliary body or the iris.[5-9]
57 Oncogenic mutations in *GNAQ* or its paralog *GNA11* are observed in up to 90% of UMs, but are
58 rare in cutaneous melanoma (CM).[4,10] Such mutations reduce GTPase activity of the
59 heterotrimeric G protein alpha subunit, resulting in constitutive activation that drives cellular
60 proliferation through downstream signaling pathways, including MAPK, YAP/TAZ, and PI3K
61 signaling.[5,11-13]

62

63 UM and CM display distinct metastatic progression. Up to 50% of UM tumors metastasize to the
64 liver via hematogenous spread,[3,14,15] and survival after metastasis is generally poor [16] There
65 remain few FDA approved options for patients with metastatic UM. Tebentafusp was the first
66 systemic therapy shown to improve overall survival in metastatic UM at both 1 year and 3 years;
67 however, this is only approved in HLA-A02:01-positive patients and, despite being an
68 improvement, progression free survival at 6 months was only 31%, and median overall survival
69 at 3 years was only 21.6 months in treated patients [17,18] Chemotherapy and immune checkpoint
70 inhibitors, which are highly effective in CM, have very limited efficacy in UM.[19,20] Some
71 promising targeted therapies are currently under investigation, including Darovasertib, a PKC
72 inhibitor targeting GNAQ/GNA11-driven MAPK signaling,[21] and more invasive options, such as
73 melphalan-based liver treatment, have demonstrated some benefit in the absence of other
74 effective systemic options.[22]

75

76 While *GNAQ/11* oncogenic mutations are uncommon in CM, the majority of CMs harbor
77 activating mutations in *BRAF* or *NRAS*.[5,23-25] This distinction suggests that unique properties of

78 melanocytes in different tissues, or perhaps their tumor microenvironments (TME), may drive
79 differential oncogene sensitivity. Melanocytes in the choroid interact with fibroblasts and
80 vasculature endothelial cells, whereas melanocytes in the skin are in direct contact with
81 keratinocytes. In transgenic experiments, $BRAF^{V600E}$-positive melanocytes exhibit significantly
82 greater survival in the epidermis compared to $GNAQ^{Q209L}$-positive melanocytes. However,
83 $GNAQ^{Q209L}$-positive melanocytes preferentially survived in the dermis, where fibroblasts are
84 abundant.[26] This suggests that oncogene-specific interactions with the microenvironment
85 influence melanocyte survival and provide a basis for the absence of *GNAQ* mutations in CM,
86 except for dermal blue nevi which interact closely with fibroblasts.[10,26] Interestingly, while UM
87 and CM are unique in their metastatic patterns, GNAQ/11-mutant non-uveal melanoma
88 demonstrates a lymphatic metastatic progression that resembles CM, thus further indicating the
89 importance of studying UM in the correct anatomical context.[24]
90
91 Zebrafish are a well-established model for studying melanocytes and melanoma due to
92 conserved melanocyte differentiation pathways, efficient genetic manipulation, and the use of
93 transparent lines that facilitate high-resolution live-cell imaging.[24,27-35] Zebrafish have three types
94 of pigment cells; dark melanocytes, iridescent iridophores, and yellow xanthophores, that arise
95 from multipotent, neural crest-derived pigment progenitors.[24,33,36-39] Melanomas have been
96 shown to upregulate neural crest transcriptional programs, which are associated with worse
97 clinical outcomes.[29,40-42] Similarly, *Tg(mitfa:GNAQ^{Q209L}); mitfa$^{-/-}$* zebrafish, which retain
98 melanocyte progenitor cells but lack differentiated melanocytes,[43] have earlier occurrences of
99 UM than wild-type zebrafish.[34] By contrast, BRAF-driven CM displays a reliance on Mitfa activity
100 to progress.[44,45] To study the early events of UM, we developed a novel zebrafish model that
101 utilizes the transgene electroporation of adult zebrafish (TEAZ) approach to express the human
102 $GNAQ^{Q209L}$ oncogene in cells of the melanocyte lineage within the skin and eye. By targeting
103 injections to the choroid, primary UM tumors arise from the same anatomical location as human

104 UM, recapitulating similar TME and initiating cell types. In this study, we analyze expression
105 differences between genetically identical skin and eye-derived GNAQ^{Q209L} tumors and
106 demonstrate the existence of a melanocyte precursor population in the eyes zebrafish that have
107 an increased sensitivity to transformation by GNAQ^{Q209L}.
108
109 **Results**
110
111 **Generation of plasmid constructs to drive GNAQ^{Q209L}-induced melanoma.**
112
113 To study GNAQ-driven melanoma in adult zebrafish, we generated expression plasmids
114 containing two cassettes under the control of the *mitfa* promoter. The first cassette encoded
115 human oncogenic *GNAQ^{Q209L}* fused to a T2A self-cleaving peptide followed by eGFP, while the
116 second cassette expressed CRISPR/Cas9. Additionally, three zebrafish U6 promoters were
117 used to drive gRNAs targeting *tp53* and *ptena/b* (**Figure 1A** – strategy A). Recognizing that T2A
118 cleavage results in residual amino acids remaining on the C-terminus of GNAQ, which may alter
119 its oncogenic activity, we employed an alternative delivery strategy. This system utilized five
120 separate plasmids: (1) *mitfa:GNAQ^{Q209L}; mitfa:eGFP* (a generous gift from Dr. Jacqueline Lees
121 at the KOCH institute Massachusetts Institute of Technology), (2) *mitfa:Cas9*, (3) *U6:*gRNA-
122 *tp53*, (4) *U6:*gRNA-*ptena* and (5) *U6:*gRNA-*ptenb* (**Figure 1A** – strategy B) (plasmids 2-5 were a
123 generous gift from Dr. Richard White at the University of Oxford, UK). This design aimed to
124 improve the oncogenicity of GNAQ^{Q209L} by avoiding unintended C-terminal modifications by T2A
125 cleavage. Moreover, the plasmids used in strategy B are smaller in size, which may enhance
126 the efficiency of uptake during electroporation.
127 We applied TEAZ to the skin (TEAZ-Skin) of adult wild-type (*AB*), *mitfa$^{w2/w2}$* (*nacre*
128 [43]), and *mitfa$^{w2/w2}$; mpv17$^{a9/a9}$* (*casper*[46,47]) zebrafish to validate the oncogenic potential of
129 *GNAQ^{Q209L}* (**Figure 1B**). TEAZ-Skin using Strategy A and Strategy B induced melanoma in wild-

130 type zebrafish within an average of 147- and 104-days, respectively (**Figure 1C-D, Figure**
131 **S1A**). TEAZ-Skin using plasmids to express oncogenic *GNAQ* alone or Cas9 with gRNAs to
132 delete *tp53, ptena* or *ptenb* alone did not induce melanoma, suggesting that both oncogenic
133 *GNAQ* and tumor suppressor deletion are required for transformation (**Figure S1A,** black line,
134 n=15). TEAZ-Skin was subsequently applied to zebrafish lacking functional *mitfa* (*nacre* and
135 *casper*), which lack differentiated melanocytes. Consistent with previous observations in
136 transgenic *Tg(mitfa-GNAQ^{Q209L}); mitfa$^{w2/w2}$; tp53$^{-/-}$* zebrafish,[34] *mitfa* loss resulted in decreased
137 tumor latency compared to wild-type zebrafish (**Figure 1C-D, Figure S1B,B'-C**). Tumors were
138 detected within an average of 30- and 28-days post-electroporation following Strategy B in
139 *nacre* and *casper*, respectively. Moreover, unlike wild-type zebrafish and consistent with
140 previous reports,[40] expression of oncogenic GNAQ alone was sufficient to induce melanoma in
141 *nacre* (**Figure 1D, Figure S1B**) and *casper* zebrafish (**Figure 1D, Figure S1C-D**). We ruled out
142 xanthomas as the cell of origin for TEAZ-Skin tumors, given the distinct visual differences
143 between the tumors and the xanthomas observed in *Tg*(*mitfa*$^{w2/w2}$, *mitfa*:*BRAF^{V600E}*, *tp53$^{-/-}$*)
144 zebrafish. The xanthomas were bright orange, opaque, and clearly distinguishable from the
145 darkly pigmented UM tumors in wild-type zebrafish and the beige, translucent UM tumors in
146 *casper* zebrafish (**Figure S1E**). CRISPR editing in TEAZ-Skin tumors was confirmed by Sanger
147 sequencing. All but one tumor (10 of 11) exhibited edits in all three targeted tumor suppressors
148 (*tp53*, *ptena*, and *ptenb*), with the remaining tumor lacking *ptena* mutation. As expected,
149 uninjected tissue showed no evidence of CRISPR editing (**Figure S2**).
150 Together, our findings demonstrate that both TEAZ-Skin strategies are sufficient to induce
151 GNAQ-driven melanoma, with strategy B demonstrating reduced tumor latency compared to
152 strategy A. Notably, TEAZ-Skin accelerates melanoma onset relative to transgenic models;[34]
153 while tumors in transgenic *Tg(mitfa:GNAQ^{Q209L}); tp53$^{-/-}$* zebrafish typically arise 200-400 days
154 post-fertilization,[34] TEAZ-Skin induces UM tumors by approximately 100 days in wild-type
155 zebrafish.

156 **The *mitfa* promoter is active in choroidal melanocytes**

157

158 Having confirmed the oncogenicity of our *GNAQ*^{Q209L} expression plasmids using TEAZ-Skin, we
159 next sought to adapt this approach to induce melanocyte transformation in the zebrafish eye
160 (TEAZ-Eye), specifically targeting the choroid, where the majority of ocular melanocytes reside
161 (**Figure 1E**). To determine whether TEAZ-Eye could serve as a model for UM in adult zebrafish,
162 we first assessed the specificity of the *mitfa* promoter in driving transgene expression in
163 choroidal melanocytes. To this end, we harvested eyes from transgenic *Tg(mitfa:GFP)* zebrafish
164 and performed immunofluorescent imaging using an anti-GFP antibody. Choroidal melanocytes
165 exhibited strong anti-GFP positivity compared to the secondary-only control (**Figure 1F**). Of
166 note, the retinal pigment epithelium (RPE), located apically to the choroidal melanocytes,
167 contains autofluorescent granules. Quenching the autofluorescence signal from the RPE
168 improved the anti-GFP signal-to-noise ratio (**Figure S3A-B**). We next applied TEAZ-Eye by
169 injecting and electroporating plasmids containing the *mitfa* promoter driving *eGFP* expression
170 (*mitfa:eGFP*) into the choroid. Eyes were harvested two weeks post-electroporation, and
171 immunofluorescence using an anti-GFP antibody was performed. Remarkably, cells at the
172 injection site exhibited a strong eGFP signal compared to the secondary-only control (**Figure**
173 **S3C**). These results demonstrate that the *mitfa* promoter is sufficient to drive transgene
174 expression in choroidal melanocytes using TEAZ-Eye.

175

176 **TEAZ-Eye induces UM in the choroid of wild-type and *casper* zebrafish**

177

178 A major limitation in the study of UM onset and progression is the lack of anatomically accurate
179 *in vivo* models. For instance, UM tumors derived in transgenic *Tg(GNAQ*^{Q209L}*): tp53*$^{-/-}$ zebrafish
180 predominantly form in the skin, with ~1-2% of tumors forming in the eye.[34] To address this gap,
181 we applied TEAZ-Eye using a plasmid pool containing *mitfa:GNAQ*^{Q209L}*, mitfa:Cas9, U6:*gRNA-

182 *tp53, U6:*gRNA-*ptena, and U6:*gRNA-*ptenb* (i.e., Strategy B) into the choroidal space of wild-
183 type zebrafish, followed by electroporation (**Figure 1G-H**). Remarkably, TEAZ-Eye in wild-type
184 zebrafish resulted in the transformation of cells within the choroid. Live *in vivo* imaging of TEAZ-
185 Eye enabled the identification of single GFP+ cells at the injection site, serving as a proxy for
186 *GNAQ*^{Q209L} expression (**Figure 1H-H'**). We next applied TEAZ-Eye to *mitfa*-deficient *casper*
187 zebrafish (**Figure 1I-I'**), and like with TEAZ-Skin, tumor latency of TEAZ-Eye injected *casper*
188 zebrafish (n=10) was significantly reduced compared to wild-type (n=5) (**Figure 1J**). H&E
189 analysis confirmed that TEAZ-Eye induced UM within the choroid, progressing into surrounding
190 ocular structures (**Figure 1K**). Notably, 100% (n=10) of tumors formed between the sclera and
191 RPE, highlighting the model's ability to induce anatomically accurate UM. Finally,
192 immunofluorescent analysis using anti-GFP antibodies confirmed the expression of plasmid
193 constructs following TEAZ-Eye (**Figure 1K'**).
194
195 **UM transformation involves activation of neural crest transcriptional programs**
196
197 During embryonic development, choroidal melanocytes are derived from the cranial neural crest
198 (CNC)[48]. Since our model can detect the earliest events in UM transformation, we asked
199 whether the reactivation of CNC programs is one of the initial steps in UM development. To
200 achieve this goal, tumors were derived in wild-type zebrafish using TEAZ-Eye with Strategy B
201 plasmids. At 50-90 dpe, when gross nodular tumors were identified, surgical enucleation was
202 performed, and dissociated cells from the entire eye were subjected to single-cell RNA
203 sequencing (scRNA-seq). We compared pooled wild-type tumors (2 sequencing replicates) with
204 tumor paired bilateral eyes or sibling-matched control eyes (2 and 4 pooled eyes, respectively, 2
205 sequencing replicates). Given that whole eyes were used as control samples and melanocytes
206 are most abundant in the choroid, melanocytes identified under control conditions are hereafter
207 referred to as choroidal melanocytes. Tumor cells were identified by expression of *GFP* and

208 oncogenic *GNAQ* (**Figure 2B**) whereas primary choroidal melanocytes were marked by
209 expression of *mlana* (**Figure S4**). Annotation of additional cell types within the TME was
210 accomplished by comparing to previously published scRNA-seq datasets using human choroid
211 and retina,[49,50] the Zebrafish Information Network (ZFIN),[51] and from the zebrafish embryo single
212 cell atlas "Daniocell"[52] (**Figure 2A**). Interestingly, tumor cells aligned most closely with choroidal
213 melanocytes, ruling out the retinal pigmented epithelium (RPE) as an origin of our TEAZ-Eye
214 induced tumors (**Figure 2C**). Additionally, profiling *GFP/GNAQ*^{Q209L}+ UM cells revealed that
215 tumors exhibited strong expression of neural crest markers (*tfap2a, tfap2c, pax7b, sox10, foxd3*)
216 and melanocytic markers (*mitfa, tfap2e, mlana, pmela, slc22a7a, mlpha, mtbl*) (**Figure 2D**).
217 Unexpectedly, the CNC marker genes *twist1* or *dlx1*[53,54] were not enriched in UM tumors
218 compared to the TME. Pathway analysis showed that the genes enriched in TEAZ-Eye-derived
219 tumors were strongly associated with MITF-M-dependent gene expression, RAF/MAP kinase,
220 mTOR, PI3K/AKT signaling, NF-kB, RHO GTPase, and NOTCH activity, as well as fatty acid
221 oxidation pathways (**Figure S6A-B**).
222
223 Re-clustering of choroidal cells from control and tumor conditions revealed a marked expansion
224 of tumor cells relative to melanocytes which was accompanied by increases in immune cell
225 populations and fibroblasts (**Figure 2E-F**). Immune cell populations within the TME included B-
226 cells (*igic1s1, pax5, cd79a, zgc:153659*), T-cells (*traf1, si:ch211-67e16.3, cd27, zap70, cd8a,*
227 *sla2*), a population of cytokine producing cells, likely representing T-cells (*il4, il13, il11, ca2, il34,*
228 *il6*) as well as macrophages (*marco, ccl34a.4, mrc1b, c1qa/b/c, grn1*) and neutrophils (*cpa5,*
229 *lect2l, mmp9, npsn, scpp8*). Additional cell types within the choroidal TME included fibroblasts
230 (*col1a1a, col1a1b, col1a2, col5a1, dcn, serpinf1*), pericytes (*pdgfrb, notch3, foxf2b, cd248a*),
231 Schwann cells (*dlx5a, apoda.1, mpz, plp1b, cd59, s100b, mbap*) and vasculature endothelial
232 cells (*vwf, flt4, epas1b, ecscr, fabp11a*) (**Figure 2D-F**, **Table S1**).
233

234 We next compared choroidal melanocytes and UM tumors, revealing a significant overlap in
235 gene expression (n=644; hypergeometric $p < 0.0001$) alongside a large set of tumor-enriched
236 genes (n=1177) (**Figure 2G**). Shared genes included melanocytic regulators (*ednrb, sox10,*
237 *foxd3, mitfa, mlpha, kita, mlana, pax7b*), supporting a melanocytic origin, and many of these
238 transcripts were further upregulated in UM tumors compared to choroidal melanocytes (**Figure**
239 **2H**). HOMER promoter motif enrichment analysis of genes enriched in UM tumors revealed
240 binding motifs for the MiT/TFE family of transcription factors, as well as PAX7 and HOXB13,
241 suggesting that these regulators may contribute to UM-specific transcriptional programs (**Figure**
242 **2G'**) Differential expression analysis further identified several genes enriched in UM tumors and
243 associated with patient survival, including *lgals2a, fabp3, gch2*, and the proto-oncogene *kita*
244 (**Figure 3H**). High expression of *FABP3, FABP5, KIT, GCH,* and *LGALS2* correlated with worse
245 overall survival (OS) and disease-free survival (DFS) in UM (**Figure 3I-K, Figure S7**), and these
246 genes were preferentially associated with TCGA molecular subtypes 3 and 4, representing the
247 more aggressive forms of UM (**Figure S8, Table S2**).[55]
248
249 **Cancer associated fibroblasts within the uveal TME upregulate components of the**
250 **extracellular matrix (ECM)**
251
252 Recent studies have significantly advanced our understanding of the TME as an active driver of
253 melanoma progression.[56,57] While it is well established that components of the TME, particularly
254 cancer-associated fibroblasts (CAFs), play a key role in malignancy,[58-60] *in vivo* models to study
255 such interactions in UM remain limited. Our model allows for direct comparison of the TME in
256 TEAZ-Eye and control injected eyes within the same animals. We compared the transcriptome
257 of CAFs and normal fibroblasts in wild-type zebrafish. Upon reclustering and differential gene
258 expression analysis of normal eye fibroblasts and CAFs, we found that several ECM proteins
259 were upregulated, indicating remodeling of the ECM in the presence of UM. Enriched genes

260 broadly fell into four categories: ECM, ECM regulators, TNFs, and collagens. Notably,
261 fibronectin (*fn1a*) was among the most significantly upregulated gene in CAFs compared to
262 normal fibroblasts (q-value < 0.0001). Several collagens were also found to have higher
263 expression in CAFs, including Collagen I (*col1a1b, col1a2),* Collagen V (*col5a1, col5a2a,*
264 *col5a3a)* and Collagen XII (*col12a1a)* (**Figure 2L, Table S3**).
265 To control for injection-related fibrosis potentially causing fibroblast activation and upregulation
266 of ECM components, we mock-injected three wild-type eyes with plasmids containing *mitfa*:GFP
267 and *mitfa*:Cas9 cassettes followed by electroporation (mock-TEAZ) and performed scRNA-seq.
268 Fibroblasts from mock-injected sibling control eyes (three pooled eyes), non-injected sibling
269 control eyes (four pooled eyes), and tumor-matched control non-injected eyes (three pooled
270 eyes) were equally distributed on the UMAP, with no alteration in *fn1a* or *lgals2a* expression or
271 other changes to extracellular matrix (ECM) genes upon mock-TEAZ injection (**Figure S5,**
272 **Figure S9**). These findings suggest that TEAZ-Eye tumor induction, and not the physical
273 injection, in zebrafish triggers a CAF response that may be critical to melanoma progression.
274
275 **Skin and eye melanocytes, and their resulting tumors, have unique gene expression**
276 **profiles**
277
278 With the ability to induce genetically identical tumors in both the eye and the skin of adult
279 zebrafish, we next asked whether tumors arising in these sites were transcriptionally distinct.
280 Any such differences could be due to the relationship between the unique microenvironments of
281 the skin and eye with their respective tumors or they could arise from inherent differences in the
282 untransformed melanocytic cells that reside in the skin or eye. To this end, we generated tumors
283 using TEAZ-Eye and TEAZ-Skin with strategy B plasmids in wild-type zebrafish and compared
284 them with control eye and skin tissue, respectively, using scRNA-seq (**Figure S5**). UMAP
285 analysis revealed that while the tumors and the majority of microenvironment clusters overlap,

286 the eye tissue expectedly had unique cell types corresponding to retinal bipolar cells, glial cells,
287 photoreceptors, and retinal interneurons (**Figure 3A**). To identify transcriptional differences
288 between TEAZ-Eye and TEAZ-Skin tumors, we compared the gene expression profiles of each
289 tumor type relative to the combined TME from both sites. A similar analysis was performed for
290 eye and skin melanocytes relative to the combined uninjected microenvironment (**Figure 3B,**
291 **Table S4**). Notably, the strongest overlap was observed between genes upregulated in skin
292 tumors versus TME and those upregulated in eye tumors versus TME, with 41% of the 2,192
293 unique differentially expressed genes (DEGs) shared, highlighting the broad transcriptional
294 programs activated by *GNAQ*^{Q209L} expression, *tp53* loss, and *ptena/b* loss (**Figure 3C**). We
295 hypothesized that the DEGs shared by only the two tumors and not the primary melanocytes
296 would represent mechanisms that are essential for UM growth and survival. In line with this
297 prediction, IPA analysis of this gene subset revealed that pathways pertaining to cancer
298 proliferation and metabolism were enriched (**Figure S10A**). Furthermore, we noticed an
299 enrichment of WNT signaling, PTEN regulation, and RAF/MAPK pathways which have been
300 previously implicated as important signaling cascades in UM.[61-69] Interestingly, only 5% of DEGs
301 overlapped across all datasets (eye and skin melanocytes and tumors), and we predicted these
302 genes to be associated with melanocyte identity and survival (**Figure 3C**). IPA analysis
303 confirmed this prediction with the most enriched pathway being MITF-M dependent gene
304 expression. Other enriched terms were signaling events that are downstream of GPCRs, such
305 as GNAQ, and pathways that are essential for survival such as nucleotide biosynthesis and
306 amino acid regulation of mTORC1 (**Figure S10B**). Notably, only 25.8% of DEGs overlapped
307 between eye and skin melanocytes, indicating substantial transcriptional differences in
308 melanocytes originating from distinct anatomical regions (**Figure 3C**). We next asked whether
309 transcriptional differences in primary melanocytes would be reflected in the corresponding
310 tumors, that is, whether eye melanocytes would be more similar to eye tumors than skin
311 melanocytes. Interestingly, the overlap of unique DEGs between eye melanocytes and eye

312 tumors relative to their respective microenvironments (386/1823) was not significantly different
313 than the overlap between skin melanocytes and eye tumors (489/1689) (permutation test, p-
314 value = 1, 10,000 permutations) (**Figure 3C**). In contrast, the overlap of unique DEGs between
315 skin melanocytes and skin tumors (552/2350) was significantly greater than the overlap
316 between eye melanocytes and skin tumors (424/2509) (permutation test, p-value = 0, 10,000
317 permutations).
318
319 While this analysis allowed for consideration of genes that were differentially expressed in the
320 same direction and magnitude versus the microenvironment, it would miss the genes that are
321 differentially regulated between the two tissue types directly. Therefore, we reclustered just the
322 normal melanocytes from both eye and skin for direct comparison and found that skin and eye
323 melanocytes clustered separately on the UMAP (**Figure 3D**). Our analysis returned 186 DEGs
324 enriched in eye melanocytes (log2FC > |0.5|, q-value < 0.01) and 229 DEGs enriched in skin
325 melanocytes (log2FC > |0.5|, q-value < 0.01) with 3387 genes not differentially regulated (q-
326 value > 0.01, expressed in at least 10% of cells), displaying modest transcriptional variance
327 between melanocytes of the skin and the eye (**Figure 3E, Table S5**). GSEA analysis of these
328 DEGs between eye and skin melanocytes revealed that skin melanocytes were enriched for
329 DNA repair pathways (p-value < 0.002, FDR < 0.016) and for genes that are upregulated during
330 UV response (p-value < 0.009, FDR < 0.081) (**Figure 3G**). On the other hand, DEGs in eye
331 melanocytes showed an enrichment for the genes involved in downregulating the UV response
332 pathway (p-value < 0.000, FDR < 0.090) and for the gene ontology oxidative phosphorylation
333 pathway (p-value < 0.000, FDR < 0.006). We also reclustered and directly compared skin and
334 eye tumors, with a similar tissue-specific grouping observed (**Figure 3D**). 230 DEGs were
335 enriched in the eye tumors (log2FC > 0.5, q-value < 0.01) and 375 DEGs were enriched in the
336 skin tumors (log2FC > 0.5, q-value < 0.01), while 5,754 genes remained not differentially
337 regulated between the two tumor types (q-value > 0.01, expressed in at least 10% of cells)

338 (**Figure 3F**). Interestingly, there was an enrichment of the epithelial to mesenchymal transition
339 dataset (p-value < 0.000, FDR < 0.020) in the eye tumor as well as an enrichment for the
340 metabolism of selenoamino acids (p-value < 0.000, FDR < 0.000) (**Figure 3H**). The skin tumor
341 was instead enriched for PI3K-AKT-MTOR signaling (p-value < 0.009, FDR < 0.086) and
342 pathways for RHO GTPases activating formins (p-value < 0.002, FDR < 0.058). Therefore, after
343 both types of analyses we conclude that both the primary melanocytes and the GNAQ-driven
344 melanomas are significantly different between the eye and the skin emphasizing the importance
345 of studying UM, and melanocytes in general, in their proper anatomical context.
346
347 **Melanocyte progenitor cells are highly susceptible to oncogenic GNAQ transformation in**
348 ***mitfa*-deficient zebrafish.**
349
350 H&E analysis of *nacre* and *casper* zebrafish eyes showed loss of choroidal melanocytes
351 (**Figure 4A**), whereas melanin in the RPE remains less affected, as previously demonstrated.[33]
352 These observations imply that an *mitfa*-independent melanocyte progenitor cell persists in *nacre*
353 and *casper* eyes and that they are susceptible to oncogenic GNAQ transformation. To identify
354 such cells, we crossed *nacre* (*mitfa*$^{w2/w2}$) with transgenic *Tg(mitfa:GFP)* lines to create
355 *Tg(mitfa:GFP); mitfa*$^{w2/w2}$ zebrafish. We then harvested adult eyes at 5 months and performed
356 anti-GFP immunofluorescence analysis, with the assumption that loss of *mitfa* does not alter
357 expression of the *mitfa* promoter. While GFP+ melanocytes were readily detected in the choroid
358 of *Tg(mitfa:GFP)* zebrafish (**Figure 1F, Figure S3**), staining of *Tg(mitfa:GFP); mitfa*$^{w2/w2}$ eyes
359 revealed rare cells with GFP-positivity (**Figure 4B**). Such GFP+ cells were primarily located in
360 the ciliary body, with isolated cells also found in the choroid, suggesting the persistence of a
361 *mitfa*-independent progenitor population in adult *mitfa*-deficient zebrafish (**Figure 4B**). We next
362 asked whether such cells retain the ability to undergo melanocyte differentiation by using TEAZ-
363 Eye to deliver plasmids containing the *mitfa*-promoter driving expression of *mitfa* (i.e., to

364 overexpress *mitfa* mRNA). Interestingly, overexpression of *mitfa* transcript levels resulted in
365 expansion of choroidal melanocytes in wild-type animals and the rescue of choroidal
366 melanocytes in *mitfa*-deficient (*nacre*) zebrafish as shown by H&E analysis (**Figure S11A-B'**).
367 To assess whether GFP-positive cells are sensitive to oncogenic transformation by GNAQ, we
368 expressed *mitfa*:*GNAQ*^{Q209L} in *Tg(mitfa:GFP); mitfa*$^{w2/w2}$ zebrafish using TEAZ-Eye. In all
369 injected fish (n=3), UM tumors were GFP-positive, suggesting they originated from GFP+
370 progenitor cells within the eye of *Tg(mitfa:GFP); mitfa*$^{w2/w2}$ zebrafish (**Figure S11C**).
371
372 **Melanocyte progenitor cells express neural crest marker genes in *mitfa*-deficient**
373 **zebrafish.**
374
375 We performed scRNA-seq and pseudotime analysis on 3 pooled UM tumors from the eyes of
376 *casper* zebrafish and compared them to the pooled tissue from 3 normal *casper* eyes (**Figure**
377 **4C, Figure S12**). Within the *casper* eyes, we identified a population of cells expressing the
378 *nacre* allele that clustered closely with UM tumors under TEAZ-Eye conditions, termed
379 progenitors (**Figure S13A-B and Tables S6-8**). We re-clustered the progenitor and tumor cells
380 (**Figure 4D**), revealing seven distinct clusters consisting of neural crest-like (NC-like),
381 melanoblast-like, proliferating, progenitor, angiogenic, stress-like, as well as an unidentified
382 cluster marked by *tmsb1, krt91* and *vim* (**Figure 4D, Table S9**). Unsupervised pseudotime
383 analysis supports a lineage trajectory from the progenitor cells to heterogeneous UM tumor cells
384 (**Figure S13C**). Notably, the progenitor cell population in normal *casper* eyes expressed neural
385 crest and melanocyte stem cell marker genes, including *tfap2a, foxd3, sox10*, *pax3a, vim,* and
386 *yap1* (**Figure 4E-F**). UM tumor cells retained expression of these genes but activated additional
387 genes associated with pigment progenitor cell function, including *tfec* and *kita* (**Figure 4F**).
388 Notably, *mitfa* expression in tumors and progenitor cells in *casper* zebrafish reflects the
389 expression of the mutant *mitfa*$^{w2/w2}$ allele, which functions as a lineage tracer to mark cells that

390 would normally express *mitfa* under wild-type conditions (**Figure S13B**). Interestingly, despite
391 the lack of Mitfa activity in *casper* zebrafish, GNAQ-positive UM tumors included a melanoblast-
392 like cluster that exhibited expression of pigmentation genes, including *pmela, mlpha*, and *mlana,*
393 likely explaining the occasional emergence of melanin within tumors as they progress in *casper*
394 zebrafish.
395
396 ***mitfa*-deficient zebrafish exhibit expanded *pax3a* and *tfec* positive melanocyte**
397 **progenitors during embryogenesis.**
398
399 Having established that an Mitfa-independent progenitor population gives rise to UM in *mitfa*-
400 deficient zebrafish, we next examined whether this population is expanded relative to wild-type
401 zebrafish. To test this prediction, we performed scRNA-seq on GFP-positive cells sorted from
402 *Tg(mitfa:GFP);mitfa*$^{w2/w2}$ and *mitfa*$^{+/w2}$ sibling-matched transgenic zebrafish embryos at 28 hours
403 post fertilization (hpf), when melanocytes (zebrafish melanophores) begin to differentiate
404 (**Figure 4G, Figure S12**). We assigned cell-type annotations based on our previously annotated
405 GFP-positive cells from *Tg(mitfa:GFP)* embryos.[30] The 10 clusters included six main cell types:
406 neural crest cells (*sox10, foxd3*), a tripotent precursor of melanoblasts (M), iridoblasts (I), and
407 xanthoblasts (X) (*tfap2a*, *cdkn1ca, slc15a2, ino80e, id3, mycn, tfec*), termed MIX cells, a cluster
408 that expressed high levels of melanoblast/xanthoblast markers (*mitfa, erbb3b, impdh1b, gch2,*
409 *id3*), termed MX cells, a melanoblast cluster (*mitfa, dct, pmel, tyr*), as well as two additional
410 clusters corresponding to xanthoblasts and xanthophores (**Table S10**). For this analysis we
411 referred to MIX and MX cells as melanophore progenitors (**Figure 4G**). As expected,
412 melanophore cells were reduced in *Tg(mitfa:GFP): mitfa*$^{w2/w2}$ zebrafish (**Figure 4G-G'**).
413 However, melanophore progenitors were expanded in *Tg(mitfa:GFP); mitfa*$^{w2/w2}$, while neural
414 crest cells remained unaffected (**Figure 4G-G'**). Melanophore markers were downregulated in
415 GFP-positive cells sorted from *Tg(mitfa:GFP); mitfa*$^{w2/w2}$*,* whereas melanocyte progenitor

416 markers (*pax3a, sox10, foxd3*), as we identified in adult zebrafish eyes, were upregulated in
417 embryonic progenitors from *Tg(mitfa:GFP); mitfa*$^{w2/w2}$ embryos (**Figure 4H, Table S11**). A role
418 for *pax3a* in adult fish eye tissue had not been previously characterized; however, recent studies
419 have identified PAX3 expression in ocular surface melanocytes,[70] and another study reports an
420 association between PAX3 and stem cell markers in UM progression.[71] Consistent with these
421 observations, we identified a *pax3* expressing cell population in adult C57BL/6 mouse eyes in
422 the limbal region, and rarely in the choroid (**Figure S14**). These findings support a rare *pax3*-
423 expressing population in both zebrafish and mouse eyes and may mirror *pax3* expression in the
424 melanocyte stem cell in the skin.[72,73]
425
426 **Conditional deletion of *mitfa* in adult zebrafish fails to recapitulate germline loss-of-**
427 **function effects on tumor-free survival in GNAQ-driven melanoma.**
428
429 We next investigated whether the accelerated growth of GNAQ-driven tumors in *mitfa*-deficient
430 zebrafish, compared to wild-type animals, was due to an expansion of progenitor cells or the
431 cell-intrinsic loss of Mitfa activity. To this end, we performed conditional *mitfa* knockout
432 experiments using Strategy B plasmids in combination with either (1) non-targeting control
433 gRNAs or (2) gRNAs targeting exon 5 of *mitfa*. TEAZ-Skin was performed in three experimental
434 groups: (1) *casper* zebrafish (n=9) with gRNAs targeting *mitfa* (which controls for off-target
435 effects of the gRNA and for potential function of the *mitfa*$^{w2/w2}$ allele), (2) wild-type zebrafish
436 (n=9) with non-targeting (NT) gRNAs, and (3) wild-type zebrafish (n=9) with *U6*:gRNA-*mitfa*.
437 GFP expression was confirmed in all injected zebrafish (**Table S12**). Within 100 days post-
438 electroporation (dpe), tumors developed in 9/9 casper, 2/9 wild-type (+U6:gRNA-mitfa), and 2/9
439 wild-type (+U6:gRNA-NT) zebrafish (**Figure 4I-J**). Of note, *mitfa*-deficient tumors that formed in
440 wild-type or *casper* zebrafish developed distal metastases, an observation not seen in *mitfa*
441 wild-type TEAZ-Skin injected zebrafish (**Figure 4J, Figure S15**). Our findings support a model

442 in which failed differentiation as well as the expansion of melanocyte progenitor cells in *mitfa*-
443 deficient animals creates a permissive cellular environment for GNAQ-induced transformation
444 and reduced tumor latency.
445
446 **Transcriptional programs enriched in BRAF- versus GNAQ-driven melanoma overlap with**
447 **specific melanocyte progenitor populations.**
448
449 Oncogenic BRAF and NRAS are unable to promote transformation in the absence of *mitfa,*[29,32]
450 suggesting that distinct transcriptional programs, potentially reflecting unique cellular origins, are
451 required for UM and CM transformation. To address this hypothesis, we analyzed previously
452 published scRNA-seq datasets in transgenic *Tg(mitfa:BRAF^{V600E}): tp53$^{-/-}$* : *mitfa$^{w2/w2}$* zebrafish
453 where TEAZ-Skin was used to rescue *mitfa* and induce melanoma,[32] to our GNAQ-induced
454 tumors by TEAZ-Skin (**Figure 5A)**. We predicted that by analyzing primary tumors, the
455 transcriptional signature of the origin cell will be retained and can be identified by overlapping
456 gene signatures identified in the embryonic melanocyte lineage.[30] Interestingly, while the
457 expression of *mitfa* was significantly higher in GNAQ-positive tumors, the expression of
458 pigmentation genes; including *tyrp1b, dct, scl45a2, sox10* and *pmela* were significantly higher in
459 BRAF-positive melanoma (**Figure S16**). Genes enriched in GNAQ-UM and BRAF-CM were
460 identified by those with a Log2FC > 1 and Adj p-value < 0.0001 between the two tumor types
461 (**Figure 5B, Table S13**). We next overlapped this differential gene signature with genes
462 expressed by cells within the melanocyte lineage isolated from zebrafish embryos (**Figure 5C**).
463 As expected, BRAF-driven tumors strongly mapped to the melanoblast and melanophore
464 clusters (**Figure 5D**), supporting recent findings that BRAF-driven melanoma originates from
465 melanoblasts, a melanocyte progenitor population[32,74]. When comparing GNAQ-enriched genes
466 to the melanocyte lineage, we found that the signatures were not confined to a single cluster but
467 were distributed among neural crest cells, melanocyte progenitors, and xanthophore clusters

468 (**Figure 5D; Figure S17**). Such results support the hypothesis that GNAQ- and BRAF-driven
469 melanomas depend on distinct transcriptional programs, reflecting less and more differentiated
470 melanocytic states, respectively.
471
472 We next asked whether less differentiated melanocytes, similar to the *mitfa*-deficient progenitors
473 in *casper* eyes, are also present in adult wild-type eyes. Since melanocyte stem cells are known
474 to reside in the zebrafish skin,[28] we included skin tissue as a control and reclustered
475 melanocytes from wild-type skin and eyes with progenitor cells from *casper* eyes. Interestingly,
476 a subset of wild-type melanocytes from both eye and skin samples clustered closely with *casper*
477 progenitors (**Figure 5E, Figure S18**) and expressed pigment cell progenitor marker genes,
478 including *pax3a, sox10, foxd3,* and *tfec* (**Figure 5F**). These findings suggest either plasticity
479 among melanocytes within the eye or the existence of an eye melanocyte stem cell population
480 in adult wild-type zebrafish. Moreover, such cells may be more susceptible to transformation by
481 *GNAQ*^{Q209L} and could represent the cells of origin for UM tumors in this context.
482
483 **Discussion**
484
485 Herein, we present an immunocompetent zebrafish model of primary UM where tumors arise
486 within the choroid and progressively invade surrounding ocular structures. This model enables
487 the study of the earliest events of UM pathogenesis and how anatomical context impacts
488 disease progression. Notably, genes identified through our analysis correlate with survival
489 differences in human UM, highlighting the model's potential for mechanistic studies on gene
490 function in UM pathogenesis. Compared to transgenic models, our system produces
491 anatomically correct tumors at an accelerated rate, offering an efficient platform for studying UM
492 progression and therapeutic responses.
493

494 By generating UM tumors from the same anatomical location as the majority of human UM, we
495 were able to conduct key analyses such as the comparison of the tumor to untransformed
496 primary choroidal melanocytes and the tumor microenvironment. This method allowed for the
497 identification of genes that are upregulated in the tumor and therefore important for disease
498 onset and progression. Specifically, we found that fatty acid binding proteins, particularly *fabp3*,
499 are enriched in UM tumors. While lipid droplets have been identified as vulnerable targets in CM
500 and regulators of melanoma plasticity,[32,75] lipid signaling in UM has received limited attention.[76-
501 79] Interestingly, high expression of *FABP3* as well as *FABP5* associated with worse disease-free
502 survival in patients with UM but not in CM. Interestingly, our analysis also identified *LGALS2* and
503 *GCH*, two genes whose expression was strongly associated with worse overall survival in UM
504 but intriguingly showed the opposite in CM. Finally, we found greater *kita* expression in GNAQ-
505 driven tumors compared to choroidal melanocytes, a result that is particularly notable given
506 recent studies linking KIT-positive UM tumors with poor prognosis and monosomy of
507 chromosome 3.[80] Furthermore, expression of these genes was highest in TCGA molecular
508 classes 3 and 4 of the UM dataset, the subset of patients with the highest rates of metastatic
509 incidence and BAP1 loss.[55] Such observations show that this model can uncover genes that are
510 likely to have key, disease-specific roles in UM whose function could be further explored through
511 genetic perturbations in zebrafish. These genes could also be developed into new biomarkers of
512 disease risk to refine the identification of patients likely to progress to metastatic disease.
513
514 Although UM and CM both arise from cells within the melanocyte lineage, they differ
515 significantly in their biology and clinical outcomes. To explore how anatomical context influences
516 transcriptional states, we compared genetically identical tumors derived in the skin and eye and
517 found that eye-derived tumors display distinct expression profiles. To explore whether the
518 differences in tumors were due to inherent differences in their primary cells, we also compared
519 normal melanocytes from the eye and the skin. While we did find some transcriptional

520 distinctions between eye and skin melanocytes, these variances only represented a small
521 fraction of the differentially expressed genes between eye and skin melanomas. These results
522 suggest that the transcriptional profiles of genetically identical tumors in distinct anatomical
523 locations are influenced by more than the intrinsic differences in their origin cells, perhaps
524 varying due to signals from their unique microenvironments. Of the expression differences
525 between normal eye and skin melanocytes, GSEA pathway analysis revealed that skin
526 melanocytes are enriched for UV responses and DNA damage repair. Zebrafish, like humans,
527 have been shown to alter their melanin production in response to UV exposure.[81] Our results
528 suggest that skin melanocytes in the zebrafish may be more primed to enact UV-protective
529 functions than eye melanocytes, even with no UV exposure. Furthermore, the enrichment of
530 oxidative phosphorylation in eye melanocytes and of selenoamino acid metabolism in eye
531 tumors suggests metabolic differences between melanocytes derived from the eye or skin.
532 Interestingly, disruptions in selenoamino acid metabolism have been shown to adjust the TME
533 and growth of primary tumors in a number of cancers, including melanoma.[82] Pathway analysis
534 between skin and eye tumors has also revealed potential differences in the progression of these
535 tumors. Eye tumors were enriched for EMT genetic programs, suggesting that eye melanocytes
536 may exist in a more mesenchymal state than skin melanocytes or that greater expression of
537 EMT programs is necessary for metastatic spread out of the eye and towards distant sites like
538 the liver. On the other hand, skin tumors were enriched for the certain arms of the GNAQ
539 signaling cascade,[5,11-13] namely PI3K/AKT/MTOR signaling and RHO GTPases activating
540 formins. Further investigation is needed to confirm whether microenvironment differences or
541 anatomical origin of melanocytes can influence the relative importance of oncogenic pathways
542 in the setting of *GNAQ*^{Q209L} expression. Using our animal model to compare genetically identical
543 tumors, and their primary cells, across different anatomical sites has revealed distinct biological
544 behaviors, highlighting the model's potential for further investigations into site-specific tumor
545 biology and therapeutic strategies.

546 An interesting distinction between GNAQ and BRAF oncogenes is their differential dependency
547 on Mitfa activity for tumorigenesis. While BRAF^{V600E} requires Mitfa activity to induce
548 melanoma,[27,29] GNAQ^{Q209L}-driven tumor latency was significantly reduced in *mitfa*-deficient
549 zebrafish compared to wild-type controls. Our results are consistent with prior studies showing
550 that *mitfa*-deficient zebrafish activate distinct signaling pathways, favoring YAP over MAPK
551 signaling, and give rise to tumors with reduced latency compared to wild type tumors. Moreover,
552 manipulating YAP activity in wild-type animals was shown to recapitulate the enhanced growth
553 seen in *mitfa*-deficient tumors.[40] We observed high *yap1* expression in melanocyte progenitor
554 cells of *mitfa*-deficient zebrafish, suggesting that elevated Yap1 activity may be carried over
555 from the progenitor cell during transformation. While germline *mitfa* loss accelerates tumor
556 onset, our data suggest this effect is not solely due to the deletion of Mitfa from differentiated
557 melanocytes. Instead, we propose that germline *mitfa* deficiency expands a population of
558 *pax3a*- and *tfec*-positive melanocyte progenitor cells, which are more susceptible to GNAQ-
559 induced transformation. Notably, conditional loss of *mitfa* in differentiated melanocytes may
560 activate progenitor-like transcriptional programs, increasing their vulnerability to oncogenic
561 transformation. Alternatively, *mitfa* loss may impair the differentiation of melanocyte progenitors,
562 preventing the formation of GNAQ-positive nevi and promoting direct progression to malignancy.
563 Interestingly, these progenitor cells appear to maintain a neural crest signature, as evidenced by
564 the relatively high expression of additional markers such as *foxd3, pax3a, sox10,* and *tfec*.
565 [30,31,83-85] Together, these findings suggest that germline loss of *mitfa* accelerates GNAQ-driven
566 transformation of melanocyte progenitor cells by promoting their expansion and maintaining a
567 neural crest-like transcriptional profile. Identifying the transcriptional and signaling mechanisms
568 within *mitfa*-independent melanocyte progenitor cells that facilitate UM onset and progression
569 will have significant clinical implications, particularly for the differential diagnosis of high-risk
570 lesions and the rational design of targeted therapies.
571

572 Studies in human UM have shown that less pigmented tumor regions are more metastatic and
573 that BAP1-negative tumors exhibit a stem-like phenotype.[1,2,86,87] Our findings raise intriguing
574 questions about whether the progenitor cells observed in *mitfa*-deficient zebrafish are similarly
575 predisposed to a more undifferentiated, stem-like phenotype, contributing to their enhanced
576 transformation potential and aggressive tumor behavior. Interestingly, the direct comparison of
577 melanocytes and tumors from the eye or skin against their microenvironments revealed that skin
578 melanocytes overlap with the skin tumor greater than the overlap of eye melanocytes with the
579 skin tumor. However, this was not true in reverse with eye melanocytes being no more similar to
580 the eye tumor than skin melanocytes are. These findings suggest that eye tumors may originate
581 from a less differentiated cell compared to the melanocytic cell type that CM arises from. This
582 progenitor cell may be underrepresented in the normal eye melanocyte population, leading to
583 the observed lower transcriptional overlap between total enriched genes in eye tumors and
584 normal eye melanocytes. Furthermore, re-clustering of normal WT melanocytes and melanocyte
585 progenitor cells from *mitfa*-deficient zebrafish demonstrates that both the eye and skin have
586 melanocyte populations that cluster closely with melanocyte progenitors. These melanocyte
587 populations may be less differentiated as evidenced by increased expression of *pax3a*, *tfec*, and
588 *foxd3*. Whether this subset of melanocytes represents bona fide melanocyte stem cells or
589 melanocytes that can oscillate between differentiation states within the eye remains to be
590 uncovered.
591
592 Furthermore, differences in *mitfa* dependency between BRAF-driven CM and GNAQ-driven UM
593 suggest fundamental distinctions in their cellular origins. Although MITF-independent
594 melanocytic cells are unlikely to be the cellular origin of CM in zebrafish models, studies have
595 shown that MITF-independent BRAF-positive melanoma cells are central to disease
596 recurrence[45]. Our results highlight that *mitfa* expression does not directly reflect Mitfa activity, as
597 *mitfa*-target genes are more highly expressed in BRAF-positive melanoma despite lower *mitfa*

598 expression compared to GNAQ-positive melanoma. GNAQ-driven transformation may be
599 facilitated by Mitfa paralogs such as Tfec and Tfeb. The Mitfa paralog Tfec has been shown to
600 activate pigmentation genes in both the retinal pigment epithelium and melanocyte progenitor
601 cells. Tfec can also rescue ectopic melanocytes in *nacre* zebrafish embryos.[31,33] Moreover, we
602 have recently shown that the MITF paralog TFE3 promotes cellular plasticity and stemness
603 genes in MITF-low melanoma cells,[88] suggesting that MITF paralogs are compelling candidate
604 transcription factors in UM pathogenesis.
605
606 Although understudied, the choroidal stroma is abundant in fibroblasts that produce various
607 ECM proteins, including collagen, elastin, laminin, fibrin and fibronectin.[89-92] This
608 microenvironment differs from that of the keratinocyte-rich epidermis where CM arises. The
609 differences in TME between UM and CM are likely to play an important role in the phenotypic
610 differences observed in these tumors. Recent studies show that increased fibronectin promotes
611 a less differentiated and more mobile phenotype in murine melanocytes *in vitro*.[93] Our finding
612 that fibronectin (*fn1a* and *fn1b)* was upregulated in CAFs compared to normal fibroblasts
613 provides evidence that fibronectin may promote invasiveness or dedifferentiation in a malignant,
614 *in vivo* context. Similar to other studies finding an accumulation of collagen I in the TME of
615 various cancer types, we found upregulation of *col1a1b* and *col1a2* in CAFs relative to normal
616 fibroblasts, indicating increased collagen I deposition.[59,60] The precise mechanism of how
617 different subclasses of CAFs regulate UM differentiation state and propensity to metastasize
618 through ECM remodeling is still to be defined.
619
620 Another explanation for decreased tumor latency in *casper* zebrafish is that the global loss of
621 *mitfa* could have secondary effects on other cell types, such as immune cells, which may
622 influence tumor behavior. Furthermore, the presence of xanthophore, iridophore, and
623 melanophore markers within UM tumor cells raises the possibility of a pluripotent progenitor

624 population. This model also enables us to examine whether differences in differentiation
625 potential contribute to tumor aggressiveness, as *casper* fish may exhibit more pronounced
626 tumor acceleration due to the simultaneous blockade of two chromatophore differentiation
627 pathways compared to single-pathway inhibition in *nacre* fish.
628
629 Our findings open numerous avenues for future research. This model can be used to study the
630 effects of *BAP1* loss and other secondary mutations commonly associated with UM, such as
631 *EIF1AX* and *SF3B1*. It also provides a platform for investigating metastatic events, as tumors
632 emerge in defined primary sites. Establishing zebrafish UM cell lines from different anatomical
633 locations and genetic backgrounds could offer further insights into the role of microenvironment
634 and *mitfa* dependency in UM progression. Additionally, characterizing the melanocyte progenitor
635 population in the eye and determining if a similar population exists in mammals could provide
636 critical insights into uveal stem cell biology. While we identified a population of Pax3-positive
637 cells in the mouse limbus, it remains to be determined if these cells are sensitive to oncogenic
638 GNAQ transformation.
639
640 **Limitation of study**
641
642 The use of *tp53* and *ptena/b* mutations in our UM model does not fully recapitulate the genetics
643 of human UM. Mutations in *TP53* and *PTEN* are rarely observed in UM, where loss-of-function
644 mutations in *BAP1* represent the most frequent tumor suppressor alteration.[67,94,95] However,
645 both *TP53* and *PTEN* signaling pathways have been shown to be altered in UM pathogenesis.
646 *MDM2* overexpression, an upstream negative regulator of p53, and downregulation of *PERP*, a
647 downstream effector of p53, have been demonstrated in many UM patients and are associated
648 with worse outcome.[96-100] Studies have also shown that over half of UM tumors have decreased
649 PTEN immunostaining and its loss is correlated with decreased survival.[67-69] Nevertheless,

650 whether genetic knockout of these tumor suppressors recapitulate the dysregulation of these
651 pathways in human UM remains an open question. Another limitation to our approach when
652 examining the differences between genetically identical skin and eye-derived tumors is the
653 inability to distinguish between purely microenvironmental effects and differences in cell of origin
654 (melanocytes in the skin versus in the eye). To address this question, a syngeneic or
655 immunodeficient model could be applied to transplant cells from a primary UM tumor into both
656 anatomical sites. Additionally, our use of the *mitfa* promoter to drive oncogene expression
657 presents a challenge in defining the exact cell of origin, as this promoter is active in both
658 melanocyte progenitors and differentiated melanocytes. As such, it remains unclear whether
659 tumors in *mitfa* wild-type fish (or those with conditional *mitfa* deletion) arise from a progenitor or
660 a mature melanocyte. Lineage tracing studies will be essential to determine whether
661 differentiated melanocytes possess the capacity to initiate primary UM in *mitfa*-competent or
662 conditional *mitfa*-KO zebrafish.
663
664 **Resource availability**
665
666 **Lead contact**
667 Requests for further information and resources should be directed to, and will be fulfilled by, the
668 lead contact, Colin Kenny, PhD (colin-kenny@uiowa.edu).
669
670 **Materials availability**
671 Plasmid constructs and zebrafish generated in this study may be obtained by a request to the
672 lead contact.
673
674 **Data and code availability**
675

Datasets generated in this article are available from NCBI GEO accession number GEO: GSE307227. This study does not report original code. Any additional information required to reanalyze the data reported in this work paper is available from the lead contact upon request.

Acknowledgments

This project was supported by grants from the Holden Comprehensive Cancer Center (HCCC; P30- CA086862) at the University of Iowa. Additional support came from an institutional research grant from the American Cancer Society, administered through the HCCC, to C.K. (IRG-18-164-43) and from the Melanoma Research Alliance (ID#1426690) to C.K. Additional support came from the National Institutes of Health (NIH) to R.A.C. (R01-AR062457). JY and DR were supported by predoctoral fellowships from the National Institutes of Health (T32 GM144636 and T90 DE023520, respectively). Additional support came from the Leo Foundation (LF-OC-21-000888) to DL. The funders had no role in study design, data collection and analysis, decision to publish, or preparation of the manuscript. We gratefully acknowledge Dr. Richard White from Oxford University, UK. for providing mitfa-Cas9, *U6*:gRNA-*ptena*, *U6*:gRNA-*ptenb* and *U6*:gRNA-*tp53* plasmids constructs and for providing critical comments to successfully preform TEAZ experiments. We additional acknowledge Dr. Jacqueline Lees and Dr. Adam Amsterdam from the Koch Institute for Integrative Cancer Research at MIT for generously providing *mitfa*:*GNAQ*^{Q209L}; *mitfa*:GFP plasmid constructs to induce UM tumors.

Author contributions

Conceptualization: C.K. Methodology: J.I.Y., D.R., R.M., Z.L., K.R.C-H., D.G., J.D.R., S.P.G.M., D.F., I.O.T. Investigation/data analysis: J.I.Y., D.R., R.M., Z.L., K.R.C-H., D.G., J.D.R., A,J,D., S.P.G.M., D.F., I.O.T., C.K. Visualization and data interpretation: J.I.Y., D.R., R.M., Z.L., K.R.C-H., D.G., S.P.G.M., D.F., I.O.T. D.L., R.J.W., and C.K. Funding acquisition: R.A.C., D.L., C.K.

Project administration: C.K. Supervision: C.K. Writing—original draft: J.I.Y., and C.K. Writing—review and editing: J.I.Y., D.R., C.M., E.M.B., D.L., R.J.W., and C.K. Approval of submission: J.I.Y., R.M., Z.L., K.R.C-H., D.R., D.G., S.P.G.M., C.M., D.F., J.D.R., A,J,D., I.O.T. R.A.C., E.M.B., D.L., R.J.W., and C.K. Accountable for contributions: J.I.Y., D.R., R.M., Z.L., K.R.C-H., D.G., C.M., S.P.G.M., D.F., J.D.R., A,J,D., I.O.T. R.A.C., E.M.B., D.L., R.J.W., and C.K.

Declaration of interests

The authors declare no competing interests.

711 **Methods**

712 **Experimental model and study participant details**

713

714 **Zebrafish husbandry**

715

716 All zebrafish used in this study were bred and maintained at the University of Iowa Animal Care
717 Facility. The zebrafish are kept consistently at 28°C, 7.4 pH, and controlled salt concentrations
718 and cyclically receive 14 h of light followed by 10 hours of darkness. All zebrafish experiments
719 were performed in compliance with the ethical regulations of the Institutional Animal Care and
720 Use Committee at the University of Iowa and in compliance with NIH guidelines (protocol
721 #3022523). Zebrafish embryos were maintained at 28.5°C and staged by hours or days post-
722 fertilization (hpf or dpf).

723

724 **Zebrafish mutant lines**

725

726 Wild-type zebrafish in this study include the *AB* line and the *WIK* line. Transgenic lines include
727 *casper* (*mitfa*$^{w2/w2}$; *mpv17*$^{-/-}$)[46,47], *nacre* (*mitfa*$^{w2/w2}$)[43], *Tg*(*mitfa*:GFP)[18], and *Tg*(*mitfa*:GFP);
728 *mitfa*$^{w2/w2}$. TEAZ-Eye and TEAZ-Skin was performed on adult zebrafish (greater than 4 months
729 postfertilization).

730

731 **Cloning**

732

733 The MiniCoopR[29] vector (MiniCoopR 2x*U6*:gRNA, *mitfa*:Cas9 was a gift from Leonard Zon
734 Addgene plasmid # 118844) was modified to replace the *mitfa* coding sequence with *GNAQ*^{Q209L}
735 by removing *mitfa* using StuI and SmaI restriction enzymes (NEB). Gibson assembly was used
736 to insert *GNAQ*^{Q209L}:T2A:GFP DNA as a gBlock hifi (IDT) with sequence on the 3'

737 (GAAGCTAACACATAGTTGAAC) and 5' (CAATGCCAACTAAATTTCATG) as overhangs.
738 Gibson assemblies were transformed using NEB 5-alpha competent *E. coli* cells via heat shock.
739 *GNAQ*^{Q209L}:T2A:GFP insertion was confirmed using Sanger sequencing (Primers:
740 CAAGGAAGCCCGGCGGATCAACGA, CATACTTGTATGGGATCTTGAGTGTGTCCA,
741 GTGGAGTCAGACAATGAGAACCGAATGGAG, CAAGCTGGAGTACAACTACAA).
742
743 *mitfa* sgRNA was designed using IDT's CRISPR-Cas9 guide RNA design tool (sequence:
744 ATGGACAAAGCTGGACCATG). *U6*:sgRNA-*ptena* was linearized by PCR (forward primer:
745 GTTTAAGAGCTATGCTGGAAACAGCAT, reverse primer: GAACAAAGAGCTGGAGGGAG).
746 Linear plasmid was purified from a 2% agarose gel using the Monarch GNA Gel Extraction Kit
747 (#T1020S). ssDNA sequences for sgRNA-*mitfa* were annealed together in NE buffer r2.1.
748 Gibson assembly was used to insert sgRNA-*mitfa* into linearized U6 plasmid. Assembled
749 product was transformed into NEB 5-alpha competent *E. coli* cells via heat shock and selected
750 with 50 ug/mL streptomycin. Insertion of sgRNA-*mitfa* was confirmed using PCR amplification of
751 lysed bacteria from single colonies (forward primer: ATGGACAAAGCTGGACCATG, reverse
752 primer: CTTAGCTGGATAACGCCAC). Positive products were isolated using the QIAGEN
753 Plasmid Maxi Kit. Entire plasmid was sequenced using Plasmidsaurus sequencing service.
754
755 **Transgene Electroporation of Adult Zebrafish Skin (TEAZ-Skin)**
756
757 Adult zebrafish were anesthetized in 0.2% Tricaine prior to upright placement on a prewetted
758 Kimwipe. Each injection consisted of 1000 ng total DNA: 100 ng of Tol2 plasmid and an equal
759 division of the remaining 900 ng for the remaining constructs. Injection stocks contained a small
760 volume (<1uL, 1:50 dilution) of green food coloring to visualize localization of injection. Injection
761 volumes ranged from 1 to 1.5 uL depending on the injection mix, keeping 1000 ng total
762 constant. Needles were pulled from 10 cm long filamented borosilicate glass capillaries at a

763 pressure of 500, heat of 650, pull strength of 100, velocity of 200, and time delay of 40 in a
764 Model P-97 Flaming/Brown micropipette puller from Sutter Instrument Co. Following injection,
765 zebrafish were immediately electroporated (<1 min) by placing the cathode probe of ultrasound
766 gel-coated Platnium Tweezertrode, 3MM, on the side of the injection site and the anode probe
767 on the other side of the fish body. Electroporation was achieved with 5 60-ms pulses of 40 volts
768 with a 1s pulse interval from a ECM 830 Electro Square Porator from BTX Harvard Apparatus.
769 Following electroporation, zebrafish are placed into a recovery tank with fresh, gently stirred
770 system water and are monitored until normal swimming resumes. Electroporated zebrafish are
771 imaged weekly. *mitfa*:*GNAQ*^{Q209L}; *mitfa*:GFP plasmid constructs were kindly provided by Dr.
772 Jacqueline A. Lees (Massachusetts Institute of Technology, Cambridge, USA). *mitfa*:Cas9,
773 *mitfa:*tdTomato, PCS2FA Tol2, *U6*:gRNA-*tp53, U6*:gRNA-*ptena,* and *U6*:gRNA-*ptenb* plasmids
774 were kindly provided by Dr. Richard White (Sloan Kettering Institute, New York, USA).
775
776 **Transgene Electroporation of Adult Zebrafish Eye (TEAZ-Eye)**
777
778 Pre-injection preparation for eye injections is the same as for skin injections including: 0.2%
779 Tricaine anesthesia, needle size, and injection concentrations. To inject the eye, a blunt
780 spherical head of a pin was gently pressed against the bottom half of the zebrafish eyeball to
781 reveal the dorsal posterior regions of the eye. The needle was gently pressed into this location,
782 where the cornea is softer, just through the sclera, keeping the needle as superficial as possible
783 as to not damage the back of the eye. Injection volumes were around 0.25 uL and were
784 terminated with a slight visual swelling of the eye. Following injection zebrafish were
785 immediately electroporated (<1 min) by the cathode probe of ultrasound gel-coated Platnium
786 Tweezertrode, 1MM, on the superior side of the eye nearest the injection and the anode probe
787 on the inferior side of the eye. Electroporation was achieved with 3 50-ms pulses of 75 volts with

788 a 1s pulse interval from a ECM 830 Electro Square Porator from BTX Harvard Apparatus.
789 Recovery and imaging procedures for these fish did not differ from the skin injections.
790
791 **Imaging and image processing**
792
793 Injected zebrafish were imaged using an upright Leica M205 FCA microscope with brightfield
794 and GFP filters. Zebrafish were briefly anesthetized with 0.2% Tricaine and positioned on a
795 Kimwipe mound for upright orientation. Images were taken and processed through the LAS X
796 software. All histology slides were imaged using brightfield, DAPI, and GFP filters on an EVOS
797 M5000 microscope from Invitrogen for individual images or on a Leica DMi8 microscope and
798 stitched together by LAS X Thunder Imaging software for full tissue images.
799
800 **H&E and IF – zebrafish tissue**
801
802 Whole zebrafish or zebrafish eyes were fixed in 4% paraformaldehyde for 48 hours at 4°C and
803 paraffin embedded in the University of Iowa Pathology Core. Fish were sectioned at 7 μM
804 thickness and placed on Superfrost Plus Microscope slides from Fisher Scientific, baked at
805 60°C, stained with hematoxylin and eosin, and mounted with Cytoseal 60 from Epredia. For
806 immunofluorescence, sections were deparaffinized and hydrated followed by heat-induced
807 antigen retrieval with 10 mM Na-citrate buffer and blocking with 3% milk in 0.1% Tween 20.
808 slides were stained with primary antibodies against GFP (NB600-308 Rabbit anti-GFP
809 polyclonal from Novus Biologicals at 1:250) overnight at 4°C and then fluorescent secondary
810 antibodies against rabbit IgG (Alexa Fluor 488 goat anti-rabbit IgG at 1:500 from a 2 mg/mL
811 stock) for 1 hr at room temperature. RPE autofluorescence was minimized using the Vector
812 TrueVIEW Autofluorescence Quenching Kit. Sections were counterstained with DAPI, mounted
813 using VECTASHIELD Vibrance Antifade Mounting Medium, and imaged the same day.

814

815 **IF - mouse eye tissue**

816

817 C57BL/6 mice eyes were collected, formalin-fixed, paraffin-embedded, and sectioned into 7 μm-
818 thick sections. Sections were deparaffinized and hydrated followed by heat-induced antigen
819 retrieval with citrate buffer (Vector Laboratories, Inc.), permeabilized with 1% horse serum in
820 0.2% Triton-X, blocked with 5% Horse serum in 0.2% Triton-X, and incubated with PAX3 primary
821 antibody (1:200 anti-rabbit, Invitrogen, 38-1801) overnight at 4°C. Samples were incubated with
822 DyLightTM 488-labeled secondary antibody (1:2000, horse anti-rabbit. Vector Laboratories, Inc.
823 DI-1088-1.5) for 1 hr at room temperature, treated with autofluorescence quenching kit (Vector
824 Laboratories, Inc. SP-8400-15), and cover slips fitted using Vectashield Antifade Mounting
825 Medium with DAPI (Vector Laboratories, Inc. H-1000-10).

826

827 **Kaplan-Meier analysis**

828

829 Zebrafish were followed for up to 70 weeks and tumor-free survival was analyzed with the
830 Kaplan-Meier method. Tumors were defined as the first presence of a GFP-positive nodular
831 mass at the injection site. Differences between injection groups were analyzed using log-rank
832 statistics.

833

834 **Single cell suspension and single-cell RNA Seq analysis**

835

836 Zebrafish were euthanized with 0.4% Tricaine for 10 mins followed by immersion in ice water
837 until no opercular movement was observed for at least 30 min as detailed in our IACUC
838 protocol. Tumors were harvested and minced into small pieces. Minced tumors were digested
839 for 1 hour at 37°C with collagenase and hyaluronidase in HBSS with 2% FBS (HF).

840 Suspensions were washed with 1:4 HF:NH_4Cl and then further digested for 5 min with pre-
841 warmed trypsin. Following trypsin inactivation, cell suspensions were washed twice with 10%
842 FBS in HBSS.
843
844 Cellular suspensions were loaded on a 10x Genomics Chromium instrument to generate single-
845 cell gel beads in emulsion (GEMs). Approximately 10,000-20,000 cells were loaded per channel
846 depending on the 10x kit used. See figures S5 and S12 for kit information per sample.
847 Next GEM kit: targeted cell number = 10,000. Single-cell RNA-Seq libraries were prepared
848 using Single Cell 3′ Reagent Kits v2: Chromium Single Cell 3′ Library & Gel Bead Kit v2, PN-
849 120237; Single Cell 3′ Chip Kit v2, PN-120236; and i7 Multiplex Kit, PN-120262 (10x Genomics)
850 and following the Single Cell 3′ Reagent Kits v2 User Guide (Manual Part # CG00052 Rev A).
851 GEM-X kit: targeted cell number = 20,000. Single-cell RNA-Seq libraries were prepared using
852 Chromium GEM-X Single Cell 3′ Reagent Kits v4: Library Construction Kit C, PN-1000694;
853 Single Cell 3’ GEM Kit v4, PN-1000693; Single Cell 3’ Gel Bead Kit v4, PN-2001128; and Dual
854 Index Kit TT Set A, PN-3000431; and following the Chromium GEM-X Single Cell 3′ Reagent
855 Kits v4 User Guide (Manual Part # CG000731 Rev B). Libraries were sequenced on an Illumina
856 HiSeq 4000 as 2 × 150 paired-end reads. Sequencing results were demultiplexed and converted
857 to FASTQ format using Illumina bcl2fastq software.
858
859 A custom reference genome for the Zebrafish was constructed with GRCz11 primary assembly
860 (Ensembl) using Cell Ranger (Cell Ranger mkref function). 10X Genomics scRNA-seq reads
861 were then processed and aligned to this reference with Cell Ranger (Cell Ranger Count
862 function). Further analysis and visualization was performed using Seurat (v4.1.0)[101], cells with
863 fewer than 200 RNA feature counts and greater than 5% mitochondrial contamination were
864 removed with filtering (greater than 15% for wildtype eye samples). RNA counts were
865 normalized, and FindVariableFeatures was run with the following parameters: selection.method

866 = “vst”, nfeatures = 2,000. The cells were originally clustered in a UMAP by RunPCA then
867 RunUMAP with dims 1:30. FindNeighbors was run with dims 1:30 followed by FindClusters
868 using a resolution of 0.4. These methods identified up to 20 clusters in individual samples.
869
870 For comparative analysis, RNA-seq datasets were integrated together using IntegrateData with
871 dims 1:30. New clusters were generated as before. Clusters were annotated using
872 FindAllMarkers and the top 25 enriched genes in each cluster were compared to the Daniocell
873 dataset[52] and Spectacle[49]. Cluster names were given according to the closest matched cellular
874 population between these two datasets. To determine enriched pathways, *danio rerio* gene
875 names were converted into human Ensembl gene codes with g:Profiler[102] and then data were
876 analyzed with the use of QIAGEN IPA (QIAGEN Inc)[103] and GSEA[104,105]. Pseudotime was
877 performed using Monocle3 (v0.2.3.0)[106].
878
879 **Verification of sgRNAs**
880
881 Zebrafish were euthanized with 0.4% Tricaine for 10 mins followed by immersion in ice water
882 until no opercular movement was observed for at least 10 min as detailed in the IACUC
883 protocol. Tumors were harvested and minced into small pieces. DNA was harvested according
884 to the DNeasy Blood and Tissue Kit from Qiagen. Regions surrounding cut sites were PCR-
885 amplified and the purity of the PCR amplicon was confirmed with agarose gel electrophoresis.
886 Samples were cleaned up with the QIAquick PCR Purification Kit from Qiagen and sent for
887 Sanger sequencing at the Iowa Institute of Human Genetics. Gene editing was confirmed with
888 DECODR INDEL analysis by comparing to wildtype sequence[107]. PCR primer sequences follow:
889 *mitfa* PCR F: CCGGTATGTATTCACATTGTCTTG
890 *mitfa* PCR R: TCTTGCTTAGGATGCCTATGTATT
891 *ptena* PCR F: CATCCCACCAAGTGAGGTTAAAC

892 *ptena* PCR R: CACATACACAGTCAAGGGTGAG

893 *ptenb* PCR F: CAGTTCTGTTGCACCCAATAAG

894 *ptenb* PCR R: CTGGTGGTGTTGAGGCTATAAAG

895 *tp53* PCR F: AAGTATTCAGCCCCCAGGTG

896 *tp53* PCR R: CGCTTTTGACTCACAGTGCAAG

897 **Figure 1: *GNAQ*^{Q209L}-induced melanoma by TEAZ-Skin and TEAZ-Eye.**

898 (**A**) TEAZ-Skin was used to induce GNAQ-positive melanoma using two strategies. Strategy A
899 involves a single plasmid construct containing expression cassettes driven by the *mitfa*
900 promoter for GNAQ^{Q209L}-T2A-eGFP and Cas9, as well as a U6 promoter driving the expression
901 of three separate gRNAs (targeting *tp53*, *ptena*, and *ptenb*, or a non-targeting control). Strategy
902 B uses a multi-plasmid approach with five plasmids for TEAZ-Skin. Expression cassettes
903 include: (a) *mitfa*:*GNAQ*^{Q209L}-*mitfa*:eGFP, (b) *mitfa*:Cas9, (c) *U6*:gRNA (*tp53*), (d) *U6*:gRNA
904 (*ptena*), and (e) *U6*:gRNA (*ptenb*).

905 (**B**) Schematic of TEAZ-Skin using wild type (*AB*), *nacre* (*mitfa*$^{w2/w2}$) and *casper* (*mitfa*$^{w2/w2}$*:*
906 *mpv17*$^{a9/a9}$) zebrafish lines.

907 (**C**) TEAZ-Skin using Strategy B plasmids in adult wild-type (*AB*) and *casper* zebrafish.
908 Representative brightfield and fluorescent images shown at 4, 8, and 12 weeks post
909 electroporation for WT and at 2, 4, and 8 weeks for *casper*.

910 (**D**) Kaplan-Meier curves were used to estimate tumor-free survival, defined as the time from
911 electroporation until the first visible appearance of GFP+ nodular tumors, in adult zebrafish via
912 TEAZ-Skin. Strategy B wild-type (n=7), *nacre* (n=5), and *casper* (n=17) curves and TEAZ-Skin
913 (*GNAQ*^{Q209L}:GFP) curves (n=3 per condition) compared pairwise with logrank (Mantel-Cox) test.
914 ns = not significant, * p-value<0.05; ** p-value<0.01; ***p-value<0.001; ****p-value<0.0001.

915 (**E**) Schematic of the zebrafish eye, dashed box indicates the retina and choroid. Hematoxylin
916 and eosin (H&E) staining of a wild-type zebrafish eye at 20× magnification, showing the retina
917 and choroid. Eye structures are labeled, including choroidal melanocytes.

918 (**F**) Immunofluorescent analysis of transgenic *Tg(mitfa:GFP)* zebrafish using an anti-GFP
919 antibody. Sections were counterstained with DAPI to visualize nuclei. Representative image
920 showing GFP expression in *mitfa*-positive cells. Secondary-only antibody was used as
921 background control.

922 (**G**) Schematic of TEAZ-Eye using choroidal targeted injection.

923 (**H-H'**) Live imaging of adult wild-type zebrafish following TEAZ-Eye with Strategy B plasmids to
924 induce uveal melanoma. Brightfield imaging and the corresponding GFP fluorescence images
925 highlighting tumor progression. Timepoints in day post-electroporation (dpe) as labeled.
926 (**I-I'**) Live imaging of adult *casper* zebrafish over 21 days post-electroporation (dpe) using TEAZ-
927 Eye with Strategy B plasmids to induce uveal melanoma. Brightfield imaging and the
928 corresponding GFP fluorescence images highlighting tumor progression.
929 (**J**) Kaplan-Meier curves comparing tumor-free survival among wild-type (n=5) and *casper*
930 (n=10) zebrafish following TEAZ-Eye induction using Strategy B plasmids. Curves compared
931 pairwise with logrank (Mantel-Cox) test. ** p-value<0.01.
932 (**K, K'**) H&E analysis of uveal melanoma in *casper* zebrafish induced by TEAZ-Eye. Images
933 were acquired at 20× magnification and stitched from 85 fields using Thunder imaging software.
934 Normal eye tissue and uveal melanoma as labeled.
935 (**K'**) Representative 40x magnification image showing GFP expression in tumors cells after anti-
936 GFP immunofluorescent analysis of TEAZ-Eye induced uveal melanoma in *casper* zebrafish.
937
938 **Figure 2: Single cell profiling of uveal melanoma and the TME in adult zebrafish.**
939 (**A**) UMAP representation of single-cell RNA-Seq (scRNA-seq) data from three dissociated wild-
940 type eyes harboring uveal melanoma (UM) that were generated by TEAZ-Eye (sequencing
941 replicates, n=2), and control eyes consisting of four pooled sibling-matched wild-type eyes, and
942 two tumor paired control eyes (sequencing replicates, n=2). Annotated cell clusters as labeled.
943 (**B**) UMAP and feature plot showing *eGFP* and *GNAQ*^{Q209L} expression in control eyes and UM
944 tumor. Red dotted line highlights the melanocyte and UM clusters.
945 (**C**) Comparison of UM tumor marker genes with the markers of cell types within the control eye
946 microenvironment. Only genes with a log2FC > 1 and q-value < 0.01 were included in the
947 analysis.

948 (**D**) Dot plot representing enriched genes (log2FC > 1; q-value < 0.01) in choroidal cell
949 populations, UM tumors cells, immune cell populations, fibroblasts, Schwann cells, pericytes,
950 and vascular endothelial cells as shown. Dot size indicates the percentage of cells expressing
951 each gene; color intensity (grey to blue) reflects normalized average expression levels (low to
952 high).
953 (**E**) UMAP clustering of cells in the choroidal microenvironment. Annotated cell clusters as
954 labelled.
955 (**F**) Comparison of relative cluster sizes between the two conditions, control and TEAZ-Eye,
956 shown in (E). Schwann cells serve as a control cluster, displaying no change in frequency
957 between conditions. Gray = TEAZ-Eye, Blue = Control.
958 (**G**) Venn diagram representing the overlap of genes between UM tumors and choroidal
959 melanocytes compared to the cells in their respective microenvironments. Enriched genes for
960 each condition were identified by differential expression analysis comparing melanocytes to the
961 microenvironment (ME) or tumor cells to the tumor microenvironment (TME), using a threshold
962 of log2FC > 1 and q-value < 0.01. Genes of interest have been labelled in their respective
963 subsets. (**G'**) HOMER promoter motif enrichment analysis of genes enriched in UM tumors vs
964 TME. The top ranked motif for "known" and "*de novo"* motifs are shown with their corresponding
965 p-values.
966 (**H)** Dot plot showing enriched genes (log2FC > 1; q-value < 0.01) in UM tumor cells, choroidal
967 melanocytes, or the tumor microenvironment (TME). Dot size indicates the percentage of cells
968 expressing each gene; color intensity (grey to blue) reflects normalized average expression
969 levels (low to high).
970 (**I-K**) Kaplan–Meier disease-free survival and overall survival curves generated using uveal
971 melanoma TCGA data. Patients stratified by relative expression levels of *KIT*, *FABP3*, or
972 *LGALS2*. Gene expression thresholds were defined by median expression within each cohort.
973 Log rank p-values as shown. Dotted lines represent 95% confidence interval.

974 (**L**) Dot plot showing enriched genes (log2FC > 1; q-value < 0.01) in cancer-associated
975 fibroblasts (CAF), normal fibroblasts (NF), or the tumor microenvironment (TME) without CAF.
976 Dot size indicates the percentage of cells expressing each gene; color intensity (grey to blue)
977 reflects normalized average expression levels (low to high). Genes have been grouped
978 according to their labelled functions.
979
980 **Figure 3: Comparison of GNAQ-driven tumors and primary melanocytes in the skin and**
981 **eyes of adult zebrafish.**
982 (**A**) UMAP representation of GNAQ-positive tumors generated using TEAZ-Eye and TEAZ-Skin,
983 along with their respective control tissues using scRNA-seq. Tumor samples include three
984 dissociated wild-type eyes harboring UM tumors generated via TEAZ-Eye and two dissociated
985 wild-type skin UM tumors generated via TEAZ-Skin (n=2 sequencing replicates). Control eye
986 samples consist of a pool of two uninjected tumor paired wild-type eyes, three mock-injected
987 sibling-matched wild-type eyes, and four uninjected sibling-matched wild-type eyes (n=3
988 sequencing replicates). Control skin samples consist of dissociated normal skin from two wild-
989 type zebrafish (n=2 sequencing replicates). Cell clusters are annotated as tumor cells (red),
990 tumor microenvironment (TME) cells shared by both eye and skin samples (light gray), and TME
991 cells specific to the eye samples (dark gray).
992 (**B**) Live imaging of representative samples used for single-cell RNA-Seq analysis and Venn
993 diagram showing overlapping genes between TEAZ-Eye, TEAZ-Skin, choroidal melanocytes,
994 and skin melanocytes compared to the cells in their respective microenvironments. Enriched
995 genes for each condition were identified by differential expression analysis comparing
996 melanocytes to the microenvironment (ME) or tumor cells to the tumor microenvironment (TME),
997 using a threshold of log2FC > 0.5 and q-value < 0.01.
998 (**C**) Table displaying overlaps between enriched gene sets from (B). Percentages represented
999 as the number of overlapping genes over the total unique genes of both gene sets.

1000 (**D**) UMAP representation of primary melanocytes and UM tumor cells from both eye (salmon)
1001 and skin (teal).
1002 (**E**) Volcano plot of differentially expressed genes (DEGs) between eye and skin primary
1003 melanocytes (log2FC > |0.5| and q-value < 0.01).
1004 (**F**) Volcano plot of differentially expressed genes (DEGs) between eye and skin UM tumors
1005 (log2FC > |0.5| and q-value < 0.01).
1006 (**G**) GSEA enrichment plots of pathways that were enriched in skin melanocytes and of
1007 pathways enriched in eye melanocytes from (E). P-values and FDRs as labelled.
1008 (**H**) GSEA enrichment plots of pathways that were enriched in UM skin tumors and of pathways
1009 enriched in UM eye tumors from (F). P-values and FDRs as labelled..
1010
1011
1012 **Figure 4: *mitf*-independent melanocyte progenitor cells are expanded in *mitfa*-deficient**
1013 **zebrafish and are susceptible to *GNAQ*^{Q209L} transformation.**
1014 (**A**) H&E analysis representation of the retina and choroid in wild-type (left), *nacre* (middle), and
1015 *casper* (right) zebrafish (20x magnification). Note the loss of melanocytes (red arrows) in the
1016 choroid of *nacre* and *casper* eyes. “Vit” = vitreous, “GCL” = ganglion cell layer, “INL” = inner
1017 nuclear layer, “ONL” = outer nuclear layer, “POS” = photoreceptor outer segment, “RPE” =
1018 retinal pigmented epithelium, “CH” = choroid.
1019 (**B**) Immunofluorescent analysis of transgenic *Tg(mitfa:GFP); mitfa*$^{w2/w2}$ (*nacre*) zebrafish using
1020 an anti-GFP antibody. Sections were counterstained with DAPI to visualize nuclei.
1021 Representative images showing GFP-positive cells in the ciliary body and choroid are shown by
1022 yellow arrow heads. Secondary-only antibody was used as background control.
1023 (**C**) UMAP representation of single-cell RNA sequencing (scRNA-seq) data from three paired
1024 dissociated *casper* eyes and from three *casper* eyes harboring uveal melanoma (UM) tumors
1025 induced using Strategy B via TEAZ-Eye (n=1 sequencing replicate for each). Annotated cell

1026 clusters are labeled. Progenitor cells and UM tumor clusters are outlined with dashed red lines.
1027 Representative brightfield images of a normal eye and a UM tumor in *casper* zebrafish are
1028 shown in the top left corner of the UMAP.
1029 (**D**) Re-clustered UMAP representing progenitor cells from control eyes and uveal melanoma
1030 (UM) tumor cells from TEAZ-Eye–injected *casper* zebrafish. Heterogeneous cell populations as
1031 labeled.
1032 (**E**) Re-clustered UMAP from (D) showing melanocyte progenitor cells from control eyes in red
1033 and UM tumor cells from TEAZ-Eye in blue. Feature plots for *pax3a, foxd3* and *sox10*
1034 expression are shown, dashed line marks the progenitor cell population.
1035 (**F**) Dot plot illustrating differentiational expressed genes (log2FC > 0.5; q-value < 0.05)
1036 between heterogeneous cell populations in (D). Dot size indicates the percentage of cells
1037 expressing each gene; color intensity (blue to red) reflects normalized average expression
1038 levels (low to high).
1039 (**G, G'**) UMAP obtained after clustering GFP-positive cells sorted from *Tg(mitfa:GFP)* and
1040 *Tg(mitfa:GFP); mitfa*$^{w2/w2}$ (*nacre*) zebrafish embryos at 28 hours post fertilization (hpf).
1041 Annotated cell clusters as labelled. (**G'**) Comparison of relative cluster size for the two
1042 genotypes; *Tg(mitfa:GFP)* and *Tg(mitfa:GFP); mitfa*$^{w2/w2}$ (*nacre*) in (G).
1043 (**H**) Dot plot illustrating differentiational expressed genes (log2FC > 0.5; q-value < 0.05) in
1044 melanophores and progenitor cells in *mitfa*$^{w2/w2}$ and sibling embryos at 28hpf. Dot size indicates
1045 the percentage of cells expressing each gene; color intensity (grey to red) reflects normalized
1046 average expression levels (low to high).
1047 (**I**) Kaplan–Meier curves comparing tumor-free survival in wild-type and *casper* zebrafish
1048 following TEAZ-Eye injection using Strategy B plasmids for *mitfa* conditional knockout. Wild-type
1049 zebrafish were injected with either Strategy B plasmids plus non-targeting gRNAs (n=9) or
1050 Strategy B plasmids plus *mitfa*-targeting gRNAs (n=9). *Casper* zebrafish were injected with
1051 Strategy B plasmids and *mitfa*-targeting gRNAs (n=9).

1052 (**J**) Representative brightfield and GFP-overlay images of tumors that formed in *casper* (9 of 9)
1053 and wild-type zebrafish injected with *mitfa*-targeting gRNAs (2 of 9). Metastatic cells are
1054 indicated by red arrows.
1055
1056 **Figure 5: Oncogenic GNAQ and BRAF transform transcriptionally distinct cells within the**
1057 **melanocyte lineage.**
1058 (**A**) UMAP obtained after clustering tumor cells from *Tg(mitfa:BRAF^{V600E}): tp53$^{-/-}$* : *mitfa$^{w2/w2}$*
1059 zebrafish where TEAZ-Skin was used to rescue *mitfa* expression and knockout *ptena* and *ptenb*
1060 to induce cutaneous melanoma[32], along with our GNAQ-induced tumors by TEAZ-Skin (Strategy
1061 B: *mitfa:Cas9, U6:*gRNA-*tp53, U6:*gRNA-*ptena, U6:*gRNA-*ptenb, mitfa:GNAQ^{Q209L}-mitfa:GFP*).
1062 BRAF-induced tumors in red and GNAQ-induced tumors in blue.
1063 (**B**) Violin plot showing differentially expressed genes (log2FC > 0.5, q-value < 0.05) between
1064 BRAF-induced and GNAQ-induced tumors from (A). The plot displays the distribution of gene
1065 expression across individual cells, with the width indicating cell density at specific expression
1066 levels and the height representing the range of expression values.
1067 (**C**) Integrated UMAP after clustering GFP-positive cells sorted from *Tg(mitfa:GFP)* and
1068 *Tg(mitfa:GFP); mitfa$^{w2/w2}$* (*nacre*) zebrafish embryos at 28 hours post fertilization (hpf).
1069 Annotated cell clusters as labelled.
1070 (**D**) Average enrichment of signature genes from BRAF- and GNAQ-driven tumors projected
1071 onto the UMAP in (C) using UCell with 'FeaturePlot' function. Signature genes represent the top
1072 50 enriched genes from each tumor genotype that are also expressed in the embryonic
1073 melanocyte lineage.
1074 (**E**) UMAP of primary melanocytes and melanocyte progenitors from 9 control wild-type eyes, 2
1075 control wild-type skin sections, and 3 control *casper* eyes. Cells are labeled according to their
1076 genotype (*casper* and wild-type) and tissue origin (eye and skin).

1077 (**F**) Feature plots representing the relative mRNA expression of *pax3a*, *foxd3*, *sox10*, and *tfec* in
1078 melanocytes described in (E). Color intensity (grey to red) reflects normalized average
1079 expression levels (low to high). The red dotted line indicates cells that are clustering closely with
1080 the melanocyte progenitors identified in *casper* eyes.
1081
1082
1083 **Figure S1:** Mitfa-deficient zebrafish have decreased tumor latency compared to wild-types by
1084 TEAZ-Skin. (**A**) Kaplan-Meier curves estimating tumor-free survival, defined as the time from
1085 electroporation until the first visible appearance of GFP+ nodular tumors, in adult wild-type
1086 zebrafish via TEAZ-Skin. Injections contained *mitfa*:Cas9 with *U6*:gRNA-*ptena* + *U6*:gRNA-
1087 *ptenb* (*ptena/b* CRISPR), *mitfa*:Cas9 with *U6*:gRNA-*tp53* (*tp53* CRISPR), *mitfa*:*GNAQ*^{Q209L}-
1088 *mitfa*:GFP (GNAQ: GFP), strategy A plasmids, or strategy B plasmids (n=3 per condition). (**B**)
1089 Kaplan-Meier curves estimating tumor-free survival in adult *nacre* (*mitfa*$^{w2/w2}$) zebrafish via
1090 TEAZ-Skin. Same injection mixes as in (A). (n=5 for Strategy B, n=3 for rest) (**B'**)
1091 Representative brightfield and fluorescent images shown at 2, 4, and 6 weeks for strategy B
1092 injection in *nacre*. (**C**) Kaplan-Meier curves estimating tumor-free survival in adult *casper*
1093 (*mitfa*$^{w2/w2}$, *mpv17*$^{a9/a9}$) zebrafish via TEAZ-Skin. Same injection mixes as in (A). (n=5 for
1094 Strategies A and B, n=3 for rest) (**D**) Kaplan-Meier curves estimating tumor-free survival in adult
1095 wild-type, *nacre*, and *casper* zebrafish via TEAZ-Skin. Oncogene alone (GNAQ: GFP) is
1096 compared to strategy B plasmids for each genotype. (n=5 for strategy B in *nacre* and *casper*,
1097 n=3 for rest). (**E**) Representative images of Strategy B TEAZ-Skin in wild-type and *casper* and a
1098 xanthoma that formed in a *Tg(mitfa:BRAF*^{V600E}*); mitfa*$^{w2/w2}$*; tp53*$^{-/-}$ zebrafish. Note the bright
1099 orange color of the xanthoma, indicated by the black arrow.
1100
1101 **Figure S2:** Targeted Sanger sequencing to confirm CRISPR gene editing following TEAZ-Skin
1102 injection using Strategy B plasmids. 11 tumors and 2 wild-type tissue controls were used for

1103 INDEL analysis to verify gene editing in *tp53, ptena,* and *ptenb.* Green box indicates successful
1104 gene editing; red box indicates no gene editing. Total number of edited genes per sample are
1105 indicated in the right-most column.
1106
1107 **Figure S3:** Immunofluorescence of the choroid using an anti-GFP antibody in (**A**) *Tg*(*mitfa*:GFP)
1108 with 10x magnification and in (**B**) *Tg*(*mitfa*:GFP) following quenching of autofluorescence. (**C**)
1109 TEAZ-Eye–injected zebrafish expressing an eGFP construct driven by the *mitfa* promoter
1110 (*mitfa:GFP*) with 40x magnification. Sections were counterstained with DAPI to visualize nuclei.
1111
1112 **Figure S4:** UMAP of normal eyes and TEAZ-Eye uveal melanoma in wild-type zebrafish
1113 (Strategy B). (**A**) Integrated object is split by sequencing replicates (top) and feature plots
1114 showing *mlana* RNA expression to identify normal choroidal melanocytes and uveal melanoma
1115 cells (bottom). Color intensity (grey to red) reflects normalized average expression levels (low to
1116 high). The red dotted line indicates the melanocyte and uveal melanoma clusters.
1117
1118 **Figure S5:** Gross images of tissue and tumors used for single cell RNA-Seq in wild-type
1119 zebrafish.
1120
1121 **Figure S6:** Ingenuity Pathway Analysis of genes enriched in TEAZ-Eye compared to the tumor
1122 microenvironment. (**A**) The top 49 pathways enriched in TEAZ-Eye. (**B**) Select pathways
1123 enriched in TEAZ-Eye pertaining to fatty acid oxidation and signaling. Color intensity indicates
1124 the sign and magnitude of the z-score from blue (negative) to orange (positive). Significance is
1125 indicated by the -log(p-value).
1126
1127 **Figure S7:** Overall survival of patients with uveal melanoma (UM) and cutaneous melanoma
1128 (CM) based on expression levels of *FABP3*, *KIT, FABP5, LGALS2,* and *GCH*. Disease-free

1129 survival in UM and CM patients based on *FABP3, KIT, and FABP5* expression. Dotted lines
1130 represent 95% confidence intervals. Data derived from TCGA datasets.
1131
1132 **Figure S8:** Normalized RNA expression of *FABP5, FABP3, LGALS1, GCH, LGALS2, KIT*
1133 across the 4 TCGA molecular subclasses. [55] Groups were compared by ANOVA with post-hoc
1134 Tukey test. ns = not significant, * p-value<0.05; ** p-value<0.01; ***p-value<0.001; ****p-
1135 value<0.0001.
1136
1137 **Figure S9:** Mock injected wild-type zebrafish eyes do not show an increase in activated
1138 fibroblast markers as compared to uninjected controls. (**A**) UMAP representation of wild-type
1139 normal eyes from three different sources: mock injected, sibling-matched (3 pooled eyes),
1140 uninjected tumor-paired (2 pooled eyes), and uninjected sibling-matched (4 pooled eyes). The
1141 red dotted line indicates the fibroblast clusters. (**B**) Feature plots showing *fn1a* RNA expression
1142 across wild-type eye control groups. Color intensity (grey to red) reflects normalized average
1143 expression levels (low to high). (**C**) Dot plot of fibroblast activation marker genes in the fibroblast
1144 clusters of wild-type eye control groups. Dot size indicates the percentage of cells expressing
1145 each gene; color intensity (grey to blue) reflects normalized average expression levels (low to
1146 high).
1147
1148 **Figure S10:** Ingenuity Pathway Analysis of enriched genes in TEAZ-Eye and TEAZ-Skin
1149 compared to the combined tumor microenvironment (eye and skin). (**A**) Enriched pathways from
1150 genes that were common to only TEAZ-Eye and TEAZ-Skin compared to the combined tumor
1151 microenvironment. Families of pathways have been identified with a colored box and colored
1152 label including: cancer proliferation (green), WNT signaling (blue), metabolism (red), PTEN
1153 regulation (black), and RAF/MAPK signaling (black). (**B**) Enriched pathways from genes that
1154 were common to all four gene subsets (TEAZ-Eye, TEAZ-Skin, choroidal melanocytes, skin

1155 melanocytes) versus their respective combined microenvironments (normal or tumor). Families
1156 of pathways have been identified with a colored box and colored label including: melanocyte
1157 identity (black), signals downstream of GNAQ/GNA11 (blue), and survival/proliferation (green).
1158 Color intensity indicates the sign and magnitude of the z-score from blue (negative) to orange
1159 (positive). Significance is indicated by the -log(p-value).
1160
1161 **Figure S11:** Melanocyte rescue experiments in *nacre* zebrafish by TEAZ-Eye using plasmids
1162 containing *mitfa*:*mitfa*; *mitfa*:GFP (miniCoopR[29]). (**A-A'**) H&E images (10x and 40x
1163 magnification) of wild-type (*AB*) eyes following TEAZ-Eye injection with (**A**) control *mitfa*-GFP or
1164 (**A'**) miniCoopR plasmids. (**B-B'**) H&E images (10x and 40x magnification) of *mitfa*$^{w2/w2}$ (*nacre*)
1165 eyes following TEAZ-Eye injection with (**B**) control *mitfa*-GFP or (**B'**) miniCoopR plasmids,
1166 rescued melanocytes in the choroid are indicated by a red asterisk. (**C**) Representative dorsal
1167 image of a transgenic *Tg(mitfa:GFP); mitfa*$^{w2/w2}$ injected with *mitfa*:*GNAQ*^{Q209L} following TEAZ-
1168 Eye injection.
1169
1170 **Figure S12:** Gross images of tissue and tumors used for single cell RNA-Seq in *casper*
1171 zebrafish and transgenic *Tg*(*mitfa*:GFP); *mitfa*$^{+/w2}$ and *Tg*(*mitfa*:GFP); *mitfa*$^{w2/w2}$ whole embryos.
1172
1173 **Figure S13:** UMAP representation of UM tumors derived from *casper* zebrafish, with
1174 accompanying pseudotime analysis. (**A**) UMAP representation following scRNA-seq on normal
1175 *casper* control eyes (3 pooled eyes) and UM tumors (3 pooled tumors) derived in *casper* (TEAZ-
1176 Eye) (**B**) Feature plot showing *eGFP* expression and *mitfa*$^{w2/w2}$ expression (**C**) UMAP following
1177 re-clustering of *mitfa*$^{w2/w2}$ positive cells from (B), with overlayed unsupervised pseudotime
1178 analysis using Monocle analysis.
1179

1180 **Figure S14:** Immunofluorescent staining for Pax3 in the mouse limbus. (**A**) Representative 20x
1181 image of the mouse eye showing Pax3 positive staining in the limbus region. Sections were
1182 counterstained with DAPI to visualize nuclei. (**B**) Post-image processing showing the retina
1183 (red), cornea (orange) and limbus (purple), Pax3-positive cells in green.
1184
1185 **Figure S15:** Representative images of TEAZ-Skin induced tumors (*Strategy B*) in (**A**) wild-type
1186 at 16 weeks, (**B**) conditional *mitfa*-KO (wild-type) at 8 weeks and (**C**) *casper* zebrafish at 8
1187 weeks post TEAZ-Skin. Brightfield and GFP-overlaid images are shown to highlight primary and
1188 metastatic cells in (B-C), and the absence of metastasis in (A).
1189
1190 **Figure S16:** Violin plots representing *mitfa* expression as well as pigmentation genes in
1191 $BRAF^{V600E}$- and $GNAQ^{Q209L}$-positive tumors by single cell RNA-Seq analysis.
1192
1193 **Figure S17:** Dot plot of genes enriched in chromatoblasts and in uveal melanoma tumors
1194 derived in wild-type zebrafish following TEAZ-Eye compared to the tumor microenvironment
1195 (TME). Genes enriched in a particular pigment cell type are labelled, including: iridophore,
1196 xanthophore, and melanocyte.
1197
1198 **Figure S18:** UMAP representation of melanocytes and melanocyte progenitors in *casper*
1199 normal eyes and in the three sequencing replicates of wild-type normal eyes. The red dotted
1200 line indicates melanocyte progenitors in the *casper* sample and melanocytes that are clustering
1201 closely with such progenitors in wild-type samples.
1202
1203
1204

1205 **Supplemental Table 1** – Findallmarkers of the integrated object between wild-type control eyes
1206 and wild-type TEAZ-Eye.
1207 **Supplemental Table 2** – RNA expression data of *FABP3*, *FABP5*, *LGALS2*, *LGALS1*, *BSCL2*,
1208 *GCH1*, and *KIT* across the 4 TCGA molecular subclasses in uveal melanoma with
1209 corresponding sample IDs.
1210 **Supplemental Table 3** – Differentially expressed genes between cancer associated fibroblasts
1211 from wild-type TEAZ-Eye and normal fibroblasts from wild-type normal eyes.
1212 **Supplemental Table 4** – Findmarkers for choroidal melanocytes, skin melanocytes, TEAZ-Eye,
1213 and TEAZ-Skin versus their respective microenvironments. Table also includes gene names in
1214 every intersection of the Venn Diagram comparison of all four groups.
1215 **Supplemental Table 5** – Differentially expressed genes between eye and skin melanocytes and
1216 between TEAZ-Eye and TEAZ-Skin, respectively.
1217 **Supplemental Table 6** – Findallmarkers of the *casper* TEAZ-Eye single-cell object.
1218 **Supplemental Table 7** – Findallmarkers of the *casper* normal eye single-cell object.
1219 **Supplemental Table 8** – Findallmarkers of the integrated object between *casper* TEAZ-Eye and
1220 *casper* normal eye with cluster names labelled.
1221 **Supplemental Table 9** – Findallmarkers of the subset of GFP-positive clusters from the
1222 integrated object between *casper* TEAZ-Eye and *casper* normal eye.
1223 **Supplemental Table 10** – Findallmarkers of the integrated object of neural crest and neural
1224 crest-derived cells from *Tg*(*mitfa*:GFP) *mitfa*$^{+/w2}$ and *Tg*(mitfa:GFP) *mitfa*$^{w2/w2}$ embryos.
1225 **Supplemental Table 11** – Differentially expressed genes between neural crest and neural crest-
1226 derived clusters from *Tg*(*mitfa*:GFP) *mitfa*$^{+/w2}$ and *Tg*(mitfa:GFP) *mitfa*$^{w2/w2}$ embryos.
1227 **Supplemental Table 12** – Injection and tumor penetrance of wild-type and *casper* zebrafish
1228 injected with Strategy B plasmids and either *U6*:gRNA-nontargeting or *U6*:gRNA-*mitfa*.
1229 **Supplemental Table 13** – Differentially expressed genes between *BRAF*^{V600E}-driven tumors and
1230 *GNAQ*^{Q209L}-driven tumors in adult zebrafish.

1. Gentien, D., Saberi-Ansari, E., Servant, N., Jolly, A., de la Grange, P., Némati, F., Liot, G., Saule, S., Teissandier, A., Bourc'his, D., et al. (2023). Multi-omics comparison of malignant and normal uveal melanocytes reveals molecular features of uveal melanoma. Cell Rep *42*, 113132. 10.1016/j.celrep.2023.113132.
2. Rodrigues, M., Mobuchon, L., Houy, A., Alsafadi, S., Baulande, S., Mariani, O., Marande, B., Ait Rais, K., Van der Kooij, M.K., Kapiteijn, E., et al. (2019). Evolutionary Routes in Metastatic Uveal Melanomas Depend on MBD4 Alterations. Clin Cancer Res *25*, 5513-5524. 10.1158/1078-0432.Ccr-19-1215.
3. Kolandjian, N.A., Wei, C., Patel, S.P., Richard, J.L., Dett, T., Papadopoulos, N.E., and Bedikian, A.Y. (2013). Delayed systemic recurrence of uveal melanoma. Am J Clin Oncol *36*, 443-449. 10.1097/COC.0b013e3182546a6b.
4. Jager, M.J., Shields, C.L., Cebulla, C.M., Abdel-Rahman, M.H., Grossniklaus, H.E., Stern, M.H., Carvajal, R.D., Belfort, R.N., Jia, R., Shields, J.A., and Damato, B.E. (2020). Uveal melanoma. Nat Rev Dis Primers *6*, 24. 10.1038/s41572-020-0158-0.
5. Lamas, N.J., Martel, A., Nahon-Estève, S., Goffinet, S., Macocco, A., Bertolotto, C., Lassalle, S., and Hofman, P. (2021). Prognostic Biomarkers in Uveal Melanoma: The Status Quo, Recent Advances and Future Directions. Cancers (Basel) *14*. 10.3390/cancers14010096.
6. Kaliki, S., and Shields, C.L. (2017). Uveal melanoma: relatively rare but deadly cancer. Eye (Lond) *31*, 241-257. 10.1038/eye.2016.275.
7. Yu, F.X., Luo, J., Mo, J.S., Liu, G., Kim, Y.C., Meng, Z., Zhao, L., Peyman, G., Ouyang, H., Jiang, W., et al. (2014). Mutant Gq/11 promote uveal melanoma tumorigenesis by activating YAP. Cancer Cell *25*, 822-830. 10.1016/j.ccr.2014.04.017.
8. Singh, A.D., Bergman, L., and Seregard, S. (2005). Uveal melanoma: epidemiologic aspects. Ophthalmol Clin North Am *18*, 75-84, viii. 10.1016/j.ohc.2004.07.002.
9. Arnesen, K. (1985). The neural crest origin of uveal melanomas. Int Ophthalmol *7*, 143-147. 10.1007/bf00128360.
10. Van Raamsdonk, C.D., Bezrookove, V., Green, G., Bauer, J., Gaugler, L., O'Brien, J.M., Simpson, E.M., Barsh, G.S., and Bastian, B.C. (2009). Frequent somatic mutations of GNAQ in uveal melanoma and blue naevi. Nature *457*, 599-602. 10.1038/nature07586.
11. Shain, A.H., Bagger, M.M., Yu, R., Chang, D., Liu, S., Vemula, S., Weier, J.F., Wadt, K., Heegaard, S., Bastian, B.C., and Kiilgaard, J.F. (2019). The genetic evolution of metastatic uveal melanoma. Nat Genet *51*, 1123-1130. 10.1038/s41588-019-0440-9.
12. Silva-Rodríguez, P., Fernández-Díaz, D., Bande, M., Pardo, M., Loidi, L., and Blanco-Teijeiro, M.J. (2022). GNAQ and GNA11 Genes: A Comprehensive Review on Oncogenesis, Prognosis and Therapeutic Opportunities in Uveal Melanoma. Cancers (Basel) *14*. 10.3390/cancers14133066.
13. Li, Y., Shi, J., Yang, J., Ge, S., Zhang, J., Jia, R., and Fan, X. (2020). Uveal melanoma: progress in molecular biology and therapeutics. Ther Adv Med Oncol *12*, 1758835920965852. 10.1177/1758835920965852.
14. Gragoudas, E.S., Egan, K.M., Seddon, J.M., Glynn, R.J., Walsh, S.M., Finn, S.M., Munzenrider, J.E., and Spar, M.D. (1991). Survival of patients with metastases from uveal melanoma. Ophthalmology *98*, 383-389; discussion 390. 10.1016/s0161-6420(91)32285-1.

15. Rantala, E.S., Hernberg, M., and Kivelä, T.T. (2019). Overall survival after treatment for metastatic uveal melanoma: a systematic review and meta-analysis. Melanoma Res *29*, 561-568. 10.1097/cmr.0000000000000575.
16. Lane, A.M., Kim, I.K., and Gragoudas, E.S. (2018). Survival Rates in Patients After Treatment for Metastasis From Uveal Melanoma. JAMA Ophthalmol *136*, 981-986. 10.1001/jamaophthalmol.2018.2466.
17. Nathan, P., Hassel, J.C., Rutkowski, P., Baurain, J.F., Butler, M.O., Schlaak, M., Sullivan, R.J., Ochsenreither, S., Dummer, R., Kirkwood, J.M., et al. (2021). Overall Survival Benefit with Tebentafusp in Metastatic Uveal Melanoma. N Engl J Med *385*, 1196-1206. 10.1056/NEJMoa2103485.
18. Hassel, J.C., Piperno-Neumann, S., Rutkowski, P., Baurain, J.F., Schlaak, M., Butler, M.O., Sullivan, R.J., Dummer, R., Kirkwood, J.M., Orloff, M., et al. (2023). Three-Year Overall Survival with Tebentafusp in Metastatic Uveal Melanoma. N Engl J Med *389*, 2256-2266. 10.1056/NEJMoa2304753.
19. Wespiser, M., Neidhardt, E., and Negrier, S. (2023). Uveal melanoma: In the era of new treatments. Cancer Treat Rev *119*, 102599. 10.1016/j.ctrv.2023.102599.
20. Kaštelan, S., Antunica, A.G., Oresković, L.B., Pelčić, G., Kasun, E., and Hat, K. (2020). Immunotherapy for Uveal Melanoma - Current Knowledge and Perspectives. Curr Med Chem *27*, 1350-1366. 10.2174/0929867326666190704141444.
21. Wdowiak, K., Dolar-Szczasny, J., Rejdak, R., Drab, A., and Maciocha, A. (2025). A Brief Overview of Uveal Melanoma Treatment Methods with a Focus on the Latest Advances. J Clin Med *14*. 10.3390/jcm14124058.
22. Souto, E.B., Zielinska, A., Luis, M., Carbone, C., Martins-Gomes, C., Souto, S.B., and Silva, A.M. (2019). Uveal melanoma: physiopathology and new in situ-specific therapies. Cancer Chemother Pharmacol *84*, 15-32. 10.1007/s00280-019-03860-z.
23. Ma, J., Weng, L., Bastian, B.C., and Chen, X. (2021). Functional characterization of uveal melanoma oncogenes. Oncogene *40*, 806-820. 10.1038/s41388-020-01569-5.
24. Livingstone, E., Zaremba, A., Horn, S., Ugurel, S., Casalini, B., Schlaak, M., Hassel, J.C., Herbst, R., Utikal, J.S., Weide, B., et al. (2020). GNAQ and GNA11 mutant nonuveal melanoma: a subtype distinct from both cutaneous and uveal melanoma. Br J Dermatol *183*, 928-939. 10.1111/bjd.18947.
25. Lee, J.H., Choi, J.W., and Kim, Y.S. (2011). Frequencies of BRAF and NRAS mutations are different in histological types and sites of origin of cutaneous melanoma: a meta-analysis. Br J Dermatol *164*, 776-784. 10.1111/j.1365-2133.2010.10185.x.
26. Urtatiz, O., Haage, A., Tanentzapf, G., and Van Raamsdonk, C.D. (2021). Crosstalk with keratinocytes causes GNAQ oncogene specificity in melanoma. Elife *10*. 10.7554/eLife.71825.
27. Callahan, S.J., Tepan, S., Zhang, Y.M., Lindsay, H., Burger, A., Campbell, N.R., Kim, I.S., Hollmann, T.J., Studer, L., Mosimann, C., and White, R.M. (2018). Cancer modeling by Transgene Electroporation in Adult Zebrafish (TEAZ). Dis Model Mech *11*. 10.1242/dmm.034561.
28. Brombin, A., Simpson, D.J., Travnickova, J., Brunsdon, H., Zeng, Z., Lu, Y., Young, A.I.J., Chandra, T., and Patton, E.E. (2022). Tfap2b specifies an embryonic melanocyte stem cell

that retains adult multifate potential. Cell Rep *38*, 110234. 10.1016/j.celrep.2021.110234.

29. Ceol, C.J., Houvras, Y., Jane-Valbuena, J., Bilodeau, S., Orlando, D.A., Battisti, V., Fritsch, L., Lin, W.M., Hollmann, T.J., Ferré, F., et al. (2011). The histone methyltransferase SETDB1 is recurrently amplified in melanoma and accelerates its onset. Nature *471*, 513-517. 10.1038/nature09806.

30. Kenny, C., Dilshat, R., Seberg, H.E., Van Otterloo, E., Bonde, G., Helverson, A., Franke, C.M., Steingrímsson, E., and Cornell, R.A. (2022). TFAP2 paralogs facilitate chromatin access for MITF at pigmentation and cell proliferation genes. PLoS Genet *18*, e1010207. 10.1371/journal.pgen.1010207.

31. Lister, J.A., Lane, B.M., Nguyen, A., and Lunney, K. (2011). Embryonic expression of zebrafish MiT family genes tfe3b, tfeb, and tfec. Dev Dyn *240*, 2529-2538. 10.1002/dvdy.22743.

32. Lumaquin-Yin, D., Montal, E., Johns, E., Baggiolini, A., Huang, T.H., Ma, Y., LaPlante, C., Suresh, S., Studer, L., and White, R.M. (2023). Lipid droplets are a metabolic vulnerability in melanoma. Nat Commun *14*, 3192. 10.1038/s41467-023-38831-9.

33. Petratou, K., Spencer, S.A., Kelsh, R.N., and Lister, J.A. (2021). The MITF paralog tfec is required in neural crest development for fate specification of the iridophore lineage from a multipotent pigment cell progenitor. PLoS One *16*, e0244794. 10.1371/journal.pone.0244794.

34. Phelps, G.B., Hagen, H.R., Amsterdam, A., and Lees, J.A. (2022). MITF deficiency accelerates GNAQ-driven uveal melanoma. Proc Natl Acad Sci U S A *119*, e2107006119. 10.1073/pnas.2107006119.

35. Seberg, H.E., Van Otterloo, E., Loftus, S.K., Liu, H., Bonde, G., Sompallae, R., Gildea, D.E., Santana, J.F., Manak, J.R., Pavan, W.J., et al. (2017). TFAP2 paralogs regulate melanocyte differentiation in parallel with MITF. PLoS Genet *13*, e1006636. 10.1371/journal.pgen.1006636.

36. Kelsh, R.N., Brand, M., Jiang, Y.J., Heisenberg, C.P., Lin, S., Haffter, P., Odenthal, J., Mullins, M.C., van Eeden, F.J., Furutani-Seiki, M., et al. (1996). Zebrafish pigmentation mutations and the processes of neural crest development. Development *123*, 369-389. 10.1242/dev.123.1.369.

37. Dutton, K.A., Pauliny, A., Lopes, S.S., Elworthy, S., Carney, T.J., Rauch, J., Geisler, R., Haffter, P., and Kelsh, R.N. (2001). Zebrafish colourless encodes sox10 and specifies non-ectomesenchymal neural crest fates. Development *128*, 4113-4125. 10.1242/dev.128.21.4113.

38. McGowan, K.A., and Barsh, G.S. (2016). Evolution: How the zebrafish got its stripes. Elife *5*. 10.7554/eLife.14239.

39. Parichy, D.M., and Spiewak, J.E. (2015). Origins of adult pigmentation: diversity in pigment stem cell lineages and implications for pattern evolution. Pigment Cell Melanoma Res *28*, 31-50. 10.1111/pcmr.12332.

40. Phelps, G.B., Amsterdam, A., Hagen, H.R., García, N.Z., and Lees, J.A. (2022). MITF deficiency and oncogenic GNAQ each promote proliferation programs in zebrafish melanocyte lineage cells. Pigment Cell Melanoma Res *35*, 539-547. 10.1111/pcmr.13057.

41. Wessely, A., Steeb, T., Berking, C., and Heppt, M.V. (2021). How Neural Crest Transcription Factors Contribute to Melanoma Heterogeneity, Cellular Plasticity, and Treatment Resistance. Int J Mol Sci *22*. 10.3390/ijms22115761.
42. Kaufman, C.K., Mosimann, C., Fan, Z.P., Yang, S., Thomas, A.J., Ablain, J., Tan, J.L., Fogley, R.D., van Rooijen, E., Hagedorn, E.J., et al. (2016). A zebrafish melanoma model reveals emergence of neural crest identity during melanoma initiation. Science *351*, aad2197. 10.1126/science.aad2197.
43. Lister, J.A., Robertson, C.P., Lepage, T., Johnson, S.L., and Raible, D.W. (1999). nacre encodes a zebrafish microphthalmia-related protein that regulates neural-crest-derived pigment cell fate. Development *126*, 3757-3767. 10.1242/dev.126.17.3757.
44. Lister, J.A., Capper, A., Zeng, Z., Mathers, M.E., Richardson, J., Paranthaman, K., Jackson, I.J., and Elizabeth Patton, E. (2014). A conditional zebrafish MITF mutation reveals MITF levels are critical for melanoma promotion vs. regression in vivo. J Invest Dermatol *134*, 133-140. 10.1038/jid.2013.293.
45. Travnickova, J., Wojciechowska, S., Khamseh, A., Gautier, P., Brown, D.V., Lefevre, T., Brombin, A., Ewing, A., Capper, A., Spitzer, M., et al. (2019). Zebrafish MITF-Low Melanoma Subtype Models Reveal Transcriptional Subclusters and MITF-Independent Residual Disease. Cancer Res *79*, 5769-5784. 10.1158/0008-5472.Can-19-0037.
46. D'Agati, G., Beltre, R., Sessa, A., Burger, A., Zhou, Y., Mosimann, C., and White, R.M. (2017). A defect in the mitochondrial protein Mpv17 underlies the transparent casper zebrafish. Dev Biol *430*, 11-17. 10.1016/j.ydbio.2017.07.017.
47. White, R.M., Sessa, A., Burke, C., Bowman, T., LeBlanc, J., Ceol, C., Bourque, C., Dovey, M., Goessling, W., Burns, C.E., and Zon, L.I. (2008). Transparent adult zebrafish as a tool for in vivo transplantation analysis. Cell Stem Cell *2*, 183-189. 10.1016/j.stem.2007.11.002.
48. McMenamin, P.G., Shields, G.T., Seyed-Razavi, Y., Kalirai, H., Insall, R.H., Machesky, L.M., and Coupland, S.E. (2020). Melanoblasts Populate the Mouse Choroid Earlier in Development Than Previously Described. Invest Ophthalmol Vis Sci *61*, 33. 10.1167/iovs.61.10.33.
49. Voigt, A.P., Whitmore, S.S., Lessing, N.D., DeLuca, A.P., Tucker, B.A., Stone, E.M., Mullins, R.F., and Scheetz, T.E. (2020). Spectacle: An interactive resource for ocular single-cell RNA sequencing data analysis. Exp Eye Res *200*, 108204. 10.1016/j.exer.2020.108204.
50. Voigt, A.P., Mulfaul, K., Mullin, N.K., Flamme-Wiese, M.J., Giacalone, J.C., Stone, E.M., Tucker, B.A., Scheetz, T.E., and Mullins, R.F. (2019). Single-cell transcriptomics of the human retinal pigment epithelium and choroid in health and macular degeneration. Proc Natl Acad Sci U S A *116*, 24100-24107. 10.1073/pnas.1914143116.
51. Howe, D.G., Bradford, Y.M., Conlin, T., Eagle, A.E., Fashena, D., Frazer, K., Knight, J., Mani, P., Martin, R., Moxon, S.A., et al. (2013). ZFIN, the Zebrafish Model Organism Database: increased support for mutants and transgenics. Nucleic Acids Res *41*, D854-860. 10.1093/nar/gks938.
52. Sur, A., Wang, Y., Capar, P., Margolin, G., Prochaska, M.K., and Farrell, J.A. (2023). Single-cell analysis of shared signatures and transcriptional diversity during zebrafish development. Dev Cell *58*, 3028-3047.e3012. 10.1016/j.devcel.2023.11.001.

1404 53. Tatarakis, D., Cang, Z., Wu, X., Sharma, P.P., Karikomi, M., MacLean, A.L., Nie, Q., and
1405 Schilling, T.F. (2021). Single-cell transcriptomic analysis of zebrafish cranial neural crest
1406 reveals spatiotemporal regulation of lineage decisions during development. Cell Rep *37*,
1407 110140. 10.1016/j.celrep.2021.110140.
1408 54. Simões-Costa, M., and Bronner, M.E. (2015). Establishing neural crest identity: a gene
1409 regulatory recipe. Development *142*, 242-257. 10.1242/dev.105445.
1410 55. Robertson, A.G., Shih, J., Yau, C., Gibb, E.A., Oba, J., Mungall, K.L., Hess, J.M.,
1411 Uzunangelov, V., Walter, V., Danilova, L., et al. (2017). Integrative Analysis Identifies Four
1412 Molecular and Clinical Subsets in Uveal Melanoma. Cancer Cell *32*, 204-220.e215.
1413 10.1016/j.ccell.2017.07.003.
1414 56. Hunter, M.V., Joshi, E., Bowker, S., Montal, E., Ma, Y., Kim, Y.H., Yang, Z., Tuffery, L., Li, Z.,
1415 Rosiek, E., et al. (2025). Mechanical confinement governs phenotypic plasticity in
1416 melanoma. Nature. 10.1038/s41586-025-09445-6.
1417 57. Hunter, M.V., Moncada, R., Weiss, J.M., Yanai, I., and White, R.M. (2021). Spatially
1418 resolved transcriptomics reveals the architecture of the tumor-microenvironment
1419 interface. Nat Commun *12*, 6278. 10.1038/s41467-021-26614-z.
1420 58. Liu, T., Zhou, L., Xiao, Y., Andl, T., and Zhang, Y. (2022). BRAF Inhibitors Reprogram
1421 Cancer-Associated Fibroblasts to Drive Matrix Remodeling and Therapeutic Escape in
1422 Melanoma. Cancer Res *82*, 419-432. 10.1158/0008-5472.Can-21-0614.
1423 59. Mao, X., Xu, J., Wang, W., Liang, C., Hua, J., Liu, J., Zhang, B., Meng, Q., Yu, X., and Shi, S.
1424 (2021). Crosstalk between cancer-associated fibroblasts and immune cells in the tumor
1425 microenvironment: new findings and future perspectives. Mol Cancer *20*, 131.
1426 10.1186/s12943-021-01428-1.
1427 60. Wang, J., Song, Y., Li, Z., Gao, T., Shen, W., Kang, Z., and Xu, C. (2025). Combining single-
1428 cell and bulk RNA sequencing to identify CAF-related signature for prognostic prediction
1429 and treatment response in patients with melanoma. Sci Rep *15*, 29082. 10.1038/s41598-
1430 025-14979-w.
1431 61. Kaochar, S., Dong, J., Torres, M., Rajapakshe, K., Nikolos, F., Davis, C.M., Ehli, E.A., Coarfa,
1432 C., Mitsiades, N., and Poulaki, V. (2018). ICG-001 Exerts Potent Anticancer Activity
1433 Against Uveal Melanoma Cells. Invest Ophthalmol Vis Sci *59*, 132-143. 10.1167/iovs.17-
1434 22454.
1435 62. Zheng, L., Liu, Y., and Pan, J. (2017). Inhibitory effect of pyrvinium pamoate on uveal
1436 melanoma cells involves blocking of Wnt/β-catenin pathway. Acta Biochim Biophys Sin
1437 (Shanghai) *49*, 890-898. 10.1093/abbs/gmx089.
1438 63. Wu, S., Han, M., and Zhang, C. (2022). Overexpression of microRNA-130a represses uveal
1439 melanoma cell migration and invasion through inactivation of the Wnt/β-catenin
1440 signaling pathway by downregulating USP6. Cancer Gene Ther *29*, 930-939.
1441 10.1038/s41417-021-00377-7.
1442 64. Zuidervaart, W., van Nieuwpoort, F., Stark, M., Dijkman, R., Packer, L., Borgstein, A.M.,
1443 Pavey, S., van der Velden, P., Out, C., Jager, M.J., et al. (2005). Activation of the MAPK
1444 pathway is a common event in uveal melanomas although it rarely occurs through
1445 mutation of BRAF or RAS. Br J Cancer *92*, 2032-2038. 10.1038/sj.bjc.6602598.

1446 65. Chen, X., Wu, Q., Depeille, P., Chen, P., Thornton, S., Kalirai, H., Coupland, S.E., Roose,
1447 J.P., and Bastian, B.C. (2017). RasGRP3 Mediates MAPK Pathway Activation in GNAQ
1448 Mutant Uveal Melanoma. Cancer Cell *31*, 685-696.e686. 10.1016/j.ccell.2017.04.002.
1449 66. Rimoldi, D., Salvi, S., Liénard, D., Lejeune, F.J., Speiser, D., Zografos, L., and Cerottini, J.C.
1450 (2003). Lack of BRAF mutations in uveal melanoma. Cancer Res *63*, 5712-5715.
1451 67. Abdel-Rahman, M.H., Yang, Y., Zhou, X.P., Craig, E.L., Davidorf, F.H., and Eng, C. (2006).
1452 High frequency of submicroscopic hemizygous deletion is a major mechanism of loss of
1453 expression of PTEN in uveal melanoma. J Clin Oncol *24*, 288-295.
1454 10.1200/jco.2005.02.2418.
1455 68. Pópulo, H., Soares, P., Rocha, A.S., Silva, P., and Lopes, J.M. (2010). Evaluation of the
1456 mTOR pathway in ocular (uvea and conjunctiva) melanoma. Melanoma Res *20*, 107-117.
1457 10.1097/CMR.0b013e32832ccd09.
1458 69. Woodman, S.E. (2012). Metastatic uveal melanoma: biology and emerging treatments.
1459 Cancer J *18*, 148-152. 10.1097/PPO.0b013e31824bd256.
1460 70. Ulrich, E., Kistenmacher, S., Martin, G., Schlötzer-Schrehardt, U., Seitz, B., Auw-Hädrich,
1461 C., Schlunck, G., Reinhard, T., and Polisetti, N. (2025). PAX3 expression patterns in ocular
1462 surface melanocytes. Sci Rep *15*, 12472. 10.1038/s41598-025-90318-3.
1463 71. Kumar, N., Singh, M.K., Singh, L., Jha, J., Pushker, N., Lomi, N., Meel, R., Sen, S., and
1464 Kashyap, S. (2025). Prognostic significance of pigmentation and stem cell markers in
1465 Indian population of uveal melanoma. Br J Ophthalmol *109*, 799-808. 10.1136/bjo-2024-
1466 325886.
1467 72. Kubic, J.D., Young, K.P., Plummer, R.S., Ludvik, A.E., and Lang, D. (2008). Pigmentation
1468 PAX-ways: the role of Pax3 in melanogenesis, melanocyte stem cell maintenance, and
1469 disease. Pigment Cell Melanoma Res *21*, 627-645. 10.1111/j.1755-148X.2008.00514.x.
1470 73. Lang, D., Lu, M.M., Huang, L., Engleka, K.A., Zhang, M., Chu, E.Y., Lipner, S., Skoultchi, A.,
1471 Millar, S.E., and Epstein, J.A. (2005). Pax3 functions at a nodal point in melanocyte stem
1472 cell differentiation. Nature *433*, 884-887. 10.1038/nature03292.
1473 74. Baggiolini, A., Callahan, S.J., Montal, E., Weiss, J.M., Trieu, T., Tagore, M.M., Tischfield,
1474 S.E., Walsh, R.M., Suresh, S., Fan, Y., et al. (2021). Developmental chromatin programs
1475 determine oncogenic competence in melanoma. Science *373*, eabc1048.
1476 10.1126/science.abc1048.
1477 75. Johns, E., Ma, Y., Louphrasitthiphol, P., Peralta, C., Hunter, M.V., Raymond, J.H., Molina,
1478 H., Goding, C.R., and White, R.M. (2025). The Lipid Droplet Protein DHRS3 Is a Regulator
1479 of Melanoma Cell State. Pigment Cell Melanoma Res *38*, e13208. 10.1111/pcmr.13208.
1480 76. Xu, Y., Xu, W.H., Yang, X.L., Zhang, H.L., and Zhang, X.F. (2020). Fatty acid-binding protein
1481 5 predicts poor prognosis in patients with uveal melanoma. Oncol Lett *19*, 1771-1780.
1482 10.3892/ol.2020.11301.
1483 77. Van Ly, D., Wang, D., Conway, R.M., Giblin, M., Liang, S., Lukeis, R., Lim, L.A., Hesson, L.,
1484 and Cherepanoff, S. (2020). Lipid-Producing Ciliochoroidal Melanoma with Expression of
1485 HMG-CoA Reductase. Ocul Oncol Pathol *6*, 416-421. 10.1159/000510393.
1486 78. Yavuzyigitoglu, S., Kilic, E., Vaarwater, J., de Klein, A., Paridaens, D., and Verdijk, R.M.
1487 (2016). Lipomatous Change in Uveal Melanoma: Histopathological,
1488 Immunohistochemical and Cytogenetic Analysis. Ocul Oncol Pathol *2*, 133-135.
1489 10.1159/000440981.

1490 79. Fiorentzis, M., Kalirai, H., Katopodis, P., and Coupland, S.E. (2017). Adipophilin
1491 expression in primary and metastatic uveal melanoma: a pilot study. Graefes Arch Clin
1492 Exp Ophthalmol *255*, 1049-1051. 10.1007/s00417-017-3630-0.
1493 80. Horvathova Kajabova, V., Soltysova, A., Demkova, L., Plesnikova, P., Lyskova, D., Furdova,
1494 A., Babal, P., and Smolkova, B. (2021). KIT Expression Is Regulated by DNA Methylation in
1495 Uveal Melanoma Tumors. Int J Mol Sci *22*. 10.3390/ijms221910748.
1496 81. Hu, S., Huang, J., Pei, S., Ouyang, Y., Ding, Y., Jiang, L., Lu, J., Kang, L., Huang, L., Xiang, H.,
1497 et al. (2019). Ganoderma lucidum polysaccharide inhibits UVB-induced melanogenesis
1498 by antagonizing cAMP/PKA and ROS/MAPK signaling pathways. J Cell Physiol *234*, 7330-
1499 7340. 10.1002/jcp.27492.
1500 82. Liang, R., Cheng, A., Lu, S., Zhang, X., Ren, M., Lin, J., Wu, Y., Zhang, W., and Luan, X.
1501 (2024). Seleno-amino Acid Metabolism Reshapes the Tumor Microenvironment: from
1502 Cytotoxicity to Immunotherapy. Int J Biol Sci *20*, 2779-2789. 10.7150/ijbs.95484.
1503 83. Li, W., and Cornell, R.A. (2007). Redundant activities of Tfap2a and Tfap2c are required
1504 for neural crest induction and development of other non-neural ectoderm derivatives in
1505 zebrafish embryos. Dev Biol *304*, 338-354. 10.1016/j.ydbio.2006.12.042.
1506 84. Lewis, J.L., Bonner, J., Modrell, M., Ragland, J.W., Moon, R.T., Dorsky, R.I., and Raible,
1507 D.W. (2004). Reiterated Wnt signaling during zebrafish neural crest development.
1508 Development *131*, 1299-1308. 10.1242/dev.01007.
1509 85. Monsoro-Burq, A.H., Wang, E., and Harland, R. (2005). Msx1 and Pax3 cooperate to
1510 mediate FGF8 and WNT signals during Xenopus neural crest induction. Dev Cell *8*, 167-
1511 178. 10.1016/j.devcel.2004.12.017.
1512 86. Han, A., Purwin, T.J., Bechtel, N., Liao, C., Chua, V., Seifert, E., Sato, T., Schug, Z.T.,
1513 Speicher, D.W., Harbour, J.W., and Aplin, A.E. (2021). BAP1 mutant uveal melanoma is
1514 stratified by metabolic phenotypes with distinct vulnerability to metabolic inhibitors.
1515 Oncogene *40*, 618-632. 10.1038/s41388-020-01554-y.
1516 87. Matatall, K.A., Agapova, O.A., Onken, M.D., Worley, L.A., Bowcock, A.M., and Harbour,
1517 J.W. (2013). BAP1 deficiency causes loss of melanocytic cell identity in uveal melanoma.
1518 BMC Cancer *13*, 371. 10.1186/1471-2407-13-371.
1519 88. Chang, J., Campbell-Hanson, K.R., Vanneste, M., Bartschat, N.I., Nagel, R., Arnadottir,
1520 A.K., Vu, H.N., Montgomery, C., Yevdash, J., Jiang, J., et al. (2025). Antagonistic roles for
1521 MITF and TFE3 in melanoma plasticity. Cell Rep *44*, 115474.
1522 10.1016/j.celrep.2025.115474.
1523 89. Pouw, A.E., Greiner, M.A., Coussa, R.G., Jiao, C., Han, I.C., Skeie, J.M., Fingert, J.H.,
1524 Mullins, R.F., and Sohn, E.H. (2021). Cell-Matrix Interactions in the Eye: From Cornea to
1525 Choroid. Cells *10*. 10.3390/cells10030687.
1526 90. Chirco, K.R., Worthington, K.S., Flamme-Wiese, M.J., Riker, M.J., Andrade, J.D.,
1527 Ueberheide, B.M., Stone, E.M., Tucker, B.A., and Mullins, R.F. (2017). Preparation and
1528 evaluation of human choroid extracellular matrix scaffolds for the study of cell
1529 replacement strategies. Acta Biomater *57*, 293-303. 10.1016/j.actbio.2017.05.011.
1530 91. Angi, M., Kalirai, H., Prendergast, S., Simpson, D., Hammond, D.E., Madigan, M.C.,
1531 Beynon, R.J., and Coupland, S.E. (2016). In-depth proteomic profiling of the uveal
1532 melanoma secretome. Oncotarget *7*, 49623-49635. 10.18632/oncotarget.10418.

1533 92. Aughton, K., Hattersley, J., Coupland, S.E., and Kalirai, H. (2024). Revealing the structural
1534 microenvironment of high metastatic risk uveal melanomas following decellularisation.
1535 Sci Rep *14*, 26811. 10.1038/s41598-024-78171-2.
1536 93. Luthold, C., Didion, M., Benedum, E., Burkhart, A.-K., Demmerle, N., Wirth, E.,
1537 Gunaratnam, G., Racz, V.S., Thangamurugan, S., Helms, V., et al. (2025). Melanocyte
1538 differentiation and mechanosensation are differentially modulated by distinct
1539 extracellular matrix proteins. bioRxiv, 2024.2010.2004.616635.
1540 10.1101/2024.10.04.616635.
1541 94. Hajkova, N., Hojny, J., Nemejcova, K., Dundr, P., Ulrych, J., Jirsova, K., Glezgova, J., and
1542 Ticha, I. (2018). Germline mutation in the TP53 gene in uveal melanoma. Sci Rep *8*, 7618.
1543 10.1038/s41598-018-26040-0.
1544 95. Harbour, J.W., Onken, M.D., Roberson, E.D., Duan, S., Cao, L., Worley, L.A., Council, M.L.,
1545 Matatall, K.A., Helms, C., and Bowcock, A.M. (2010). Frequent mutation of BAP1 in
1546 metastasizing uveal melanomas. Science *330*, 1410-1413. 10.1126/science.1194472.
1547 96. Brantley, M.A., Jr., and Harbour, J.W. (2000). Deregulation of the Rb and p53 pathways in
1548 uveal melanoma. Am J Pathol *157*, 1795-1801. 10.1016/s0002-9440(10)64817-1.
1549 97. Coupland, S.E., Anastassiou, G., Stang, A., Schilling, H., Anagnostopoulos, I., Bornfeld, N.,
1550 and Stein, H. (2000). The prognostic value of cyclin D1, p53, and MDM2 protein
1551 expression in uveal melanoma. J Pathol *191*, 120-126. 10.1002/(sici)1096-
1552 9896(200006)191:2<120::Aid-path591>3.0.Co;2-p.
1553 98. Paraoan, L., Gray, D., Hiscott, P., Ebrahimi, B., Damato, B., and Grierson, I. (2006).
1554 Expression of p53-induced apoptosis effector PERP in primary uveal melanomas:
1555 downregulation is associated with aggressive type. Exp Eye Res *83*, 911-919.
1556 10.1016/j.exer.2006.04.016.
1557 99. Davies, L., Spiller, D., White, M.R., Grierson, I., and Paraoan, L. (2011). PERP expression
1558 stabilizes active p53 via modulation of p53-MDM2 interaction in uveal melanoma cells.
1559 Cell Death Dis *2*, e136. 10.1038/cddis.2011.19.
1560 100. de Lange, J., Ly, L.V., Lodder, K., Verlaan-de Vries, M., Teunisse, A.F., Jager, M.J., and
1561 Jochemsen, A.G. (2012). Synergistic growth inhibition based on small-molecule p53
1562 activation as treatment for intraocular melanoma. Oncogene *31*, 1105-1116.
1563 10.1038/onc.2011.309.
1564 101. Butler, A., Hoffman, P., Smibert, P., Papalexi, E., and Satija, R. (2018). Integrating single-
1565 cell transcriptomic data across different conditions, technologies, and species. Nat
1566 Biotechnol *36*, 411-420. 10.1038/nbt.4096.
1567 102. Kolberg, L., Raudvere, U., Kuzmin, I., Adler, P., Vilo, J., and Peterson, H. (2023). g:Profiler-
1568 interoperable web service for functional enrichment analysis and gene identifier
1569 mapping (2023 update). Nucleic Acids Res *51*, W207-w212. 10.1093/nar/gkad347.
1570 103. Krämer, A., Green, J., Pollard, J., Jr., and Tugendreich, S. (2014). Causal analysis
1571 approaches in Ingenuity Pathway Analysis. Bioinformatics *30*, 523-530.
1572 10.1093/bioinformatics/btt703.
1573 104. Subramanian, A., Tamayo, P., Mootha, V.K., Mukherjee, S., Ebert, B.L., Gillette, M.A.,
1574 Paulovich, A., Pomeroy, S.L., Golub, T.R., Lander, E.S., and Mesirov, J.P. (2005). Gene set
1575 enrichment analysis: a knowledge-based approach for interpreting genome-wide

1576 expression profiles. Proc Natl Acad Sci U S A *102*, 15545-15550.
1577 10.1073/pnas.0506580102.
1578 105. Mootha, V.K., Lindgren, C.M., Eriksson, K.F., Subramanian, A., Sihag, S., Lehar, J.,
1579 Puigserver, P., Carlsson, E., Ridderstråle, M., Laurila, E., et al. (2003). PGC-1alpha-
1580 responsive genes involved in oxidative phosphorylation are coordinately downregulated
1581 in human diabetes. Nat Genet *34*, 267-273. 10.1038/ng1180.
1582 106. Trapnell, C., Cacchiarelli, D., Grimsby, J., Pokharel, P., Li, S., Morse, M., Lennon, N.J.,
1583 Livak, K.J., Mikkelsen, T.S., and Rinn, J.L. (2014). The dynamics and regulators of cell fate
1584 decisions are revealed by pseudotemporal ordering of single cells. Nat Biotechnol *32*,
1585 381-386. 10.1038/nbt.2859.
1586 107. Bloh, K., Kanchana, R., Bialk, P., Banas, K., Zhang, Z., Yoo, B.C., and Kmiec, E.B. (2021).
1587 Deconvolution of Complex DNA Repair (DECODR): Establishing a Novel Deconvolution
1588 Algorithm for Comprehensive Analysis of CRISPR-Edited Sanger Sequencing Data. Crispr j
1589 *4*, 120-131. 10.1089/crispr.2020.0022.
1590

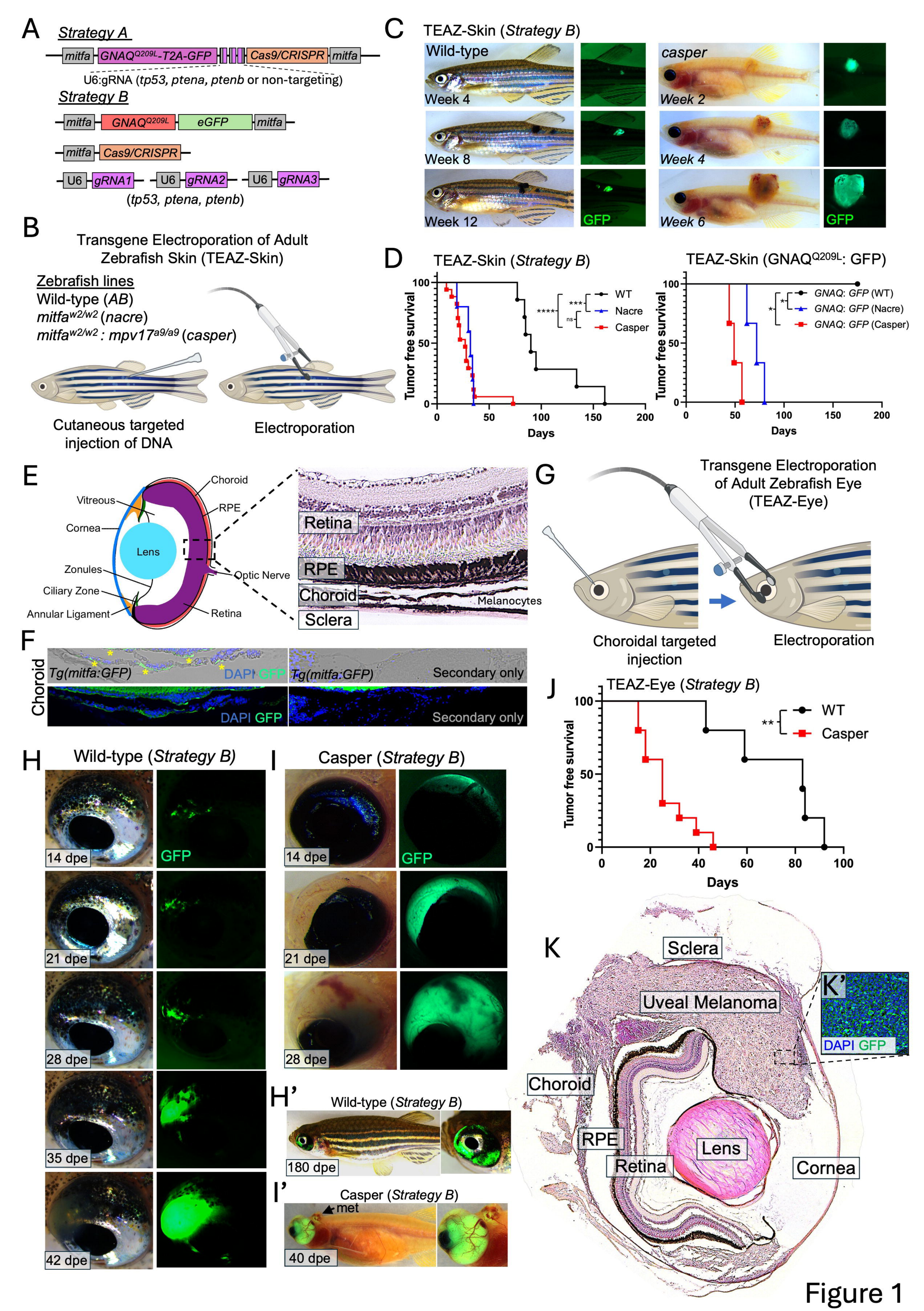
A
Strategy A
mitfa
GNAQQ209L-T2A-GFP
Cas9/CRISPR
mitfa
U6:gRNA (tp53, ptena, ptenb or non-targeting)
Strategy B
mitfa
GNAQQ209L
eGFP
mitfa
mitfa
Cas9/CRISPR
U6
gRNA1
U6
gRNA2
U6
gRNA3
(tp53, ptena, ptenb)
B
Transgene Electroporation of Adult Zebrafish Skin (TEAZ-Skin)
Zebrafish lines
Wild-type (AB)
mitfaw2/w2 (nacre)
mitfaw2/w2 : mpv17a9/a9 (casper)
Cutaneous targeted injection of DNA
Electroporation
C
TEAZ-Skin (Strategy B)
Wild-type
Week 4
Week 8
Week 12
GFP
casper
Week 2
Week 4
Week 6
GFP
D
TEAZ-Skin (Strategy B)
Tumor free survival
Days
WT
Nacre
Casper
TEAZ-Skin (GNAQQ209L: GFP)
GNAQ: GFP (WT)
GNAQ: GFP (Nacre)
GNAQ: GFP (Casper)
E
Choroid
Vitreous
RPE
Cornea
Lens
Zonules
Optic Nerve
Ciliary Zone
Annular Ligament
Retina
Retina
RPE
Choroid
Melanocytes
Sclera
F
Choroid
Tg(mitfa:GFP)
DAPI GFP
Secondary only
G
Transgene Electroporation of Adult Zebrafish Eye (TEAZ-Eye)
Choroidal targeted injection
Electroporation
H
Wild-type (Strategy B)
14 dpe
GFP
21 dpe
28 dpe
35 dpe
42 dpe
I
Casper (Strategy B)
14 dpe
GFP
21 dpe
28 dpe
H'
Wild-type (Strategy B)
180 dpe
I'
Casper (Strategy B)
met
40 dpe
J
TEAZ-Eye (Strategy B)
Tumor free survival
Days
WT
Casper
K
Sclera
Uveal Melanoma
K'
DAPI GFP
Choroid
RPE
Retina
Lens
Cornea

Figure 1

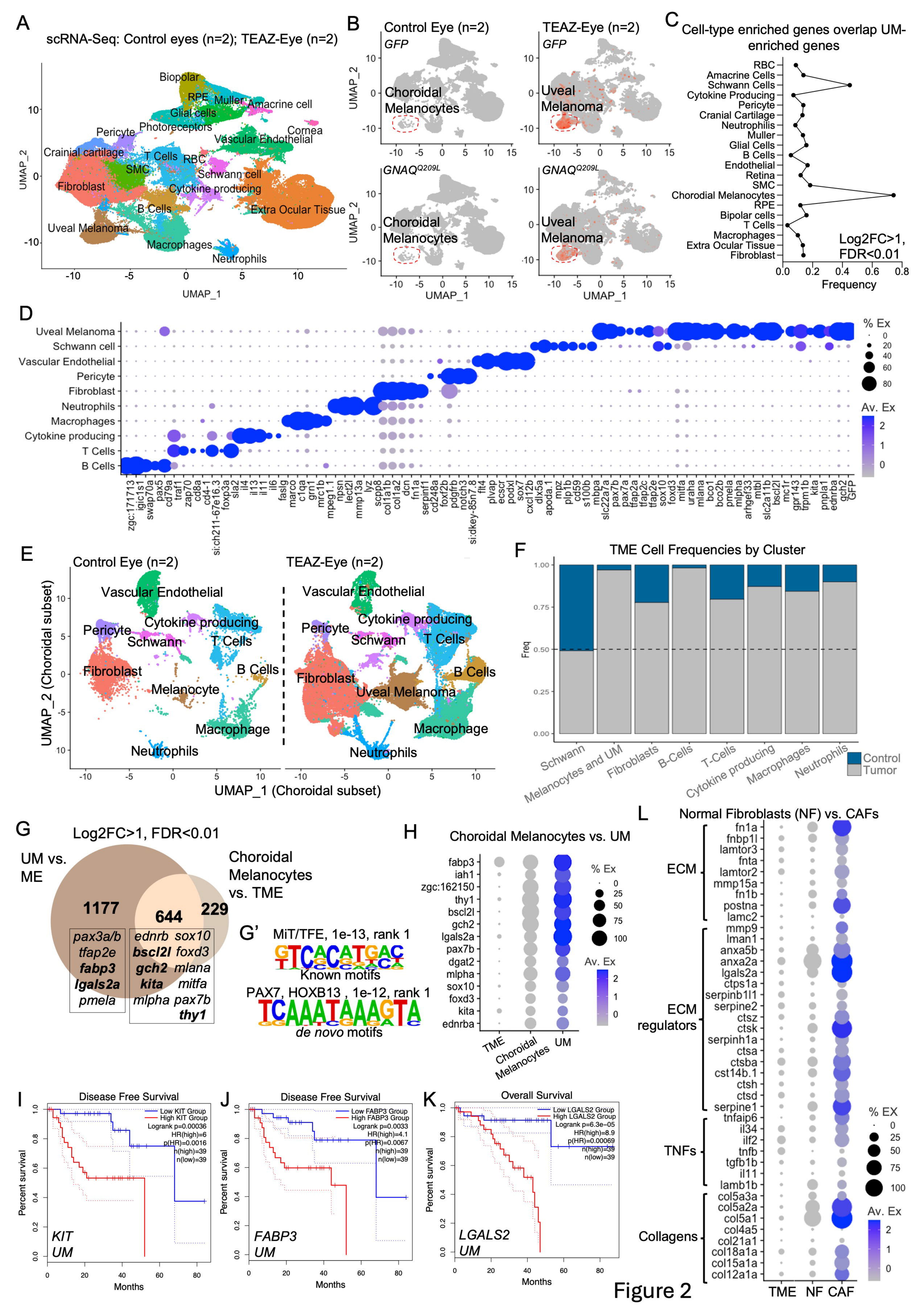
A
scRNA-Seq: Control eyes (n=2); TEAZ-Eye (n=2)
Biopolar
RPE
Muller
Amacrine cell
Glial cells
Photoreceptors
Pericyte
Cornea
Vascular Endothelial
Crainial cartilage
T Cells
RBC
SMC
Schwann cell
Fibroblast
Cytokine producing
B Cells
Extra Ocular Tissue
Uveal Melanoma
Macrophages
Neutrophils
UMAP_1
UMAP_2
B
Control Eye (n=2)
TEAZ-Eye (n=2)
GFP
Choroidal Melanocytes
Uveal Melanoma
GNAQQ209L
C
Cell-type enriched genes overlap UM-enriched genes
RBC
Amacrine Cells
Schwann Cells
Cytokine Producing
Pericyte
Cranial Cartilage
Neutrophilis
Muller
Glial Cells
B Cells
Endothelial
Retina
SMC
Chorodial Melanocytes
RPE
Bipolar cells
T Cells
Macrophages
Extra Ocular Tissue
Fibroblast
Log2FC>1, FDR<0.01
Frequency
D
Uveal Melanoma
Schwann cell
Vascular Endothelial
Pericyte
Fibroblast
Neutrophils
Macrophages
Cytokine producing
T Cells
B Cells
% Ex
Av. Ex
E
Control Eye (n=2)
TEAZ-Eye (n=2)
Vascular Endothelial
Cytokine producing
Pericyte
Schwann
T Cells
Fibroblast
B Cells
Melanocyte
Uveal Melanoma
Macrophage
Neutrophils
UMAP_1 (Choroidal subset)
UMAP_2 (Choroidal subset)
F
TME Cell Frequencies by Cluster
Freq
Schwann
Melanocytes and UM
Fibroblasts
B-Cells
T-Cells
Cytokine producing
Macrophages
Neutrophils
Control
Tumor
G
Log2FC>1, FDR<0.01
UM vs. ME
Choroidal Melanocytes vs. TME
1177
644
229
pax3a/b
tfap2e
fabp3
lgals2a
pmela
ednrb sox10
bscl2l foxd3
gch2 mlana
kita mitfa
mlpha pax7b
thy1
G'
MiT/TFE, 1e-13, rank 1
Known motifs
PAX7, HOXB13 , 1e-12, rank 1
de novo motifs
H
Choroidal Melanocytes vs. UM
fabp3
iah1
zgc:162150
thy1
bscl2l
gch2
lgals2a
pax7b
dgat2
mlpha
sox10
foxd3
kita
ednrba
TME
Choroidal Melanocytes
UM
% Ex
Av. Ex
L
Normal Fibroblasts (NF) vs. CAFs
ECM
fn1a
fnbp1l
lamtor3
fnta
lamtor2
mmp15a
fn1b
postna
lamc2
ECM regulators
mmp9
lman1
anxa5b
anxa2a
lgals2a
ctps1a
serpinb1l1
serpine2
ctsz
ctsk
serpinh1a
ctsa
ctsba
cst14b.1
ctsh
ctsd
serpine1
TNFs
tnfaip6
il34
ilf2
tnfb
tgfb1b
il11
lamb1b
Collagens
col5a3a
col5a2a
col5a1
col4a5
col21a1
col18a1a
col15a1a
col12a1a
TME NF CAF
% EX
Av. Ex
I
Disease Free Survival
Low KIT Group
High KIT Group
Logrank p=0.00036
HR(high)=6
p(HR)=0.0016
n(high)=39
n(low)=39
KIT
UM
Percent survival
Months
J
Disease Free Survival
Low FABP3 Group
High FABP3 Group
Logrank p=0.0033
HR(high)=4.1
p(HR)=0.0067
n(high)=39
n(low)=39
FABP3
UM
K
Overall Survival
Low LGALS2 Group
High LGALS2 Group
Logrank p=6.3e-05
HR(high)=8.9
p(HR)=0.00069
n(high)=39
n(low)=39
LGALS2
UM

Figure 2

A

Control eye (n=3); Control skin (n=2); TEAZ-Eye (n=2), TEAZ-Skin (n=2)

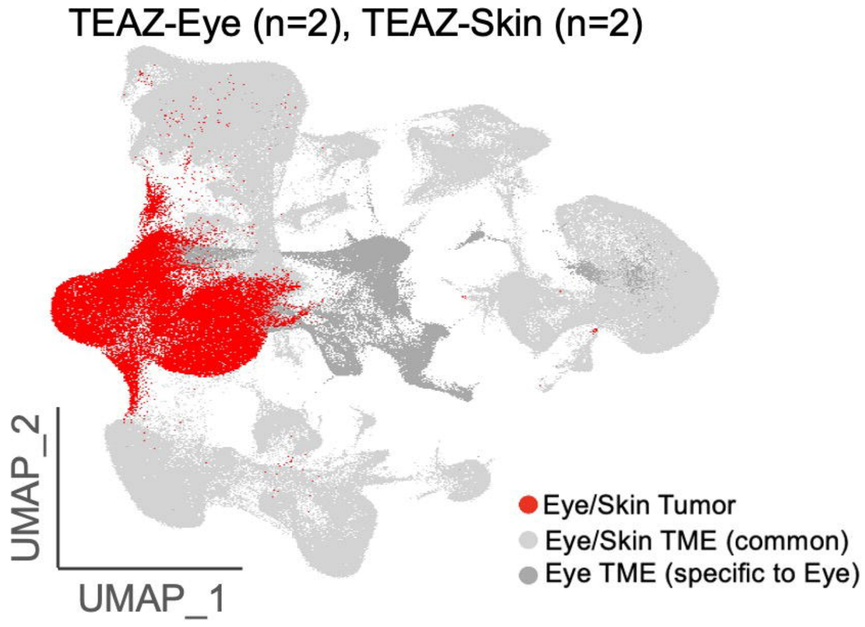

B

Comparison of Primary Melanocytes and GNAQ-induced Melanoma Across Eye and Skin

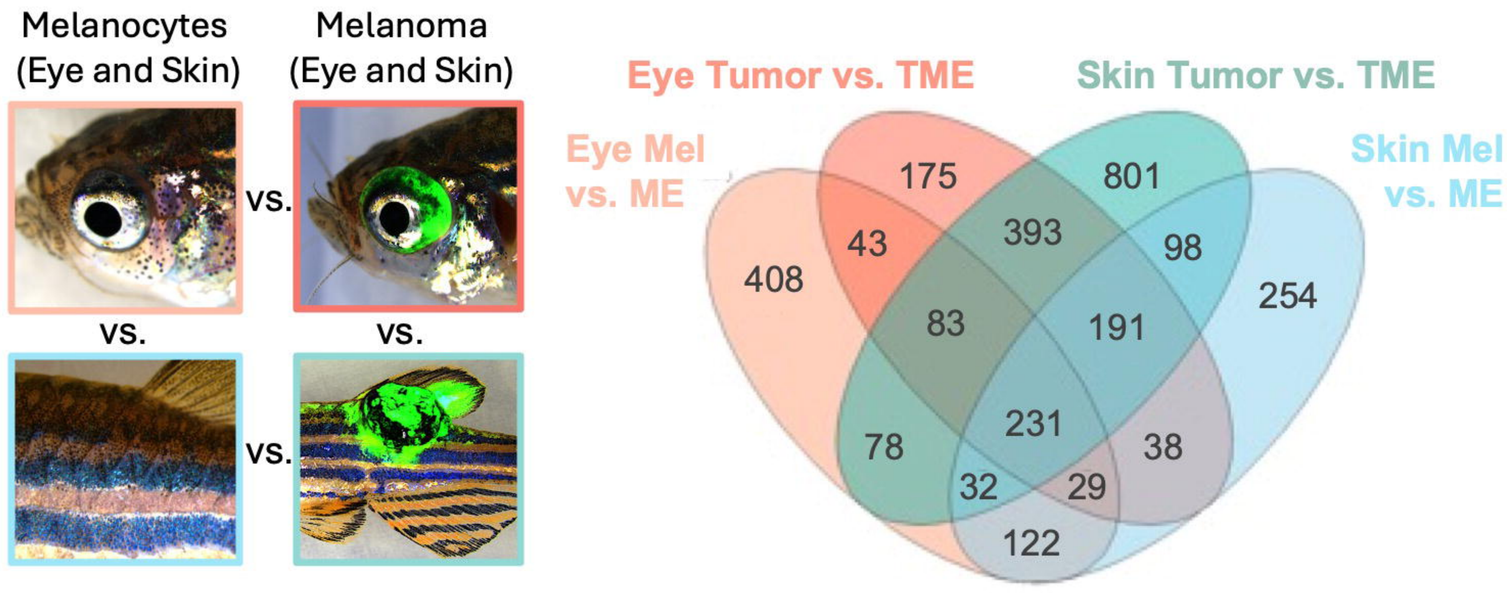

C

Gene sets	Overlap/total genes	Percentage
Skin Tumor and Skin Melanocytes	552/2350	23.5%
Eye Tumor and Eye Melanocytes	386/1823	21.2%
Skin Tumor and Eye Tumor	898/2192	41.0%
Skin Melanocytes and Eye Melanocytes	414/1607	25.8%
All four conditions	231/4418	5.2%
Skin Tumor and Eye Melanocytes	424/2509	16.9%
Eye Tumor and Skin Melanocytes	489/1689	29.0%

D

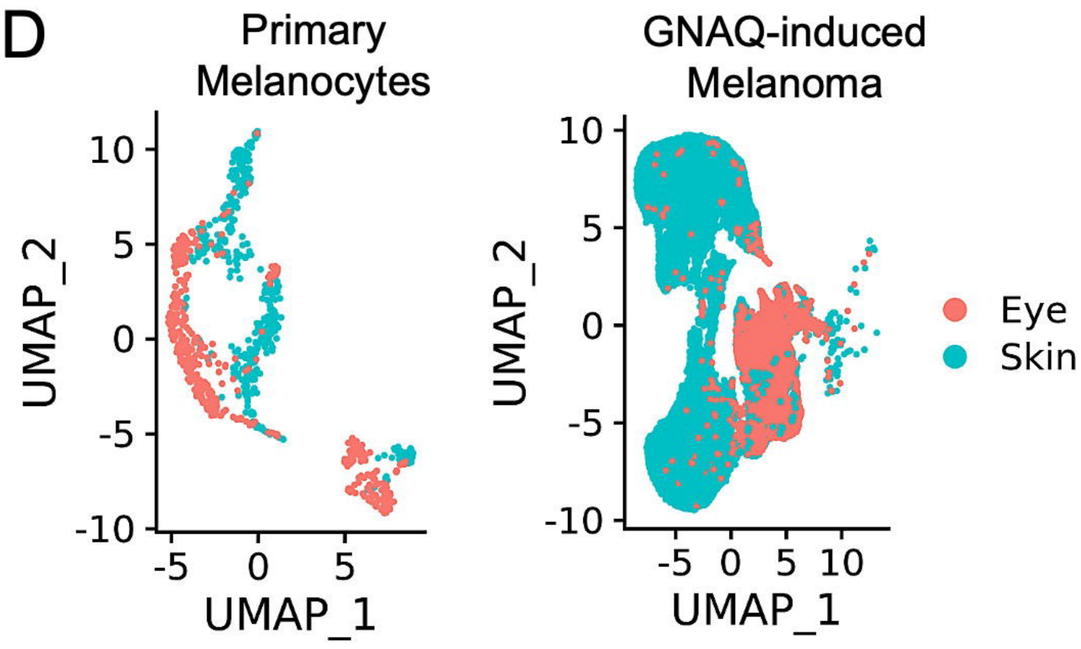

E

DEGs: Primary Melanocytes Eye vs. Skin (FDR<0.01, Log2FC >|0.5|)

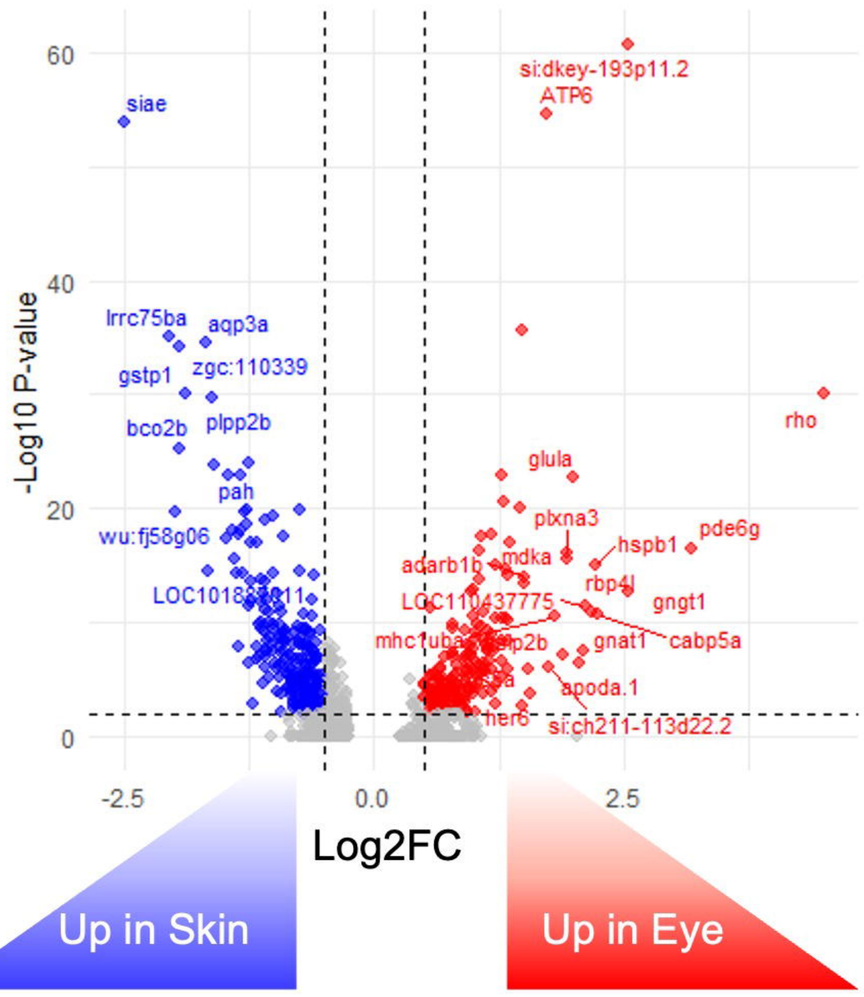

F

DEGs: GNAQ-induced Melanoma Eye vs. Skin (FDR<0.01, Log2FC >|0.5|)

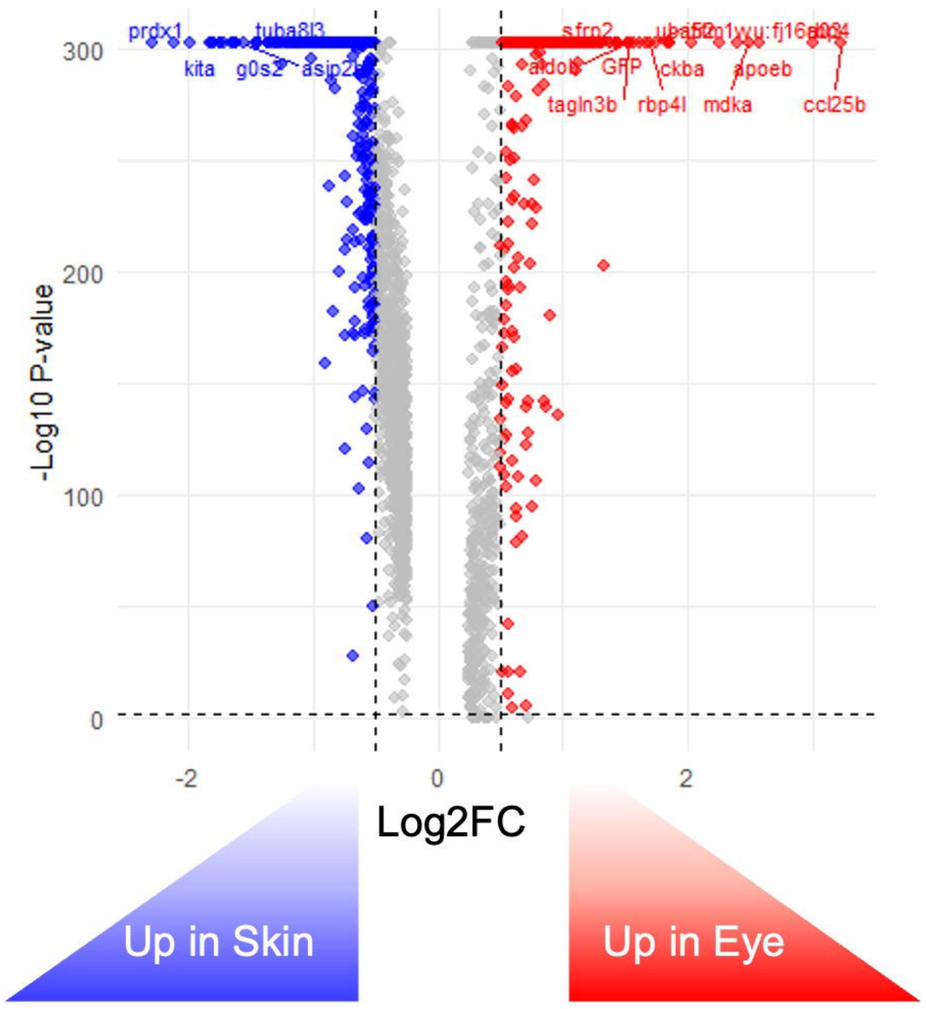

G

DNA Repair

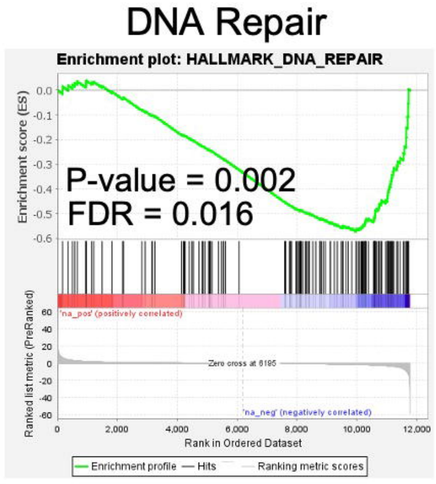

Oxidative phosphorylation

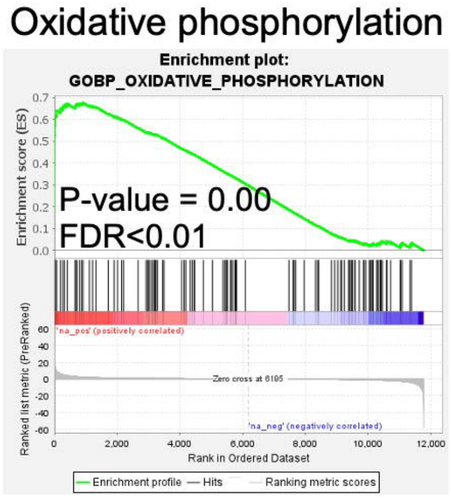

UV Response Up

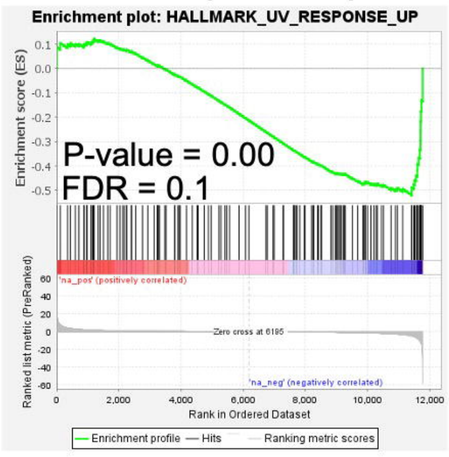

UV Response Down

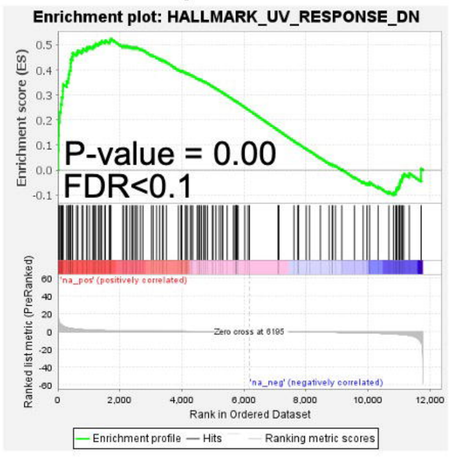

H

PI3K/AKT/MTOR

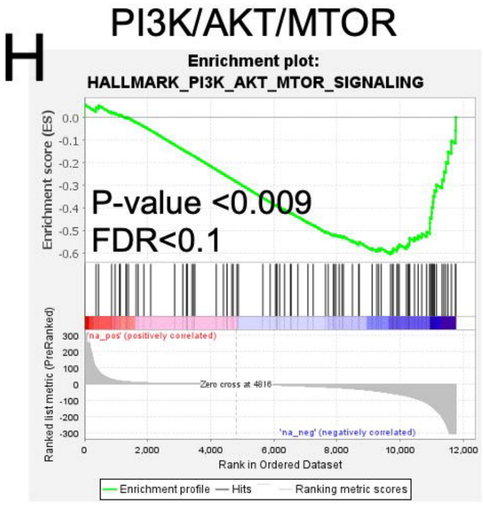

EMT transition

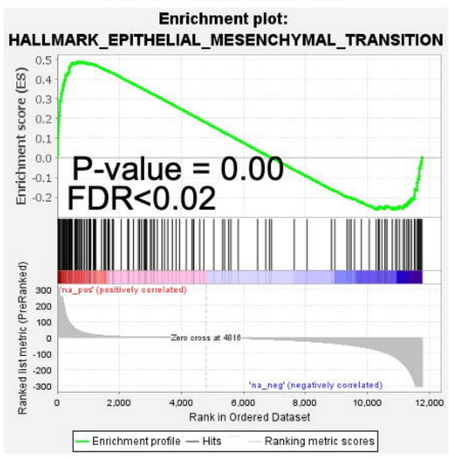

RHO GTPase

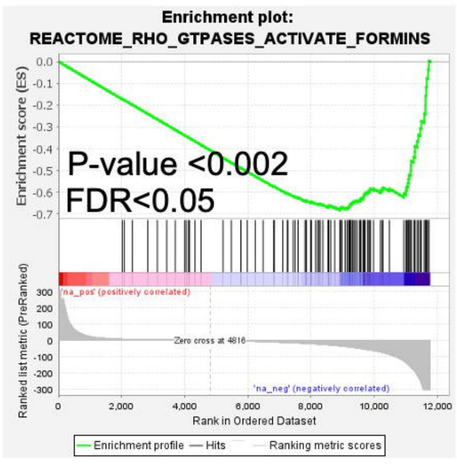

Selenoamino acid metabolism

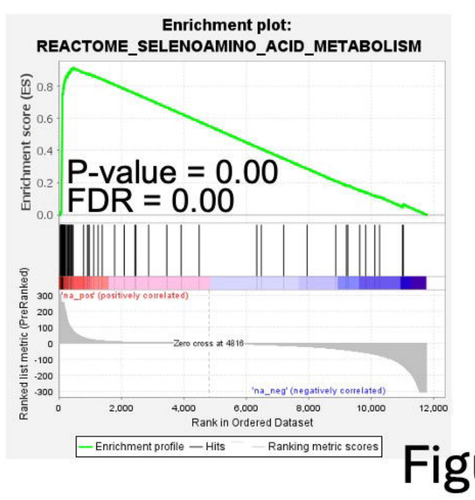

Figure 3

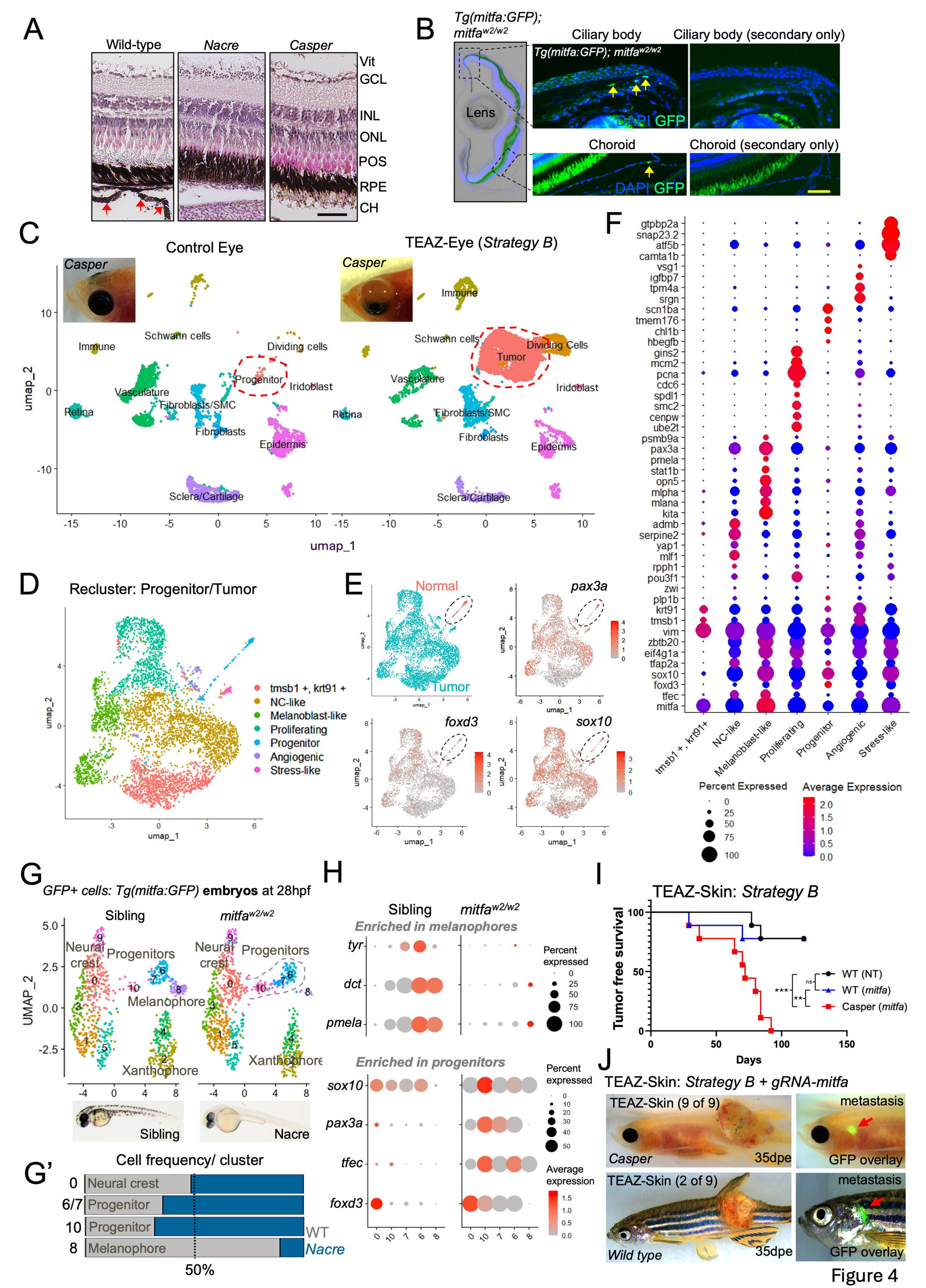
A
Wild-type
Nacre
Casper
Vit
GCL
INL
ONL
POS
RPE
CH
B
Tg(mitfa:GFP); mitfa w2/w2
Lens
Ciliary body
Ciliary body (secondary only)
Choroid
Choroid (secondary only)
DAPI GFP
C
Control Eye
TEAZ-Eye (Strategy B)
Casper
Immune
Schwann cells
Dividing cells
Dividing Cells
Tumor
Progenitor
Iridoblast
Vasculature
Fibroblasts/SMC
Fibroblasts
Retina
Epidermis
Sclera/Cartilage
umap_1
umap_2
D
Recluster: Progenitor/Tumor
tmsb1 +, krt91 +
NC-like
Melanoblast-like
Proliferating
Progenitor
Angiogenic
Stress-like
E
Normal
Tumor
pax3a
foxd3
sox10
F
gtpbp2a
snap23.2
atf5b
camta1b
vsg1
igfbp7
tpm4a
srgn
scn1ba
tmem176
chl1b
hbegfb
gins2
mcm2
pcna
cdc6
spdl1
smc2
cenpw
ube2t
psmb9a
pax3a
pmela
stat1b
opn5
mlpha
mlana
kita
admb
serpine2
yap1
mlf1
rpph1
pou3f1
zwi
plp1b
krt91
tmsb1
vim
zbtb20
eif4g1a
tfap2a
sox10
foxd3
tfec
mitfa
tmsb1 +, krt91+
NC-like
Melanoblast-like
Proliferating
Progenitor
Angiogenic
Stress-like
Percent Expressed
Average Expression
G
GFP+ cells: Tg(mitfa:GFP) embryos at 28hpf
Sibling
mitfa w2/w2
Neural crest
Progenitors
Melanophore
Xanthophore
UMAP_2
Sibling
Nacre
G'
Cell frequency/ cluster
0 Neural crest
6/7 Progenitor
10 Progenitor
8 Melanophore
WT
Nacre
50%
H
Sibling
mitfa w2/w2
Enriched in melanophores
tyr
dct
pmela
Enriched in progenitors
sox10
pax3a
tfec
foxd3
Percent expressed
Average expression
I
TEAZ-Skin: Strategy B
Tumor free survival
Days
WT (NT)
WT (mitfa)
Casper (mitfa)
J
TEAZ-Skin: Strategy B + gRNA-mitfa
TEAZ-Skin (9 of 9)
Casper
35dpe
metastasis
GFP overlay
TEAZ-Skin (2 of 9)
Wild type
35dpe
metastasis
GFP overlay

Figure 4

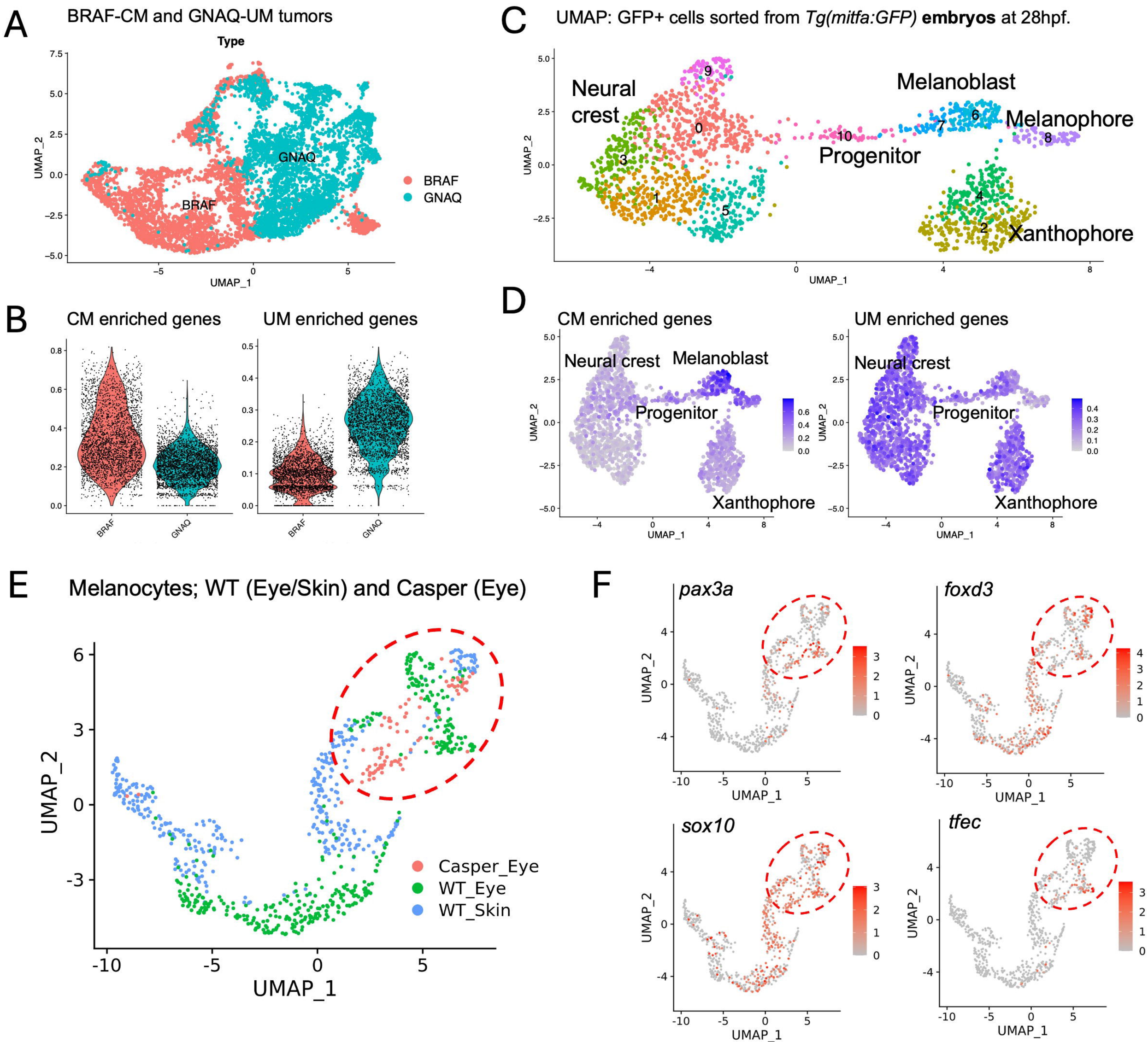
A
BRAF-CM and GNAQ-UM tumors
Type
GNAQ
BRAF
BRAF
GNAQ
UMAP_1
UMAP_2
B
CM enriched genes
UM enriched genes
BRAF
GNAQ
C
UMAP: GFP+ cells sorted from Tg(mitfa:GFP) embryos at 28hpf.
Neural crest
Melanoblast
Melanophore
Progenitor
Xanthophore
D
CM enriched genes
UM enriched genes
Neural crest
Melanoblast
Progenitor
Xanthophore
E
Melanocytes; WT (Eye/Skin) and Casper (Eye)
Casper_Eye
WT_Eye
WT_Skin
F
pax3a
foxd3
sox10
tfec

Figure 5

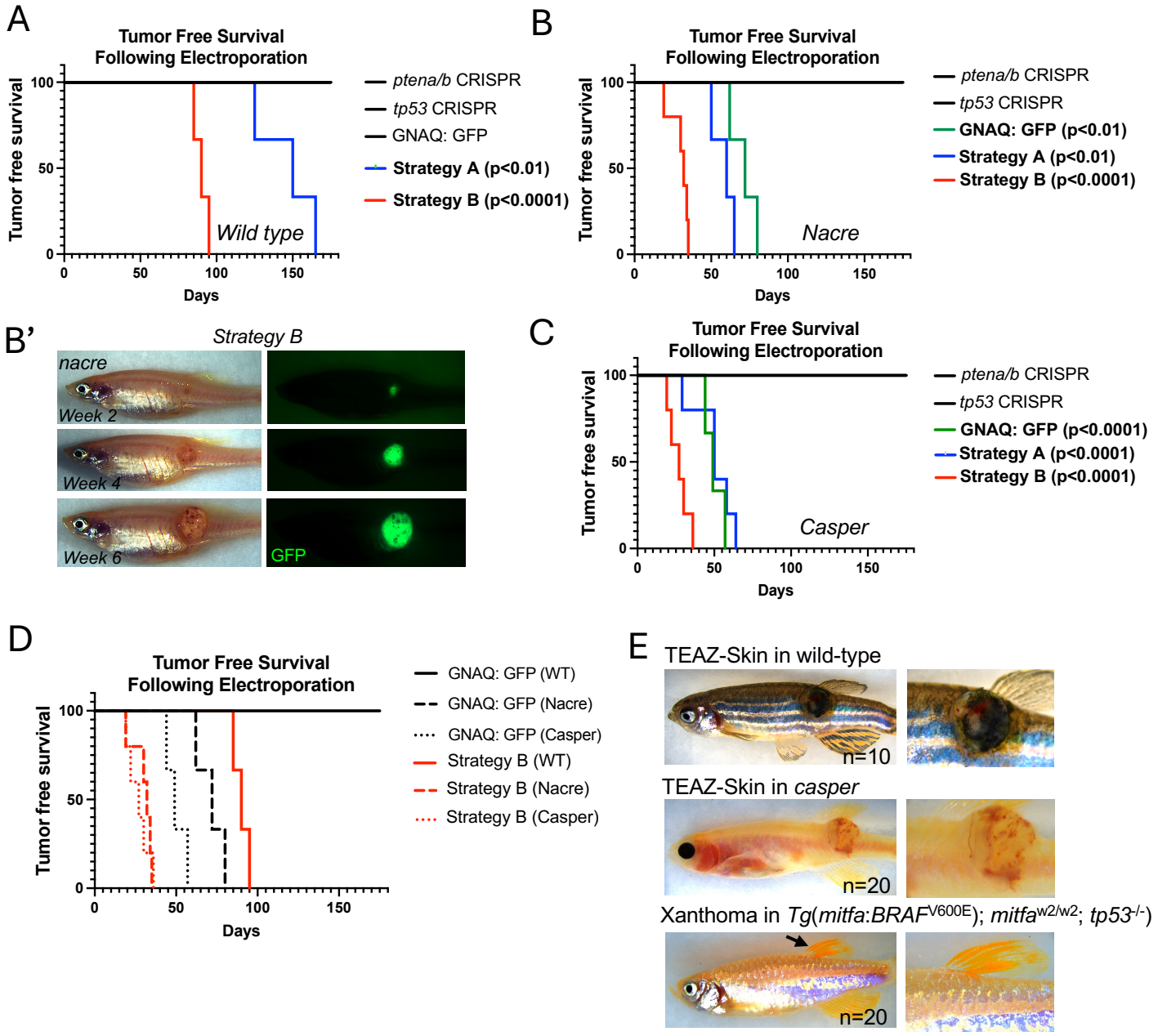
A
Tumor Free Survival
Following Electroporation
Tumor free survival
Days
Wild type
ptena/b CRISPR
tp53 CRISPR
GNAQ: GFP
Strategy A (p<0.01)
Strategy B (p<0.0001)
B
Tumor Free Survival
Following Electroporation
Nacre
ptena/b CRISPR
tp53 CRISPR
GNAQ: GFP (p<0.01)
Strategy A (p<0.01)
Strategy B (p<0.0001)
B'
Strategy B
nacre
Week 2
Week 4
Week 6
GFP
C
Tumor Free Survival
Following Electroporation
Casper
ptena/b CRISPR
tp53 CRISPR
GNAQ: GFP (p<0.0001)
Strategy A (p<0.0001)
Strategy B (p<0.0001)
D
Tumor Free Survival
Following Electroporation
GNAQ: GFP (WT)
GNAQ: GFP (Nacre)
GNAQ: GFP (Casper)
Strategy B (WT)
Strategy B (Nacre)
Strategy B (Casper)
E
TEAZ-Skin in wild-type
n=10
TEAZ-Skin in casper
n=20
Xanthoma in Tg(mitfa:BRAFV600E); mitfaw2/w2; tp53-/-)
n=20

FIGURE S1

Tumor #	ptena	ptenb	tp53	# of edited genes
1				**3**
2				**3**
3				**2**
4				**3**
5				**3**
6				**3**
7				**3**
8				**3**
9				**3**
10				**3**
11				**3**
Germline	**ptena**	**ptenb**	**tp53**	
WT1				**0**
WT2				**0**

CRISPR editing

No editing

FIGURE S2

A

Tg(mitfa-GFP) Zebrafish Line

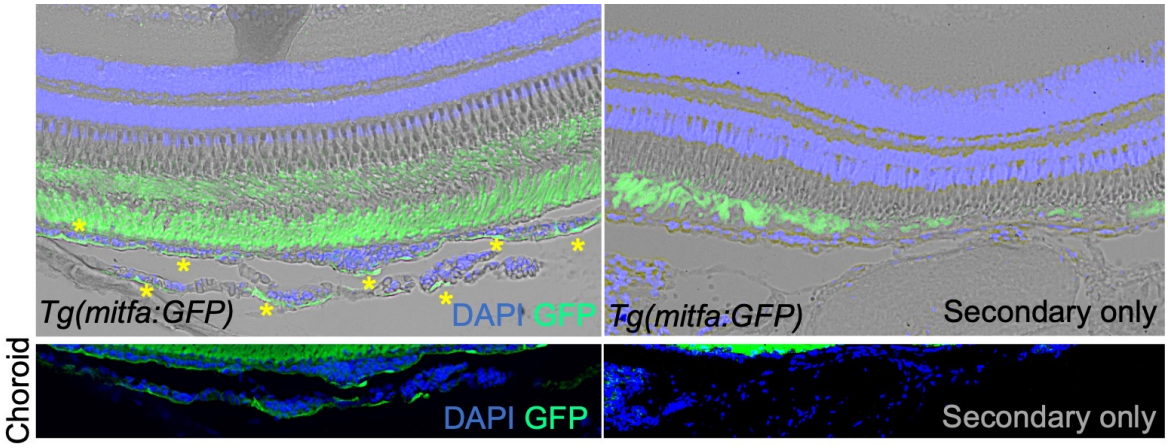

B

Tg(mitfa-GFP) Zebrafish Line

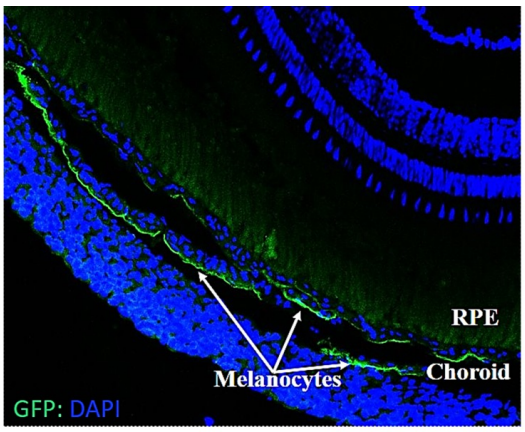

Anti-GFP IF

C

TEAZ-Eye using *mitfa:GFP* plasmids into WT Zebrafish

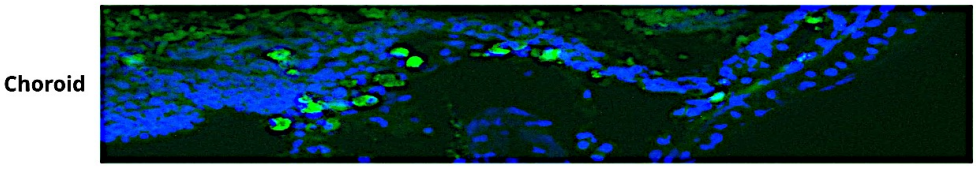

Anti-GFP IF

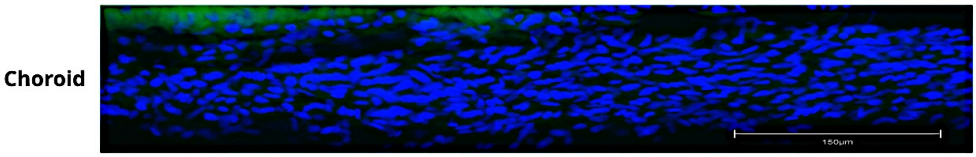

Secondary-only Control

FIGURE S3

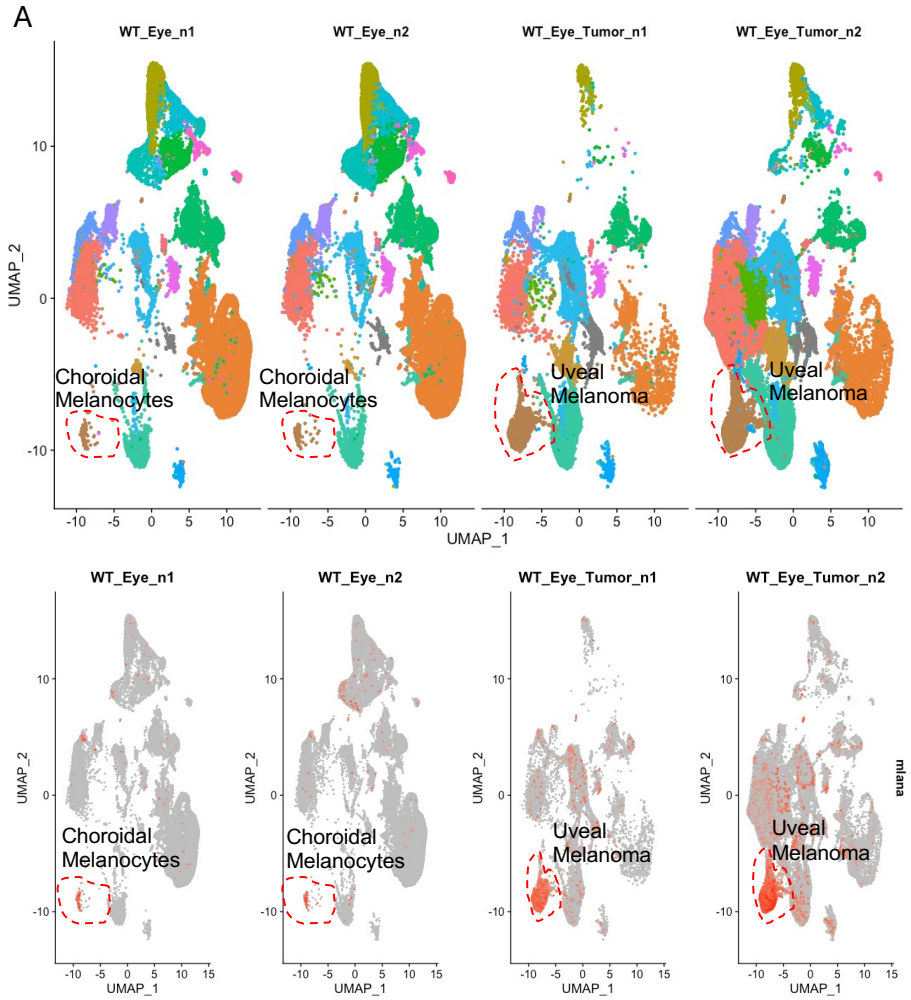
A
WT_Eye_n1
WT_Eye_n2
WT_Eye_Tumor_n1
WT_Eye_Tumor_n2
UMAP_2
UMAP_1
Choroidal Melanocytes
Uveal Melanoma
mlana

FIGURE S4

Single-cell RNA seq Replicates

Tissue	Genotype	Replicate 1 (pooled tissue, tumors)	Replicate 2 (pooled tissue, tumors)
Skin	Wild-type	1 skin sample 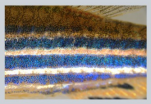	1 skin sample 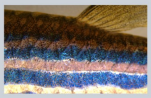
Skin Tumor	Wild-type	1 tumor sample 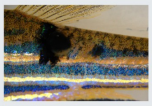 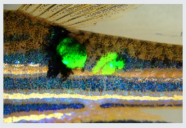	1 tumor sample 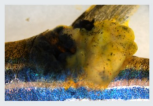 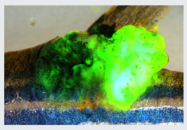
Eye Paired (tumor matched bilateral eye)	Wild-type	2 pooled eyes 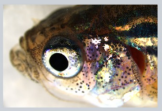 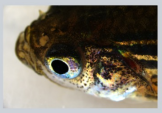	
Eye sibling matched	Wild-type	4 pooled eyes 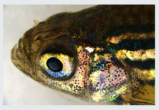 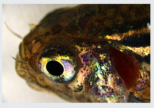 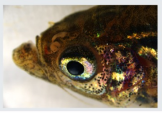	
Eye mock injected, sibling matched	Wild-type	3 pooled eyes 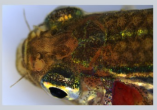 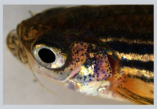 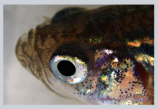	
Eye Tumor	Wild-type	1 tumor sample	2 pooled tumor samples 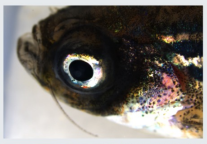 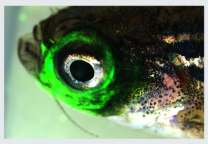 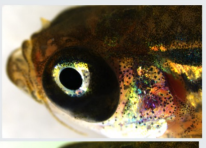

FIGURE S5

A

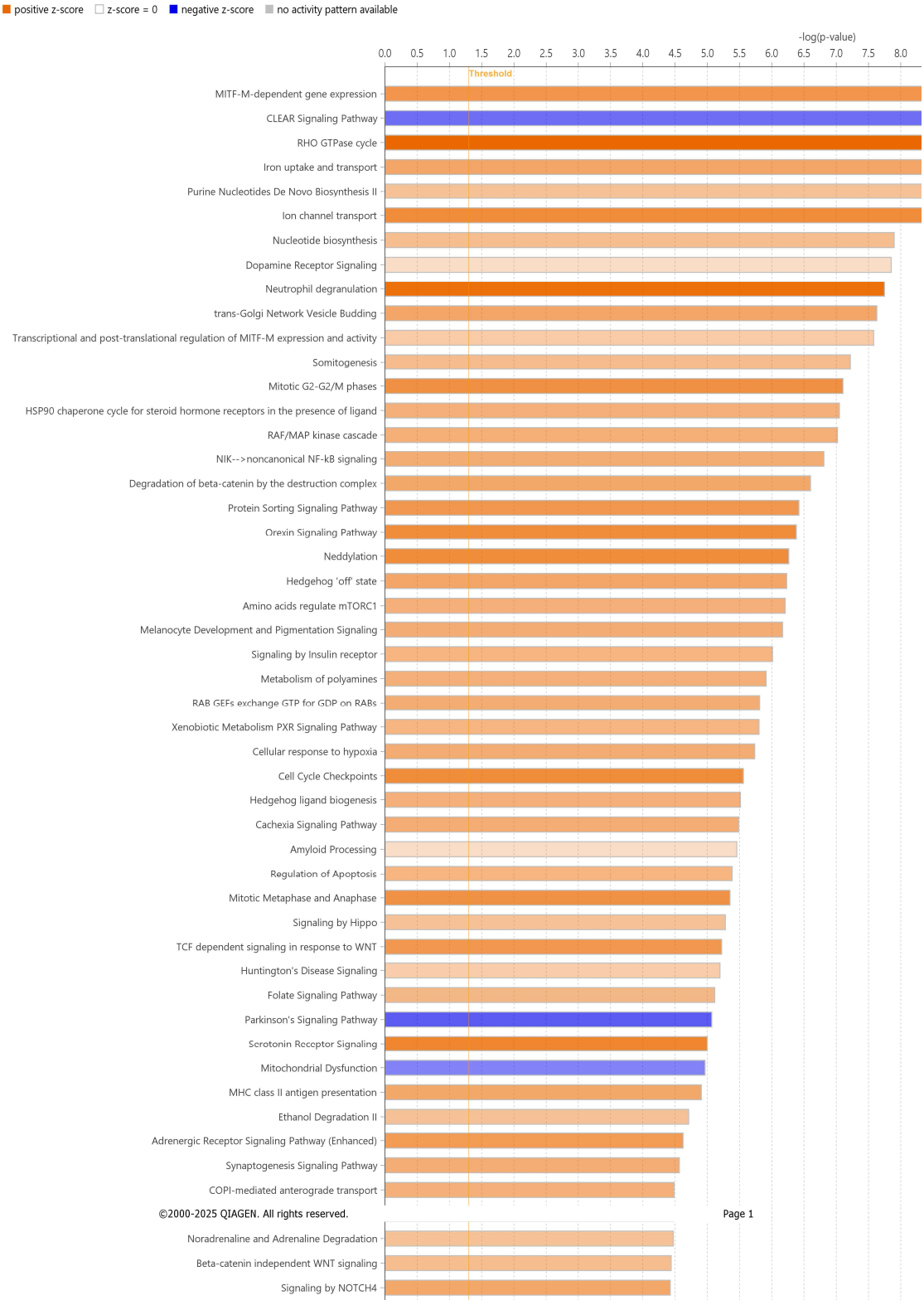
positive z-score
z-score = 0
negative z-score
no activity pattern available
-log(p-value)
0.0 0.5 1.0 1.5 2.0 2.5 3.0 3.5 4.0 4.5 5.0 5.5 6.0 6.5 7.0 7.5 8.0
Threshold
MITF-M-dependent gene expression
CLEAR Signaling Pathway
RHO GTPase cycle
Iron uptake and transport
Purine Nucleotides De Novo Biosynthesis II
Ion channel transport
Nucleotide biosynthesis
Dopamine Receptor Signaling
Neutrophil degranulation
trans-Golgi Network Vesicle Budding
Transcriptional and post-translational regulation of MITF-M expression and activity
Somitogenesis
Mitotic G2-G2/M phases
HSP90 chaperone cycle for steroid hormone receptors in the presence of ligand
RAF/MAP kinase cascade
NIK-->noncanonical NF-kB signaling
Degradation of beta-catenin by the destruction complex
Protein Sorting Signaling Pathway
Orexin Signaling Pathway
Neddylation
Hedgehog 'off' state
Amino acids regulate mTORC1
Melanocyte Development and Pigmentation Signaling
Signaling by Insulin receptor
Metabolism of polyamines
RAB GEFs exchange GTP for GDP on RABs
Xenobiotic Metabolism PXR Signaling Pathway
Cellular response to hypoxia
Cell Cycle Checkpoints
Hedgehog ligand biogenesis
Cachexia Signaling Pathway
Amyloid Processing
Regulation of Apoptosis
Mitotic Metaphase and Anaphase
Signaling by Hippo
TCF dependent signaling in response to WNT
Huntington's Disease Signaling
Folate Signaling Pathway
Parkinson's Signaling Pathway
Serotonin Receptor Signaling
Mitochondrial Dysfunction
MHC class II antigen presentation
Ethanol Degradation II
Adrenergic Receptor Signaling Pathway (Enhanced)
Synaptogenesis Signaling Pathway
COPI-mediated anterograde transport
©2000-2025 QIAGEN. All rights reserved.
Page 1
Noradrenaline and Adrenaline Degradation
Beta-catenin independent WNT signaling
Signaling by NOTCH4

B

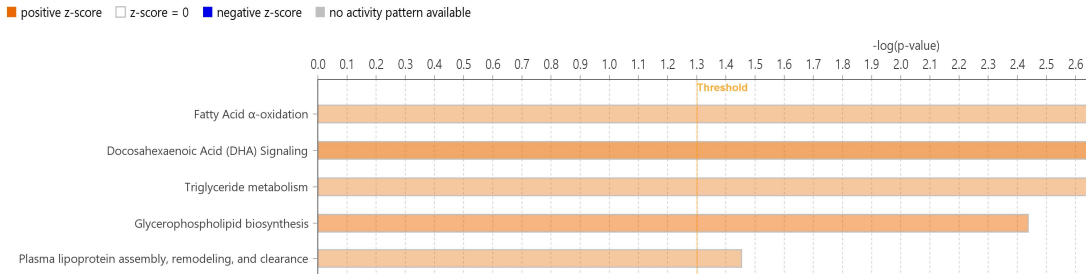
positive z-score
z-score = 0
negative z-score
no activity pattern available
-log(p-value)
0.0 0.1 0.2 0.3 0.4 0.5 0.6 0.7 0.8 0.9 1.0 1.1 1.2 1.3 1.4 1.5 1.6 1.7 1.8 1.9 2.0 2.1 2.2 2.3 2.4 2.5 2.6
Threshold
Fatty Acid α-oxidation
Docosahexaenoic Acid (DHA) Signaling
Triglyceride metabolism
Glycerophospholipid biosynthesis
Plasma lipoprotein assembly, remodeling, and clearance

FIGURE S6

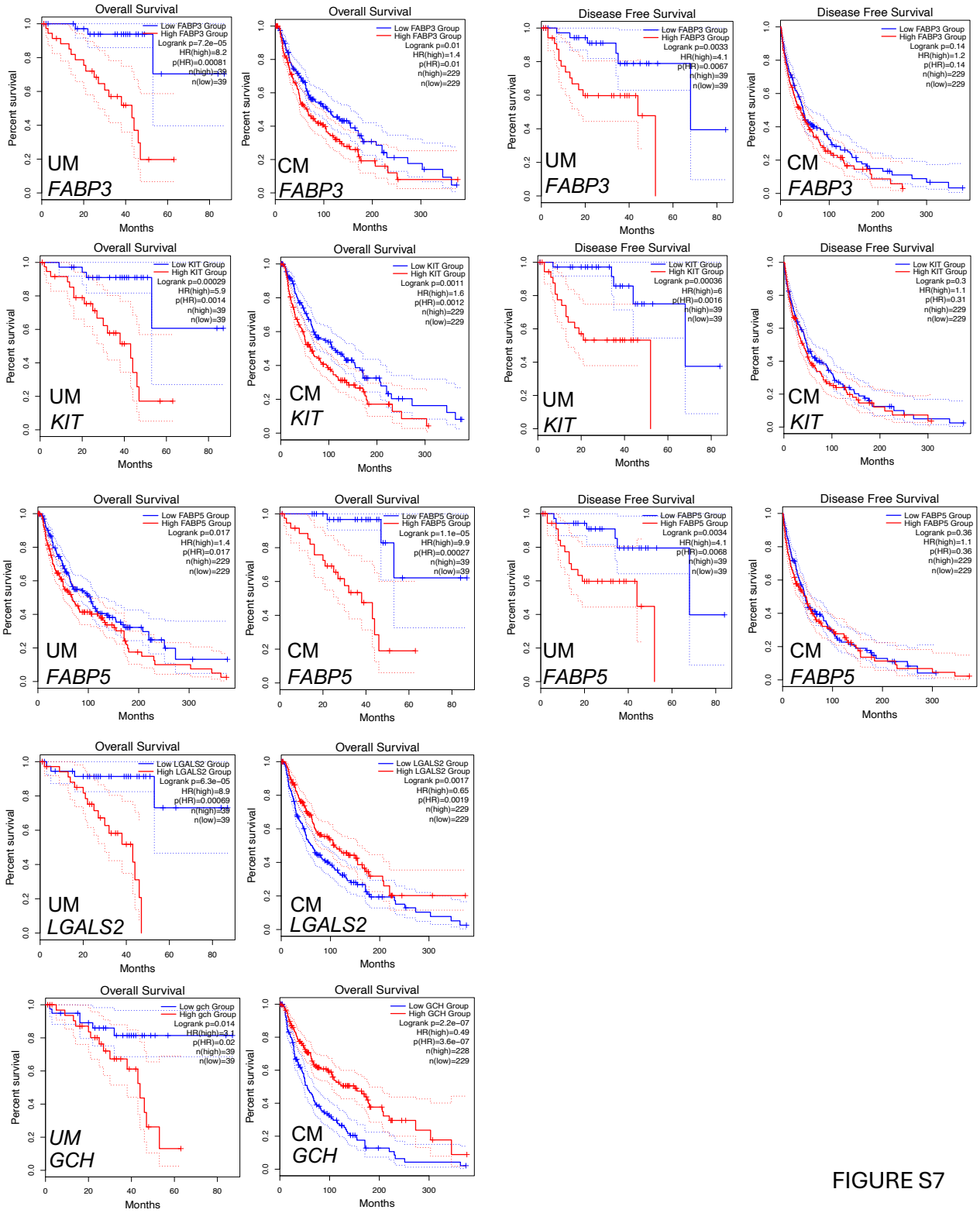
Overall Survival
Low FABP3 Group
High FABP3 Group
Logrank p=7.2e−05
HR(high)=8.2
p(HR)=0.00081
n(high)=39
n(low)=39
UM
FABP3
Overall Survival
Low FABP3 Group
High FABP3 Group
Logrank p=0.01
HR(high)=1.4
p(HR)=0.01
n(high)=229
n(low)=229
CM
FABP3
Disease Free Survival
Low FABP3 Group
High FABP3 Group
Logrank p=0.0033
HR(high)=4.1
p(HR)=0.0067
n(high)=39
n(low)=39
UM
FABP3
Disease Free Survival
Low FABP3 Group
High FABP3 Group
Logrank p=0.14
HR(high)=1.2
p(HR)=0.14
n(high)=229
n(low)=229
CM
FABP3
Overall Survival
Low KIT Group
High KIT Group
Logrank p=0.00029
HR(high)=5.9
p(HR)=0.0014
n(high)=39
n(low)=39
UM
KIT
Overall Survival
Low KIT Group
High KIT Group
Logrank p=0.0011
HR(high)=1.6
p(HR)=0.0012
n(high)=229
n(low)=229
CM
KIT
Disease Free Survival
Low KIT Group
High KIT Group
Logrank p=0.00036
HR(high)=6
p(HR)=0.0016
n(high)=39
n(low)=39
UM
KIT
Disease Free Survival
Low KIT Group
High KIT Group
Logrank p=0.3
HR(high)=1.1
p(HR)=0.31
n(high)=229
n(low)=229
CM
KIT
Overall Survival
Low FABP5 Group
High FABP5 Group
Logrank p=0.017
HR(high)=1.4
p(HR)=0.017
n(high)=229
n(low)=229
UM
FABP5
Overall Survival
Low FABP5 Group
High FABP5 Group
Logrank p=1.1e−05
HR(high)=9.9
p(HR)=0.00027
n(high)=39
n(low)=39
CM
FABP5
Disease Free Survival
Low FABP5 Group
High FABP5 Group
Logrank p=0.0034
HR(high)=4.1
p(HR)=0.0068
n(high)=39
n(low)=39
UM
FABP5
Disease Free Survival
Low FABP5 Group
High FABP5 Group
Logrank p=0.36
HR(high)=1.1
p(HR)=0.36
n(high)=229
n(low)=229
CM
FABP5
Overall Survival
Low LGALS2 Group
High LGALS2 Group
Logrank p=6.3e−05
HR(high)=8.9
p(HR)=0.00069
n(high)=39
n(low)=39
UM
LGALS2
Overall Survival
Low LGALS2 Group
High LGALS2 Group
Logrank p=0.0017
HR(high)=0.65
p(HR)=0.0019
n(high)=229
n(low)=229
CM
LGALS2
Overall Survival
Low gch Group
High gch Group
Logrank p=0.014
HR(high)=2.1
p(HR)=0.02
n(high)=39
n(low)=39
UM
GCH
Overall Survival
Low GCH Group
High GCH Group
Logrank p=2.2e−07
HR(high)=0.49
p(HR)=3.6e−07
n(high)=228
n(low)=229
CM
GCH
Percent survival
Months

FIGURE S7

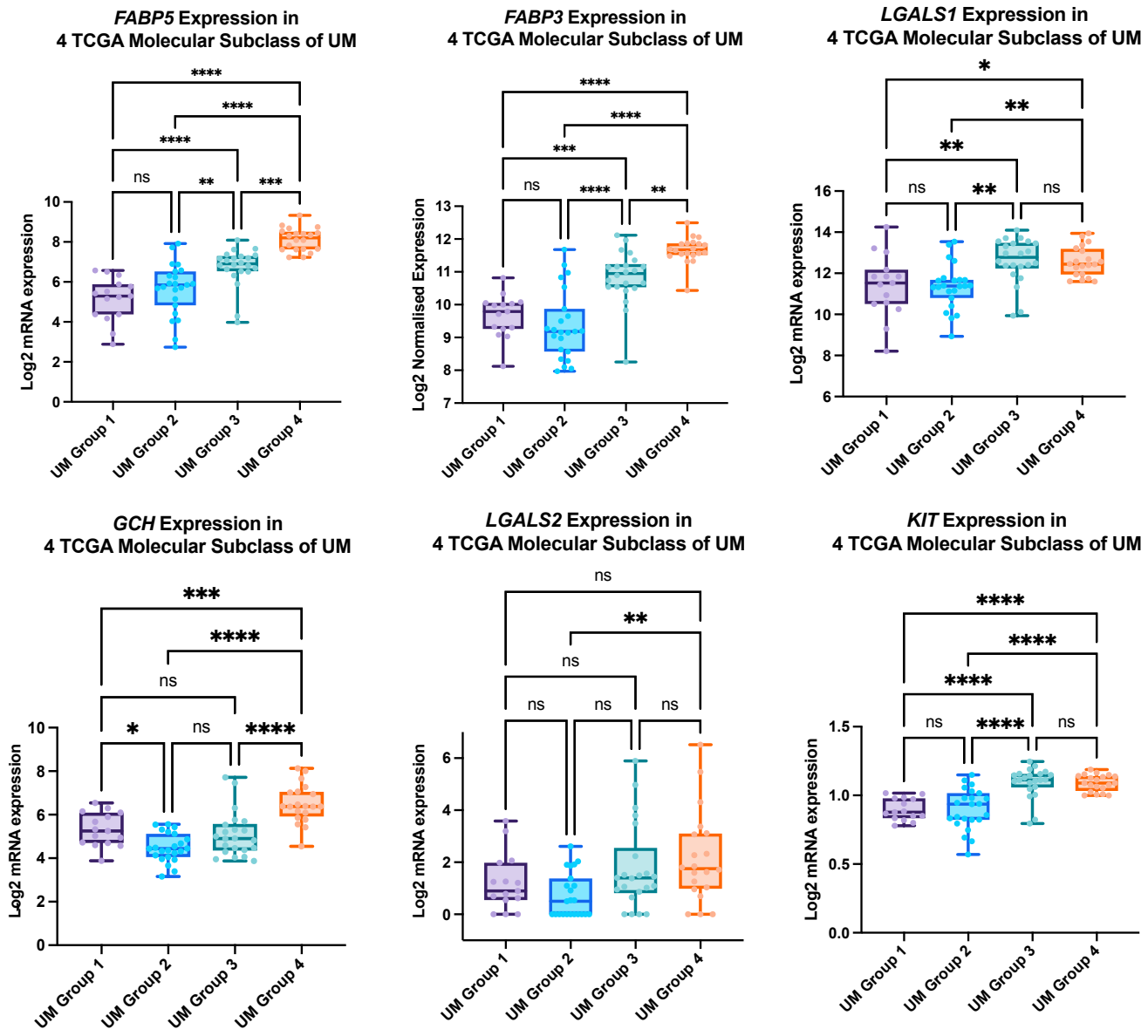
FABP5 Expression in
4 TCGA Molecular Subclass of UM
Log2 mRNA expression
FABP3 Expression in
4 TCGA Molecular Subclass of UM
Log2 Normalised Expression
LGALS1 Expression in
4 TCGA Molecular Subclass of UM
Log2 mRNA expression
GCH Expression in
4 TCGA Molecular Subclass of UM
Log2 mRNA expression
LGALS2 Expression in
4 TCGA Molecular Subclass of UM
Log2 mRNA expression
KIT Expression in
4 TCGA Molecular Subclass of UM
Log2 mRNA expression
UM Group 1
UM Group 2
UM Group 3
UM Group 4
ns
*
**
***
****

FIGURE S8

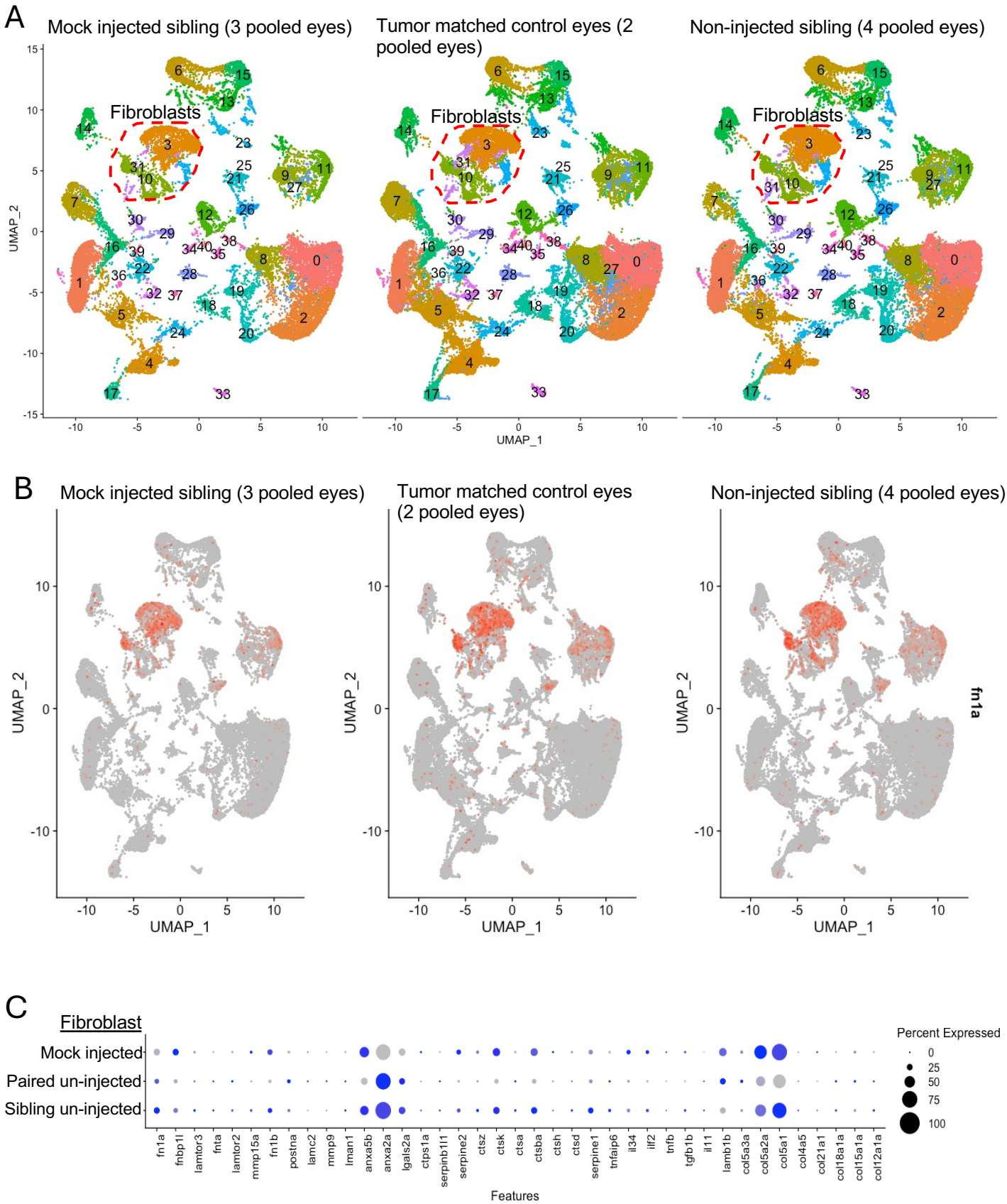
A
Mock injected sibling (3 pooled eyes)
Tumor matched control eyes (2 pooled eyes)
Non-injected sibling (4 pooled eyes)
Fibroblasts
UMAP_2
UMAP_1
B
Mock injected sibling (3 pooled eyes)
Tumor matched control eyes (2 pooled eyes)
Non-injected sibling (4 pooled eyes)
fn1a
UMAP_2
UMAP_1
C
Fibroblast
Mock injected
Paired un-injected
Sibling un-injected
fn1a
fnbp1l
lamtor3
fnta
lamtor2
mmp15a
fn1b
postna
lamc2
mmp9
lman1
anxa5b
anxa2a
lgals2a
ctps1a
serpinb1l1
serpine2
ctsz
ctsk
ctsa
ctsba
ctsh
ctsd
serpine1
tnfaip6
il34
il1f2
tnfb
tgfb1b
il11
lamb1b
col5a3a
col5a2a
col5a1
col4a5
col21a1
col18a1a
col15a1a
col12a1a
Features
Percent Expressed
0
25
50
75
100

FIGURE S9

A

B

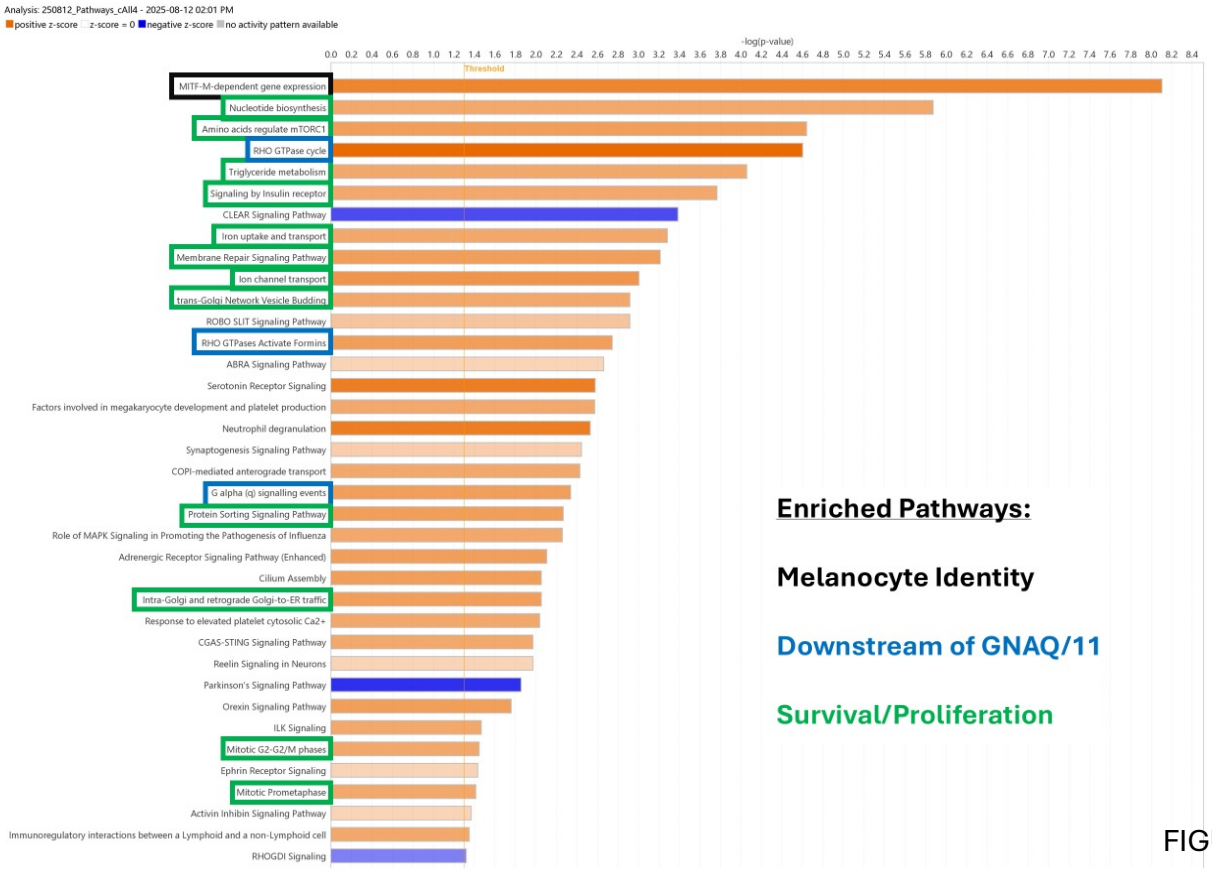

FIGURE S10

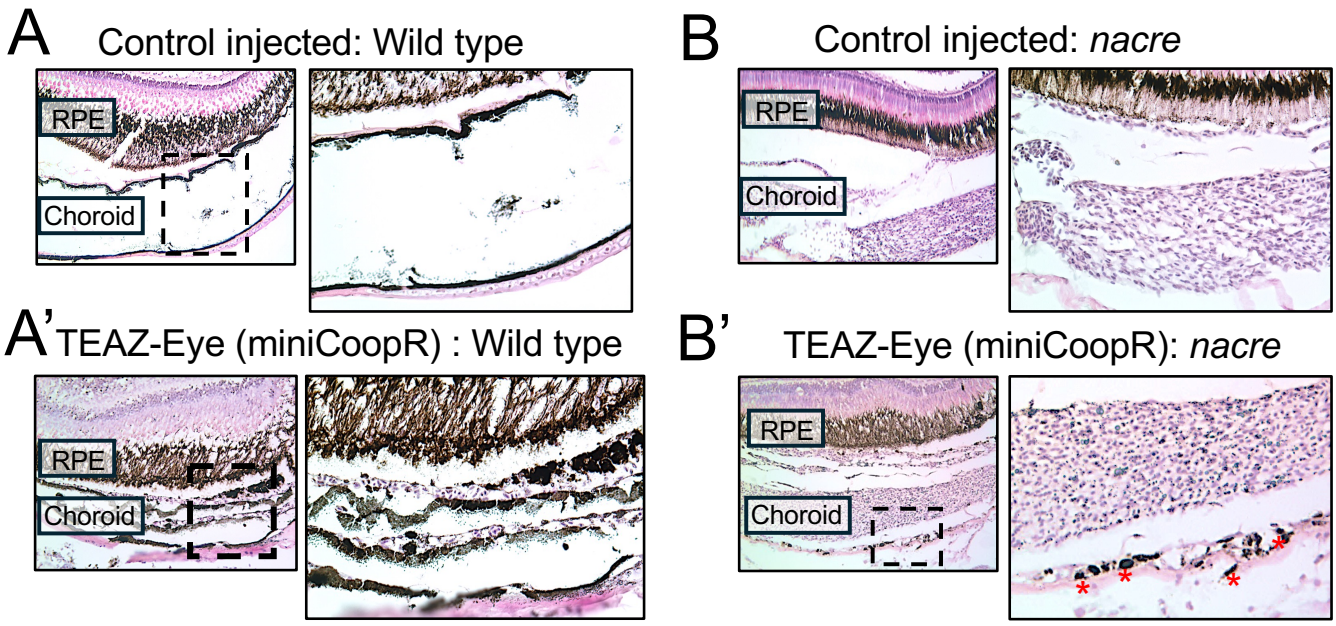
A
Control injected: Wild type
RPE
Choroid
B
Control injected: *nacre*
RPE
Choroid
A'
TEAZ-Eye (miniCoopR) : Wild type
RPE
Choroid
B'
TEAZ-Eye (miniCoopR): *nacre*
RPE
Choroid

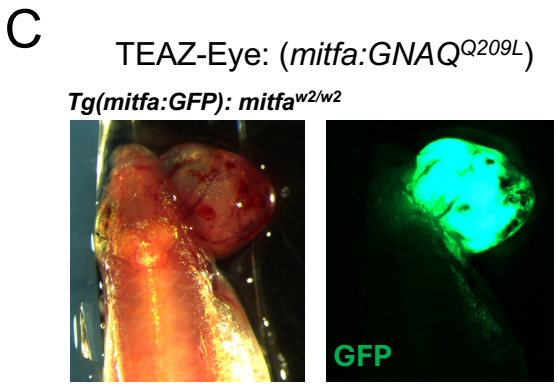
C
TEAZ-Eye: (*mitfa:GNAQ*^{Q209L})
Tg(mitfa:GFP): mitfa$^{w2/w2}$
GFP

Figure S11

Single-cell RNA seq Replicates

Tissue	Genotype	Replicate 1 (pooled tissue, tumors)
Eye	Casper	3 pooled eyes
Eye Tumor	Casper	3 pooled tumors 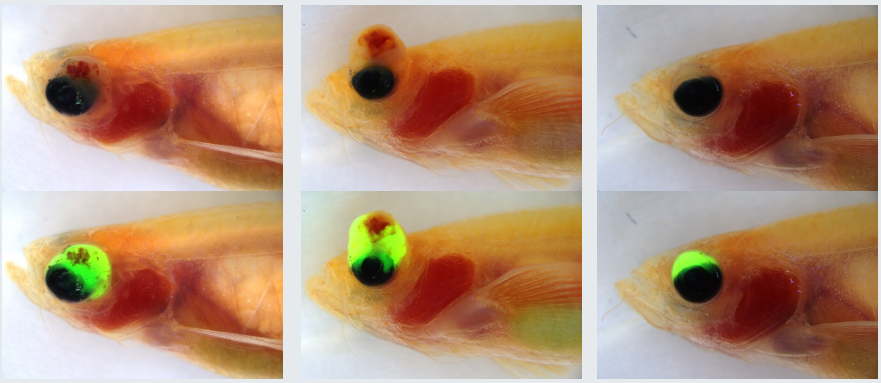
Whole embryo 28hpf	Wild-type Tg(mitfa:GFP); mitfa$^{+/w2}$	Pooled embryos 25 total 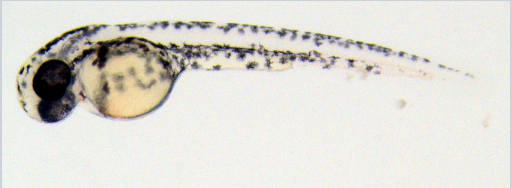
Whole embryo 28hpf	Nacre Tg(mitfa:GFP); mitfa$^{w2/w2}$	Pooled embryos 25 total 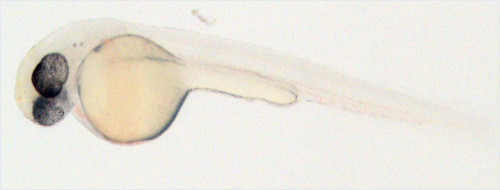

Figure S12

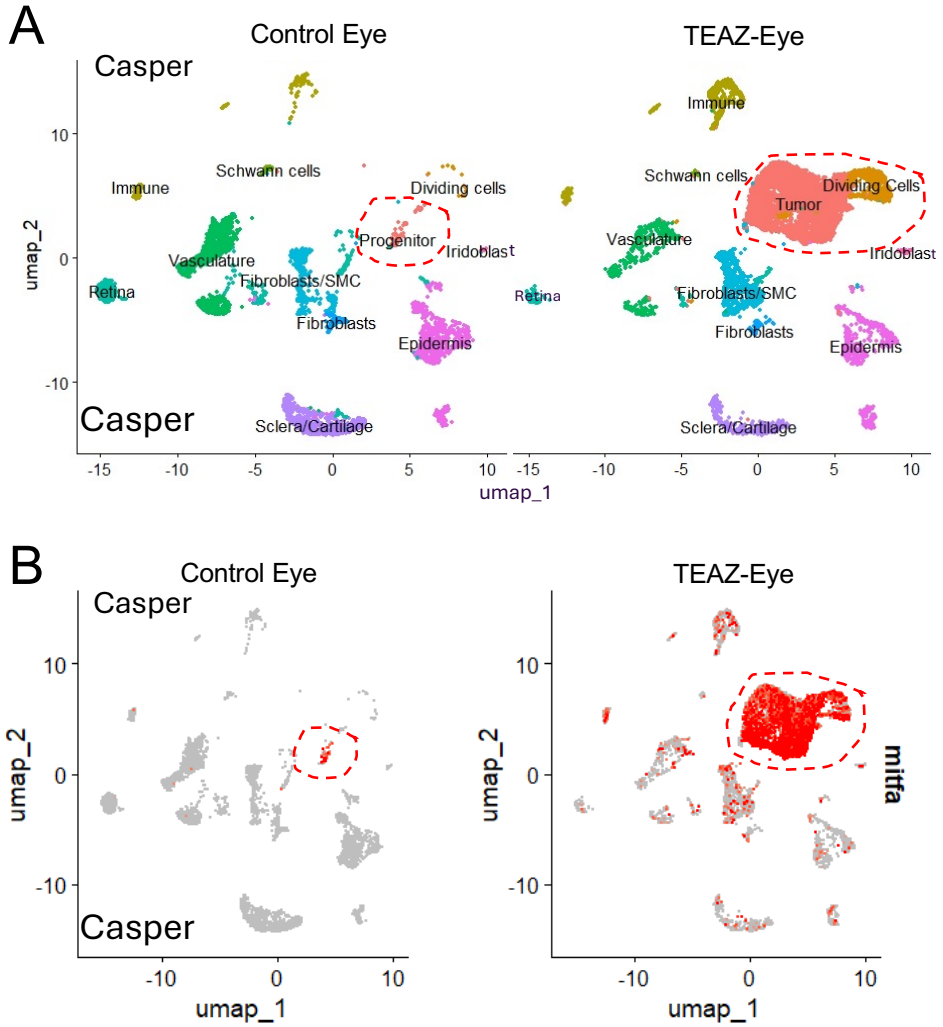
A
Control Eye
TEAZ-Eye
Casper
Casper
Immune
Schwann cells
Dividing cells
Progenitor
Iridoblast
Vasculature
Fibroblasts/SMC
Fibroblasts
Epidermis
Retina
Sclera/Cartilage
Immune
Schwann cells
Dividing Cells
Tumor
Vasculature
Iridoblast
Retina
Fibroblasts/SMC
Fibroblasts
Epidermis
Sclera/Cartilage
umap_2
umap_1
B
Control Eye
TEAZ-Eye
Casper
Casper
mitfa
umap_2
umap_1

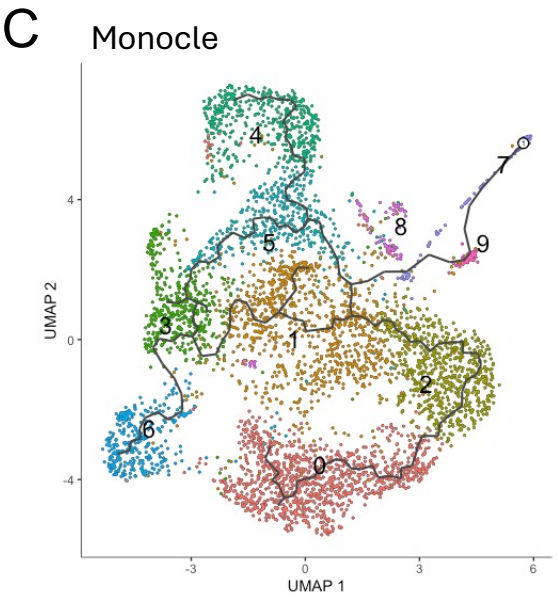
C
Monocle
UMAP 2
UMAP 1

Figure S13

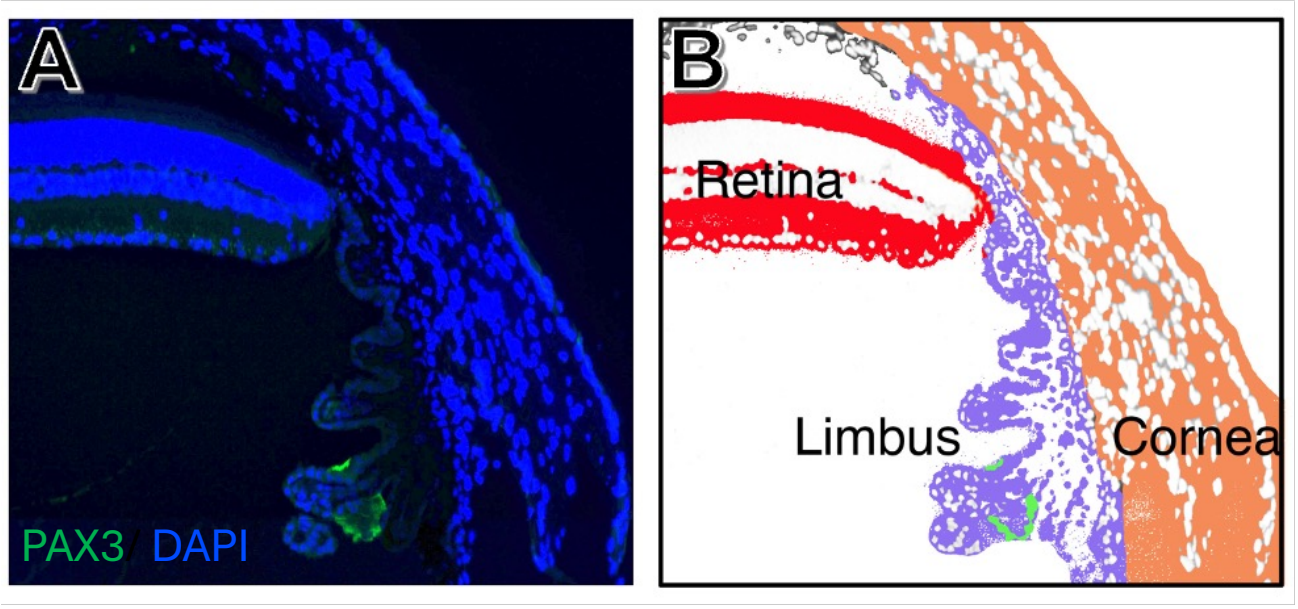

FIGURE S14

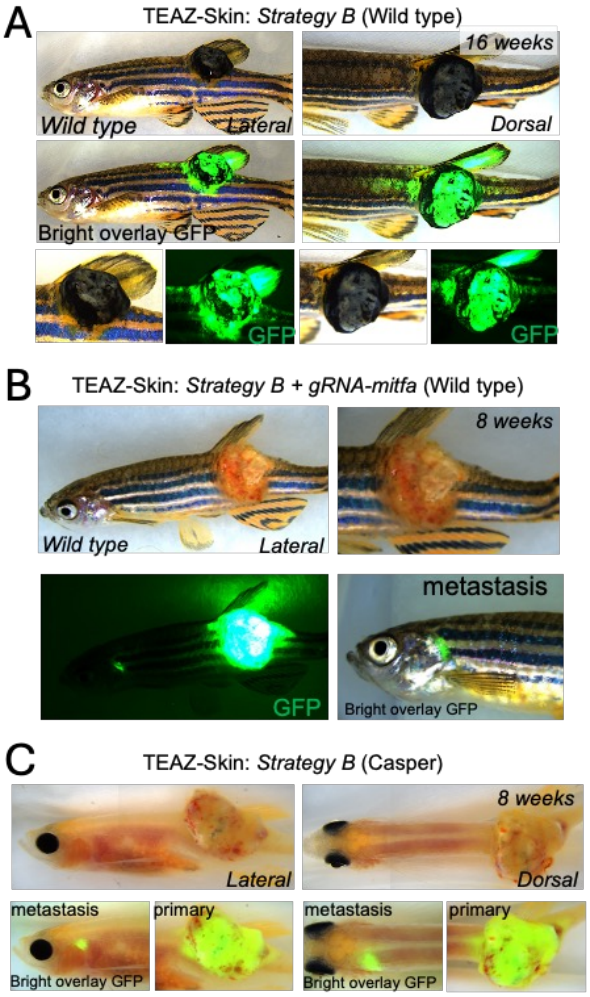
A
TEAZ-Skin: Strategy B (Wild type)
16 weeks
Wild type
Lateral
Dorsal
Bright overlay GFP
GFP
GFP
B
TEAZ-Skin: Strategy B + gRNA-mitfa (Wild type)
8 weeks
Wild type
Lateral
metastasis
GFP
Bright overlay GFP
C
TEAZ-Skin: Strategy B (Casper)
8 weeks
Lateral
Dorsal
metastasis
primary
metastasis
primary
Bright overlay GFP
Bright overlay GFP

Figure S15

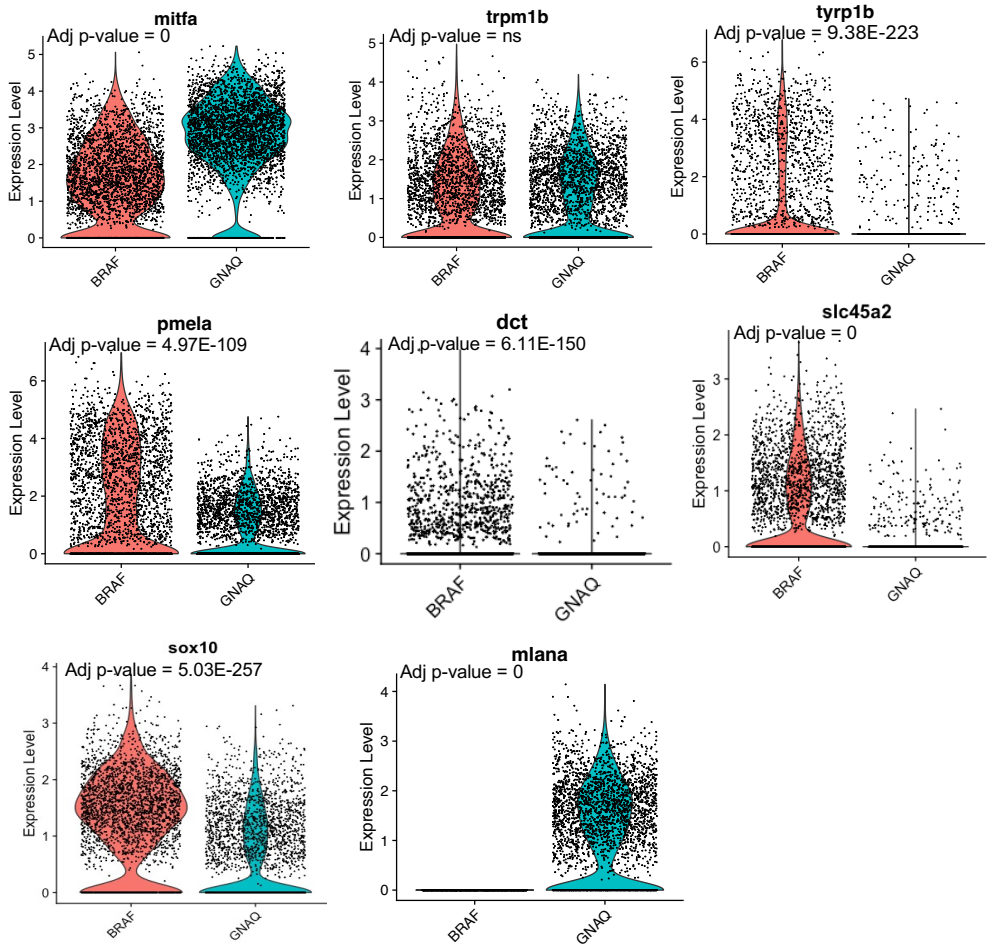
mitfa
Adj p-value = 0
trpm1b
Adj p-value = ns
tyrp1b
Adj p-value = 9.38E-223
pmela
Adj p-value = 4.97E-109
dct
Adj p-value = 6.11E-150
slc45a2
Adj p-value = 0
sox10
Adj p-value = 5.03E-257
mlana
Adj p-value = 0
Expression Level
BRAF
GNAQ

Figure S16

TEAZ-Eye Strategy B (Wild-type)

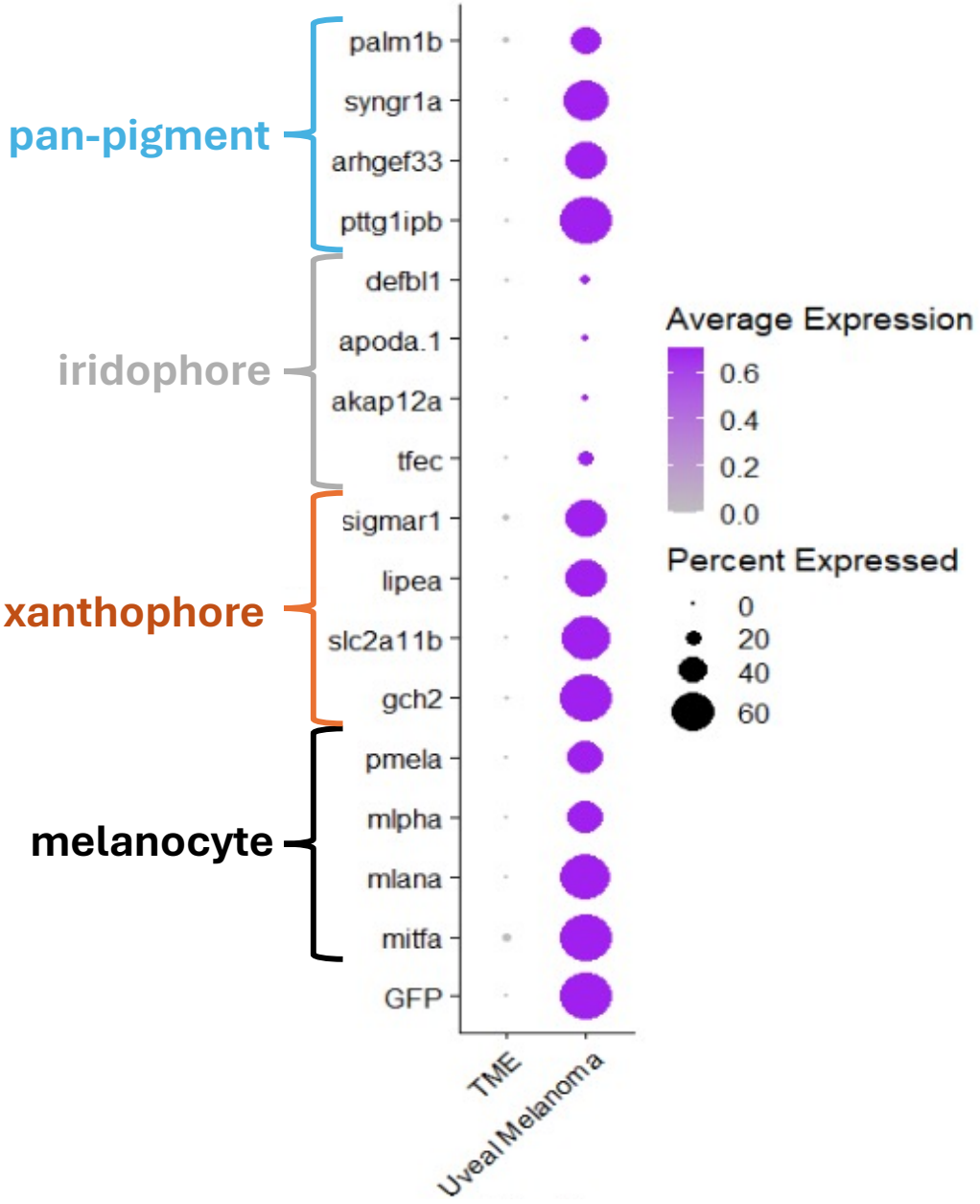

Figure S17

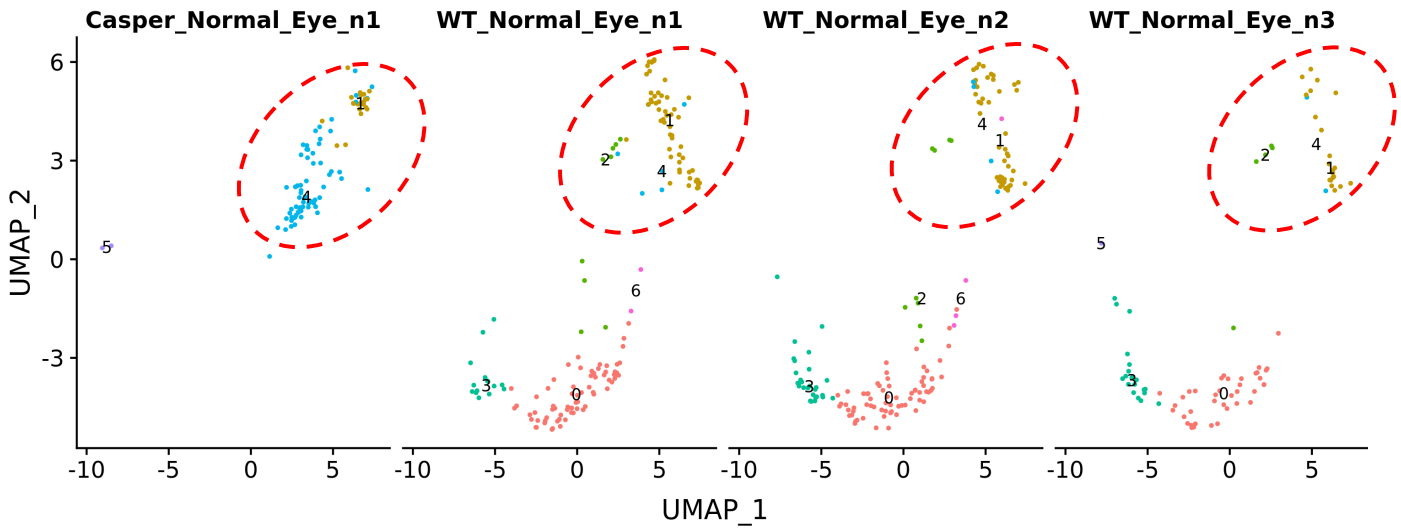
Casper_Normal_Eye_n1
WT_Normal_Eye_n1
WT_Normal_Eye_n2
WT_Normal_Eye_n3
UMAP_2
UMAP_1
6
3
0
-3
-10
-5
0
5

Figure S18